HYDRAULIC FRACTURE INTERACTING WITH PARTIALLY-CEMENTED AND NON-PERSISTENT NATURAL FRACTURE

by

Wei Fu

B. E. in Civil Engineering, Southwest Jiaotong University, 2011

M. S. in Bridge and Tunnel Engineering, Southwest Jiaotong University, 2013

Submitted to the Graduate Faculty of

the Swanson School of Engineering in partial fulfillment

of the requirements for the degree of

Doctor of Philosophy

University of Pittsburgh

2018

UNIVERSITY OF PITTSBURGH

SWANSON SCHOOL OF ENGINEERING

This dissertation was presented

by

Wei Fu

It was defended on

February 14, 2018

and approved by

Andrew P. Bunger, Ph.D., Assistant Professor, Department of Civil and Environmental

Engineering & Department of Chemical and Petroleum Engineering

Jeen-Shang Lin, Ph.D., Associate Professor, Department of Civil and Environmental

Engineering

Luis Vallejo, Ph.D., Professor, Department of Civil and Environmental Engineering

William Harbert, Ph.D., Professor, Department of Geology and Environmental Science

Dissertation Director: Andrew P. Bunger, Ph.D., Assistant Professor, Department of Civil

and Environmental Engineering & Department of Chemical and Petroleum Engineering

HYDRAULIC FRACTURE INTERACTING WITH PARTIALLY-CEMENTED AND NON-PERSISTENT NATURAL FRACTURE

Wei Fu, PhD

University of Pittsburgh, 2018

Natural fractures (NFs) are commonly encountered in unconventional reservoirs, sometimes strongly impacting the hydraulic fracture (HF) propagation. The HF-NF interaction has been studied extensively as a 2D problem, and almost all studies assume NFs to be continuous with the same properties over the entire NFs. However, it is a nearly ubiquitous feature that NFs in shale reservoirs are of different sizes and fully/partially filled with mineralization, leading to spatial variations in mechanical properties. These heterogeneous features of NFs may lead to distinctive interaction behaviors that can only be understood in a 3D setting.

Inspired by field observations, this research is aimed at studying the influence of NF heterogeneity on HF propagation. It is comprised of three main parts. First, analogue laboratory experiments were carried out to demonstrate the HF-NF interaction with variations of cemented proportion and cementation strength of NFs. Experimental observations prove that the spatial heterogeneity of NFs can significantly influence the HF propagation path. Three main patterns were observed as the size of the cemented region(s) decreases: (1) complete crossing (2) crossing with mismatched crack path (3) no crossing. Furthermore, based on and benchmarked with lab observations, a new 3D analytical criterion was developed from linear elastic fracture mechanics to quantitatively assess the dependence of HF-NF interaction behaviors on NF heterogeneity. Lastly, fully-coupled DEM (distinct element method) lattice simulation was conducted on the 3D growth of HFs crossing partially/fully cemented NFs. The simulation results are consistent with

experimental observations and match the analytical criterion well in an extended parametric space of NF properties including twenty sets of simulation cases.

In summary, experimental, analytical and numerical approaches demonstrate the essential consideration of NF heterogeneity when estimating the HF propagation. This work reveals the 3D interaction patterns of HFs crossing partially-cemented and non-persistent NFs, and identifies the role of spatially-varied NF properties in HF-NF interaction. Most importantly, a new analytical criterion is found to give good agreement with both experimental and fully-coupled numerical results. It therefore can be used to embed more realistic criteria in numerical simulators aimed at predicting potentially complex and multi-stranded HF propagation in unconventional reservoirs.

TABLE OF CONTENTS

LIST OF TABLES

LIST OF FIGURES

PREFACE

First and foremost, I would like to thank my advisor, Professor Andrew Bunger, who gives me complete trust and support during my path of achieving career goals. He has shaped my view of research with his creativity and enthusiasm. The dynamic research lab he has nurtured, excellent guidance he provided, and highly-enjoyable interactions we had on experimental, analytical and numerical problems were immensely helpful in advancing my research in geomechanics. I will also never forget the Australia Day Party, Thanksgiving Dinner and Hot-Pot Night that he and his family treated me to, and deeply value his mentoring and motivation both to my study and life.

I would like to thank Dr. Alexei Savitski and Dr. John Dudley, whom I have had the privilege of working with on my PhD project, and in the dynamic collaborative environment of Geomechanics Lab at Shell Technology Center Houston. They offered insightful suggestions and instructions on my research and publications and unreserved encouragement to my work. I always benefited from their high-standard scientific attitude as well as personal wisdom.

Moreover, I would like to thank my committee members Professor Jeen-Shang Lin, Professor Luis Vallejo, and Professor William Harbert for their professional guidance and time dedicated to this dissertation. Many thanks go to my friends overseas, and my fellow students Navid Zolfaghari, Pengju Xing, Guanyi Lu, Qiao Lu, Delal Gunaydin, Cheng Cheng, Di Wang, Yao Huang, Yunxing Lu, Bo Luo, Jesse Rippole, Wu Zhao, Tao Jiang, Shuaifang Zhang and Han Shi for the company and passionate scientific discussions.

I would also like to thank the outstanding lab crew of my project: Charles Hager (Scooter), Brandon Ames (The Breaker) and Garrett Swarm (Mr. Smoother) for their enormous assistance and collaboration on hydraulic fracturing experiments, soil/rock mechanics tests, and various material property characterization tests. We spent hundreds of hours together, thought outside the box in test design and improvement and overcame many obstacles to achieve reliable results.

I would like to express the deepest gratitude to my parents, sister, and family, for their endless love, support, and encouragement. My mother and father are my heroes. They teach me to be a man and make me who I am with their integrity, kindness, compassion, and reliability. A son of parents, a husband of wife, a father or grandfather of children, whatever roles I am or will be, their love will always make a part of me.

Finally, I would like to reserve my special gratitude to my beloved wonderful fiancée Weijin Wang and her parents. Weijin is kind and caring, delicate yet strong, and always by my side. Her talent in art and pure curiosity of beauty would lead me back to the rest of the world after I spent too long in my research zone. When we first met, we were still first-year undergraduate students in college, now we both graduated from the same university with PhD. Time flies, you stay.

At first I thought pursuing a PhD degree would be a walk in the park, but at the end it actually reminded me that this journey is largely a state of mind. Every past day and night were not only a part of the study, but also a part of my life. There were and will always be unpredictable challenges, I may never know what chocolate I am going to get, but now I know what attitude I shall take. For that, I will be eternally grateful.

1.0   INTRODUCTION

Hydraulic fracturing, together with horizontal drilling, is the main technology for enhancing the production of hydrocarbons trapped in low-permeability reservoirs. Extensive field observations show through core samples, image logs, mineback experiments, and outcrop studies that unconventional reservoirs tend to contain NFs (Warpinski and Teufel 1987; Hennings et al. 2000; Gale et al. 2007, 2014; Jeffrey et al. 2009a). These natural fractures (NFs) are in the forms of veins, joints, bedding planes and faults and may result in substantial difference in the hydraulic fracture (HF) propagation geometry compared to the symmetric and planar growth assumed in homogenous rock matrix. Indeed, both field and laboratory experiments demonstrate that HFs can cross, cross with offsetting, or be deviated by NFs, causing asymmetrical and multiple-strand propagation trajectories and eventually complex fracture networks (Hanson et al. 1981; Teufel and Clark 1984; Warpinski and Teufel 1987; Jeffrey et al. 2009a, b). A large number of published studies on HF-NF interaction have focused on identifying and evaluating the key factors that influence the interaction behaviors. It is shown that the HF tends to cross the NF under high differential stress and/or intersection angle. On the other hand, it can be blunted or deviated by the NF under low differential stress and/or intersection angle (Blanton 1982, 1986; Doe and Boyce 1989; Gu and Weng 2010; Gu et al. 2012). The influence of fluid flow factors, such as the injection

1

rate, fluid viscosity and NF conductivity, are also investigated through experiments and numerical/analytical modeling (Beugelsdijk et al. 2000; Zhang et al. 2009; Chuprakov et al. 2013; Kresse et al. 2013a; Llanos et al. 2017).

While past studies have provided important information on the HF-NF interaction mechanisms and demonstrate the necessity of further research, one ubiquitous feature of NFs has hitherto been ignored: NFs tend to be partially/fully filled with mineralization (Laubach 2003; Gale et al. 2007, 2014; Gale and Holder 2008). The cement strength can vary widely depending on the composition of the mineralization. For the Barnett Shale (Texas), the cementing material is often calcite that may serve as weak discontinuities during HF treatments (Gale and Holder 2008; Lee et al. 2014). In the highly siliceous Woodford Shale and tight-gas sandstone reservoirs, quartz-filled veins are commonly encountered, which are stiffer/stronger than the host rock (Gale et al. 2014; Lander and Laubach 2014; Laubach et al. 2016). Core samples and outcrops from eighteen shale plays also show that NFs have different heights ranging from <1 cm to 1.8 m (Gale et al. 2014). Hence, the existence of partially or fully cemented NFs with different size and cementation strength may have a first-order impact on the mechanics of HF-NF interaction, and will bring the problem to 3D due to the spatially-varied NF properties. In contrast, most studies assume that NFs have uniform properties that span the entire height of the HF/reservoir, which eventually lead to the 2D analysis. As a result, several fundamentally 3D questions that are of great importance to reservoir stimulation design remain poorly understood. For example: 1) Will partially cemented NFs affect HF propagation differently from uncemented/fully cemented NFs, and 2) Do small NFs matter in real hydraulic fracturing applications?

Besides there being little understanding of the 3D HF-NF interaction behaviors, the challenge is compounded in developing models to evaluate and predict the interaction. Analytical

solutions and mechanical models have been widely used to understand the mechanics and predict the propagation of HF in fractured reservoirs. Blanton (Blanton 1982, 1986) derived a criterion based on elastic solution which is a function of the differential in-situ stresses and angle of interaction. Warpinski and Teufel (Warpinski and Teufel 1987) proposed an analytical model to predict the NF dilation which considers the perturbation of the stress field near the dilated NF and the effect of the pore pressure change resulting from fluid leak off. Renshaw and Pollard (Renshaw and Pollard 1995) developed an analytical criterion from linear elastic fracture mechanics which evaluates HF crossing/no crossing behaviors based on in-situ stresses, host rock strength and frictional properties of NFs. This criterion is later extended to include the impact of NF cohesion and different intersection angles (Gu and Weng 2010; Gu et al. 2012). Chuprakov and co-authors (Chuprakov et al. 2013) developed an analytical model (OpenT) to include the effects of fluid flow parameters on NF's local activation and re-initiation. While these researches provide important tools for predicting HF-NF interactions, two simplifying assumptions have been continuously made: 1) the height of the HF is comparable or less than the height of the NF/reservoir height, and 2) the properties of the NF are uniform. In other words, the mechanical and geometrical heterogeneities of NFs are not taken into account, which might be impractical for the conditions in real reservoirs.

Another challenge lays in the numerical modeling of the 3D HF-NF interaction behaviors in fractured reservoirs. According to the HF geometry and HF-NF interaction mechanisms, current numerical models can be generally divided into three categories. The first category is 2D models, which normally employ plane strain assumption (Budyn et al. 2004; Zhang and Jeffrey 2006; Zhang et al. 2007; Dahi-Taleghani and Olson 2011; Dahi Taleghani et al. 2013). A second category of simulators consists of Pseudo-3D models and some fully 3D models that couple with simplified

2D HF-NF interaction criteria (Olson and Dahi Taleghani 2009; Weng et al. 2011, 2014; McClure et al. 2016). These models solve fluid flow and fracture deformation in 3D and therefore break the 2D limitations. However, they still cannot account for the true 3D HF-NF interactions because of implementing 2D analytical criteria and/or ignore the spatially-varied NF properties. Recently, more complex 3D models are being developed to solve fully-coupled interaction between HFs and NFs with non-uniform properties (Damjanac et al. 2010, 2016, Nagel et al. 2011, 2013; Damjanac and Cundall 2016; Settgast et al. 2017).

Indeed, the non-persistence and spatial variability of NFs have been one of the most challenging problems in practical rock engineering and are proved to have significant influence on the overall rock mass behaviors (Einstein et al. 1983; Kim et al. 2007; Bahaaddini et al. 2009; Shang et al. 2017). In the hydraulic fracturing area, the interaction between HFs and partially cemented/non-persistent NFs comprise a new topic with the potential to contribute important insights into the 3D interaction behaviors and the mechanics behind the complex and multi-strand HF propagation in low-permeability oil/gas or geothermal reservoirs. The research herein will focus on demonstrating qualitatively and quantitatively the impact of NF heterogeneities, characterized by the proportion of cemented region(s), cementation strength and NF height, on the HF propagation. Specifically, the work will be comprised of analog laboratory experiments to reveal the 3D interaction patterns of HF crossing partially cemented/non-persistent NFs, development of new analytical criterion to predict the 3D interaction behaviors, and fully-coupled numerical simulation of HF-NF interaction using a 3D DEM (distinct element method) lattice model.

2.0   IMPACT OF PARTIALLY-CEMENTED AND NON-PERSISTENT NATURAL FRACTURES ON HYDRAULIC FRACTURE PROPAGATION

2.1   PREAMBLE

The content of this chapter comprises a preprint of Fu et al. (2016). It presents laboratory experiments exploring the interaction between hydraulic fractures and cemented natural fractures. The seldom-considered configuration of partial cementing and non-persistence of natural fractures is observed to have first-order effect on the hydraulic fracture propagation path. As the ratio of the cemented to total height of an interface decreases, hydraulic fracture behaviors in the interaction with a fully/partially and strongly cemented interface transition as follows: (1) complete crossing, (2) crossing at cemented region(s) with mismatched crack path at uncemented region(s), (3) no crossing. The experimental observations also call into question the validity of the often-used assumptions in analytical/numerical models of: (1) natural fracture height coinciding with reservoir/hydraulic fracture height, and (2) uniform properties of the natural fracture.

2.2   ABSTRACT

This paper presents laboratory experiments exploring the interaction between hydraulic fractures and pre-existing natural fractures that are strongly cemented relative to the host-material strength

but over only a portion of the natural fracture. Two sets of experiments were conducted, including the central region cemented case and the top-bottom region cemented case. Three main patterns are observed for the interaction between hydraulic fractures and partially cemented natural fractures: (1) complete crossing (2) crossing with mismatched crack path (3) no crossing. The results show that a hydraulic fracture penetrates directly through a fully and strongly cemented pre-existing natural fracture. When the proportion of the strongly-cemented region decreases or the height of the weak natural fracture increases, the hydraulic fracture is observed to persist through the entire height of the specimen both before and after the interface. However, the fracture path proceeds directly through strongly-cemented portions while causing mismatched crack path at uncemented portions. No crossing results are obtained when the strongly-cemented region is sufficiently small, around 30% of the natural fracture's height. Results of this seldom-considered but almost certainly realistic configuration of partial cementing suggest that the hydraulic fracture path is strongly influenced by the size of the cemented region of the natural fracture.

2.3   INTRODUCTION

Hydraulic fracturing is a widely used well-stimulation technique for enhancing the productivity of oil and natural gas in low-permeability unconventional reservoirs. Over the years, hydraulic fracturing treatment designs in the industry have been using symmetric and planar growth models, which assume the reservoirs to be homogenous. However, extensive field observations show that many reservoirs contain preexisting natural fractures in the forms of faults, veins, joints and bedding planes. These natural fractures may result in substantial difference in the hydraulic fracture propagation geometry. Indeed, both field and laboratory experiments show that hydraulic

6

fractures can be greatly influenced by natural fractures, causing asymmetrical and multiple-strand propagation and eventually complex fracture networks (Hanson et al. 1981; Teufel and Clark 1984; Warpinski and Teufel 1987; Jeffrey et al. 2009a, b). The mechanics of the interaction of hydraulic fractures with natural fractures is often understood through some now-classical analytical solutions and mechanical models (Blanton 1982, 1986; Warpinski and Teufel 1987; Renshaw and Pollard 1995). Work on this subject is ongoing, with recent contributions aimed at experimental evaluation of these criteria and/or development of more generalized approaches (Gu and Weng 2010; Gu et al. 2012). Extensive numerical studies have also been conducted to interpret and predict the mode of interaction (Zhang and Jeffrey 2006; Zhang et al. 2007; Weng et al. 2011; Dahi-Taleghani and Olson 2011; Chuprakov et al. 2013; Kresse et al. 2013b; Wu and Olson 2015).

In spite of these advances, almost all the studies on this problem assume the natural fracture to be continuous and most experimental analyses of hydraulic fracture-natural fracture interaction treat natural fractures as frictional interfaces with no cohesion (Blanton 1982; Renshaw and Pollard 1995) or very weak cohesion (Gu et al. 2012). However, it is almost a ubiquitous feature that natural fractures in real reservoirs tend to be partially or fully cemented with minerals. For shale reservoirs this cement is often calcite; while in tight gas sandstone reservoirs it is common to encounter quartz-filled veins (Gale et al. 2007, 2014; Lander and Laubach 2014). From a mechanical perspective, the existence of partially or fully cemented natural fractures in reservoirs ought to be an important distinction that should lead to differences in hydraulic fracture growth and hence must be considered for stimulation approaches to be successful.

To address the distinction, we carried out analog laboratory experiments symmetrically on specimens with partially/fully-cemented interfaces. In this paper, fully-cemented interface experiments are presented as the base case; two sets of partially-cemented interface experiments,

7

including the central region cemented case and the top-bottom region cemented case, are presented for comparison and illustrating the impact of partially-cemented natural fractures on hydraulic fracture propagation behaviors.

2.4   EXPERIMENTAL PROCEDURE

The experimental setup is depicted in Figure 2.1. Specimens are loaded symmetrically with hydraulic actuators in a true tri-axial loading frame. Transparent polymethyl methacrylate (PMMA) spacers are placed around the specimen to promote an evenly distributed compressive stress field. Note that hydraulic fractures cannot cross a discontinuity to grow into PMMA because of the lack of flaws that could nucleate growth. The fluid used for initiating the hydraulic fracture is a solution of glycerine and water with food dye added to track the hydraulic fracture geometry inside the specimen. The viscosity of the solution is 0.3 Pa · s at 20 ℃. Pressurized hydraulic fluid is delivered by a syringe pump with the capability to provide both flow rate control and pressure control.
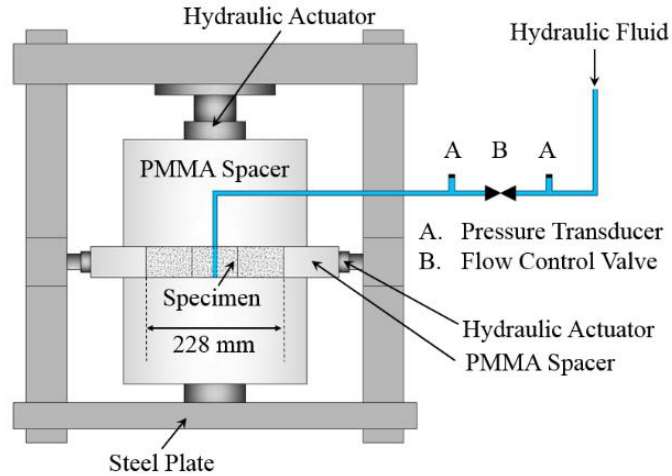
Figure 2.1: Sketch of the cross-sectional view of the experimental setup.

Specimens were prepared from Portland cement mortar mix with a 28-day cure period at 100% humidity. The tensile strength of the specimens is around 2 MPa (from direct tension test, pull-off method). As depicted in Figure 2.2a, specimens consist of three mortar blocks. The dimensions of each block are 76mm · 76mm · 51mm (3 inches · 3 inches · 2 inches). The interfaces of the blocks are partially or fully glued together by an epoxy adhesive which generates a bonding strength several times greater than the tensile strength of the mortar specimens. It has been shown in many core samples and outcrops that natural fractures in shale reservoirs are mostly narrow fractures (Gale et al. 2007, 2014). Therefore, the specimens are prepared such that the thickness of the cementation layers is of sub-millimeter scale. The wellbore for these experiments is a 100mm long stainless steel tube with an outer diameter of 9.5mm and with perforations over its central region. This tube is placed in the central block and sealed in place with a strong epoxy, using O-rings to define an approximately 25-30 mm long open-hole section in the central part of the 51 mm high specimens. During the test, an axially-oriented hydraulic fracture is initiated from the center of the wellbore, in an isolated region between two rubber O-rings (Figure 2.2b).

9
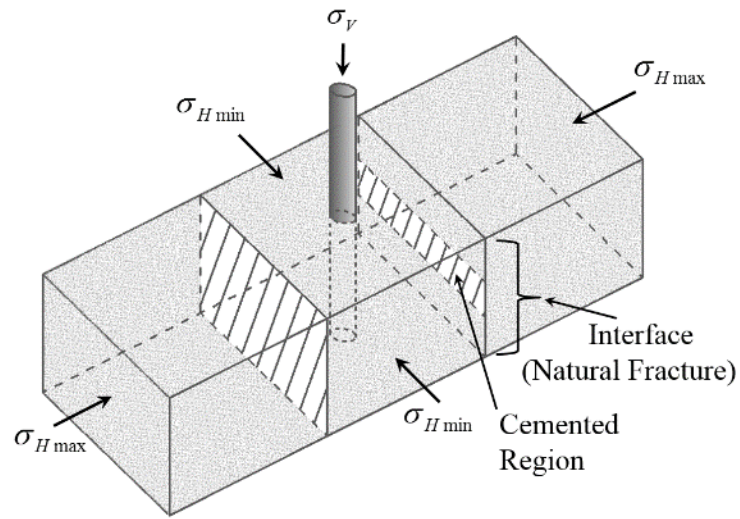
(a)
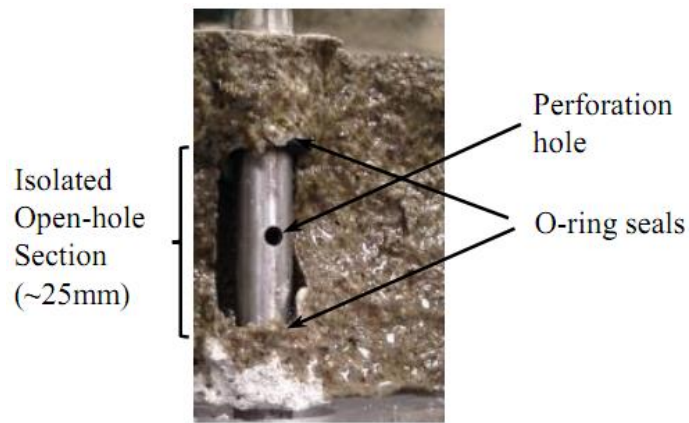
(b)

Figure 2.2: (a) Specimen geometry; (b) cross section of the isolated interval that is pressurized to generate axial hydraulic fractures.

In real reservoirs, the lag region between the fluid and fracture front or simply the "fluid lag" is expected to be extremely small in comparison with the length of the hydraulic fracture (Economides and Nolte 2000). Therefore, to promote the physical similarity between the experiments and the field, it is important to minimize fluid lag in laboratory experiments. In our case, fluid lag is minimized by adjusting the viscosity of the fluid and reducing the injection rate/fluid tip (Garagash and Detournay 2000). A comparison between the length of surface cracks and the wetted region inside the specimen showed that we were able to suppress fluid lag at the scale of observation in these experiments. However, such a statement must also be cautious because the fluid could have lagged behind the fracture front and this would not have been detected as long as it caught up sometime later in the test.

For these experiments, σ_{Hmin} (minimum horizontal stress) is set to zero and a vertical stress σ_V is applied to the specimen such that the hydraulic fracture is contained between two PMMA plates, propagates in the vertical plane and finally hits the interfaces, which are the analog of natural fractures. The intermediate σ_{Hmax} (maximum horizontal stress) is applied to the specimens to control the hydraulic fracture propagation orientation. See Table 2.1 for the values used for these quantities.

In the beginning of the experiment, a constant wellbore fluid pressure of 2.5 MPa is applied briefly to detect possible leaks in the injecting system. Then the fracture fluid is injected at a constant pump rate of 6ml/min into the steel tube, and this constant rate is maintained throughout the hydraulic fracture growth. Pump rate, wellbore pressure, fluid pressure, fluid displacement and confining stresses are recorded during the whole procedure (Figure 2.3).
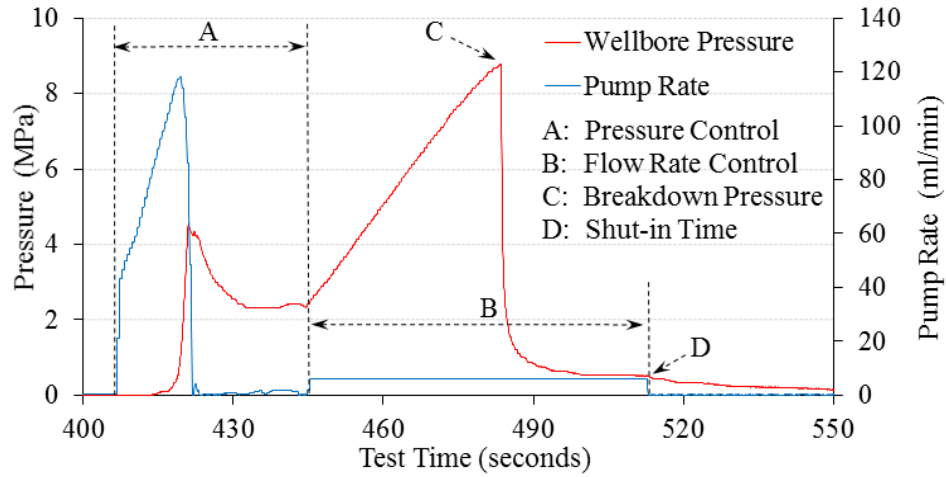
Figure 2.3: Pump rate and wellbore pressure record. Note that the constant pressure is set at the pump, resulting in a transient pressure downstream of the flow control valve (Figure 2.1).
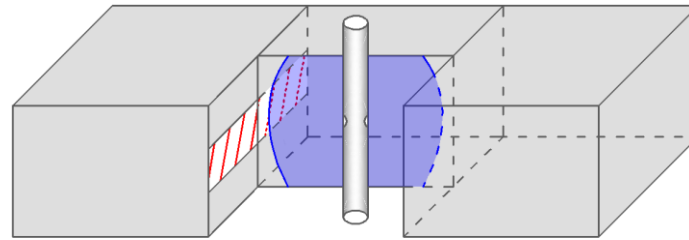
(a)
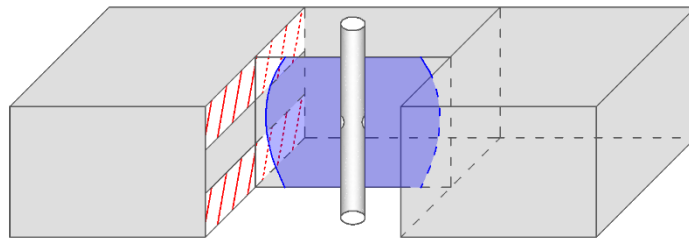
(b)

Figure 2.4: (a) Sketch of the central region cemented case; (b) sketch of the top-bottom region cemented case.

2.5 EXPERIMENTAL RESULTS

Two sets of partially-cemented interface experiments (central region cemented case and top-bottom region cemented case) were conducted, which are the analog of field conditions when hydraulic fractures encounter large natural fractures (e.g. long veins) that persist over the height of the reservoir and are partially filled with mineral cementation. Figure 2.4 shows the sketches of the two cases, with half of the central block removed for clarity. After the experiments were completed, specimens were separated manually to reveal the inside hydraulic fracture geometry and crack paths across interfaces.

Note that the direct, undeviated crossing of fully cemented interfaces, described below, shows that the cemented regions have no impact on hydraulic fracture propagation. In other words, the strongly and narrowly cemented regions are behaving analogously to intact rock. Therefore, the partially-cemented interfaces are also analogous to uncemented fractures with limited height, e.g. uncemented natural fractures that do not persist over the height of the reservoir.

2.5.1   Central Region Cemented Case

The impact of a partially-cemented (central region) natural fracture on hydraulic fracture propagation behavior was studied through a series of experiments in which the height of the cemented area was varied. Table 2.1 summarizes the experimental conditions and test results. Figure 2.5 shows the hydraulic fracture geometry and fracture paths at the interfaces for tests A1, A4 and A5 after manual separation. The hydraulic fracture can be seen running subvertically

through these blocks. In all the experiments, the hydraulic fracture was initiated from the isolated open-hole section and attained full height of the specimen before reaching the interfaces.

As shown in Figure 2.5a, A1 has a fully-cemented interface which generated no impact on the hydraulic fracture path. Figure 2.5b (A4) shows a central region cemented case with a cemented-region height of 21mm. The hydraulic fracture propagated in the vertical plane, crossed the cemented region directly and formed large fracture path "offset" at the uncemented regions. The wetted areas indicate the extent of fluid penetration. The hydraulic fracture was still able to grow to full height after crossing, but propagated to a relatively shorter distance compared to the fully cemented case (A1).

In experiment A5 (Figure 2.5c), the height of the cemented region was decreased to 15mm. The partially-cemented interface was largely debonded by the hydraulic fracture with no fracture penetration across the interface.
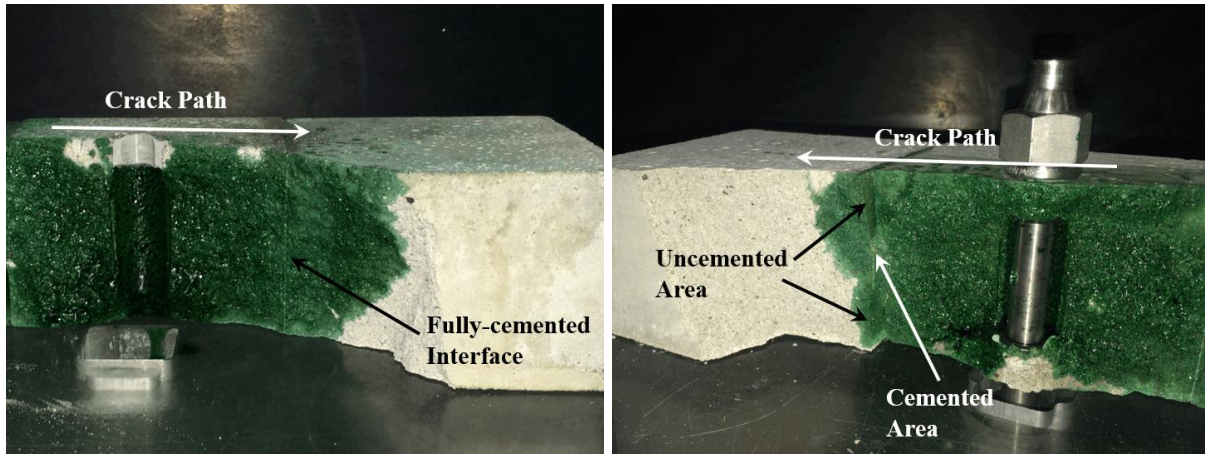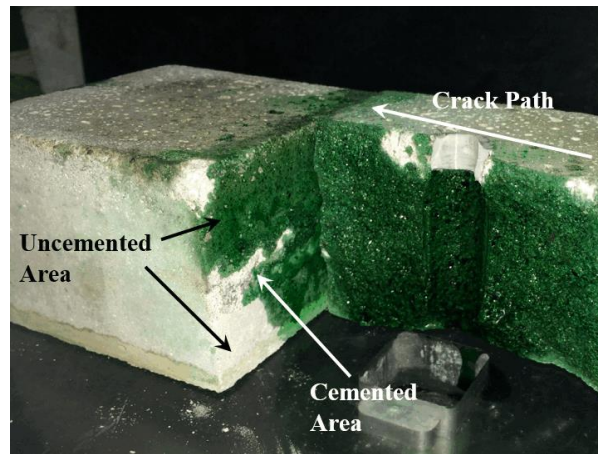
Figure 2.5: Photographs of specimens after testing and manual separation of the parts of the blocks, including cases with: (a) fully-cemented interface (A1, 100% cemented); (b) central region cemented interface (A4, 41% cemented); (c) central region cemented interface (A5, 29% cemented). Wetted areas indicate the extent of the hydraulic fluid penetration.

Table 2.1: Summary of experimental conditions and results for the central region cemented case.

Test	Height of Cemented Area (mm)	Cemented Height/ Total Height	σ_V (MPa)	σ_{Vmax} (MPa)	Results
A1	51	100%	1.3	1.1	Crossing
A2	39	76%	1.3	1.1	Crossing with "offset"
A3	22	43%	1.3	1.1	Crossing with "offset"
A4	21	41%	1.3	1.1	Crossing with "offset"
A5	15	29%	1.3	1.1	No crossing
A6	14	27%	1.3	1.1	No crossing
A7	10	20%	1.3	1.1	No crossing

Table 2.2: Summary of experimental conditions and results for top-bottom region cemented case.

Test	Height of Cemented Area (mm)	Cemented Height/ Total Height	σ_V (MPa)	σ_{Hmax} (MPa)	Results
B1	51	100%	1.2	1.0	Crossing
B2	26	51%	1.2	1.0	Crossing with "offset"
B3	17	33%	1.2	1.0	No crossing
B4	16	31%	1.2	1.0	No crossing

2.5.2 Top-bottom Region Cemented Case

Another set of experiments was conducted to study the influence of top-bottom region cemented natural fractures on hydraulic fracture propagation. Figure 2.6 presents photographs of specimens after testing and manual separation, which reveal the inside hydraulic fracture distribution and fracture paths at the interfaces. Table 2.2 summarizes the experimental conditions and test results.

Similar to A1, B1 is presented as the base case in which the fully and strongly cemented interface has no impact on hydraulic fracture propagation. The interfaces in B2, B3 and B4 were cemented at the top and bottom and uncemented in the center. In experiment B2 in which the cemented regions constitute 51% of the full interface height, the vertical hydraulic fracture crossed the interface directly at the cemented regions and generated an apparent offset fracture path at the uncemented region. After crossing the interface, the fluid front propagated further into the cemented regions than the uncemented region, which, in agreement with A4, indicates that the crossing of the interface initiated at the cemented regions. After crossing, the hydraulic fracture propagated horizontally at the cemented regions to reach a further distance and radially into the uncemented region to attain the full specimen height. In experiment B3 (Figure 2.6c), the cemented regions were mostly debonded with no hydraulic fracture penetration across the interface.
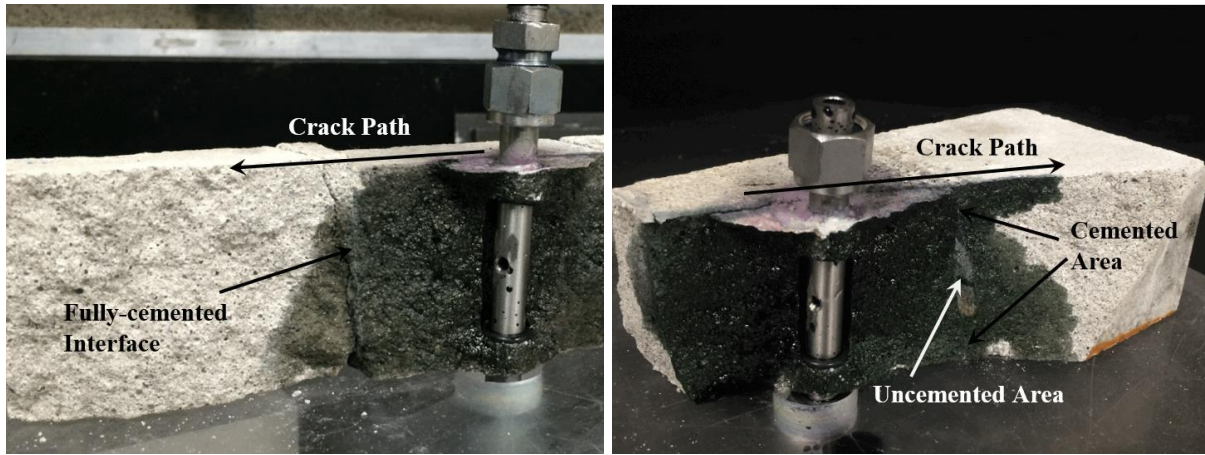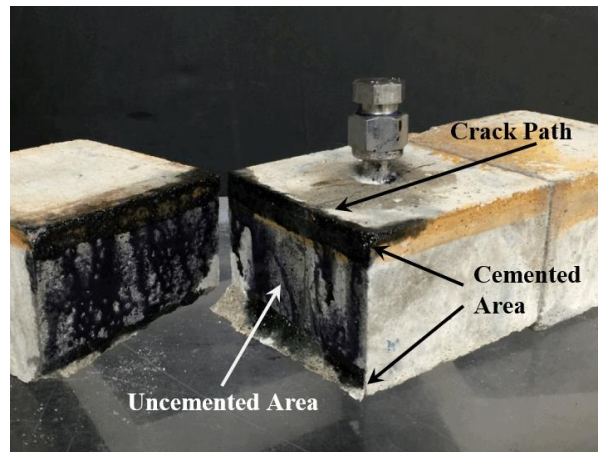
Figure 2.6: Photographs of specimens after testing and manual separation of the parts of the blocks, including cases with: (a) fully-cemented interface (B1, 100% cemented); (b) top-bottom region cemented interface (B2, 51% cemented); (c) top-bottom region cemented interface (B3, 33% cemented). Wetted areas indicate the extent of the hydraulic fluid penetration.

2.6   DISCUSSION

By observing the hydraulic fracture paths of the experiments, we are able to identify a transition in the behavior of hydraulic fracture-natural fracture interaction (Figure 2.7 and Figure 2.8). Figure 2.7 shows the traces of the hydraulic fracture on the adjacent faces of the blocks forming the interface. The "crack before crossing" is the trace along the surface of the middle block – the one in which the wellbore is contained. The "crack after crossing" trace is on the outer block, which is either partially or fully cemented to the middle block. When the two traces match, it means there is no "offset" in the hydraulic fracture path. Where they do not match, their separation indicates an "offset" along the interface.

However, there the word "offset" is placed in quotation because it is apparently formed by a fundamentally 3D phenomenon, described in more detail below and differing completely from the concept of offsetting adopted in a 2D view of the problem (after e.g. Warpinski and Teufel 1987 as well as the more recent experimental results of Bunger et al. 2016). Such phenomena in hydraulic fracture interaction with natural fractures has also been observed by Olson et al. 2012.
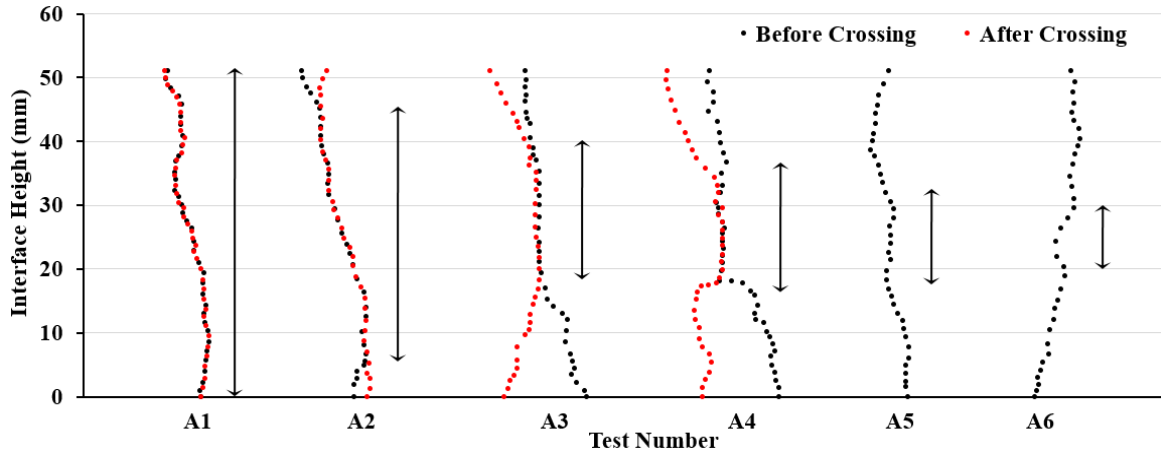
(a)
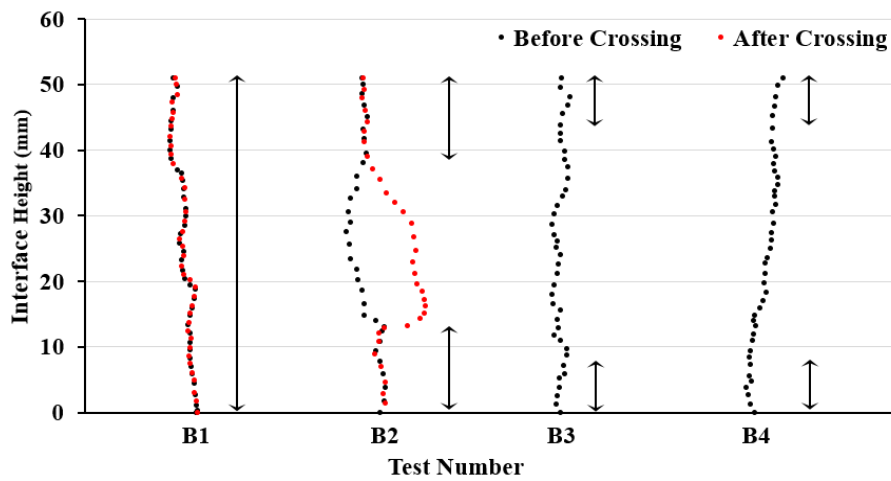
(b)

Figure 2.7: Digitized trace of offset between hydraulic fracture intersections at partially cemented interface, the ratio of the cemented to total height of an interface decreases to the right. Vertical black lines indicate the height and location of cemented regions: (a) Central region cemented case; (b) top-bottom region cemented case. The hydraulic fracture half-length at the time of intersection with the interface was the same (~38 mm) in all cases.
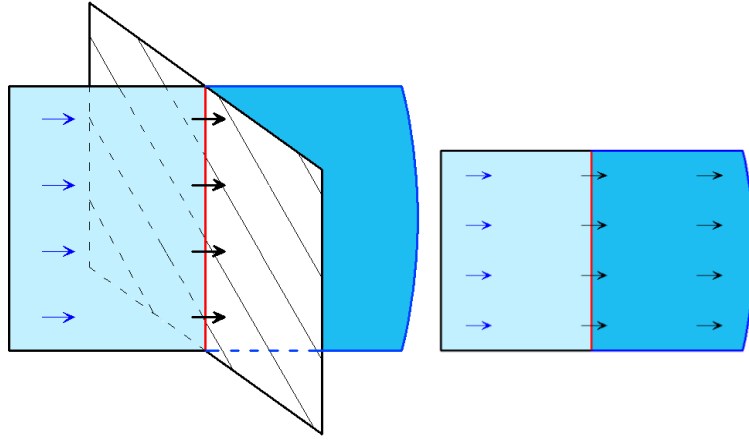
(a)
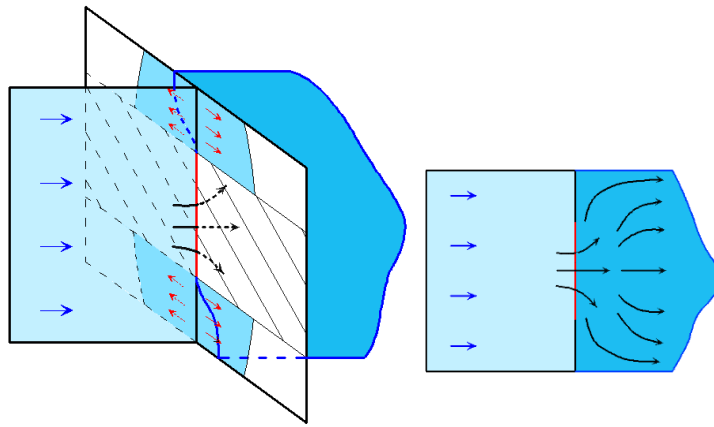
(b1)
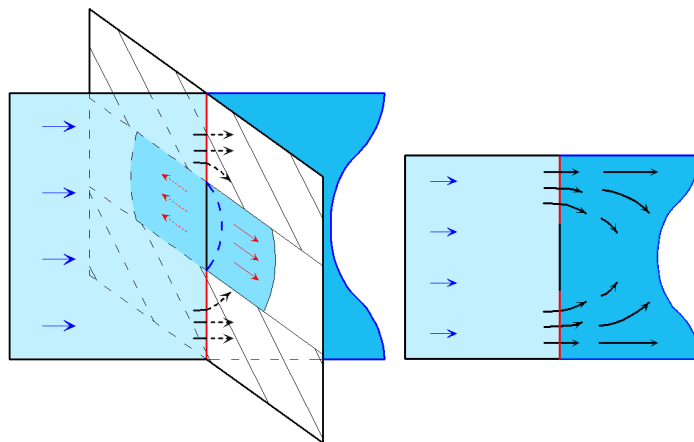
(b2)
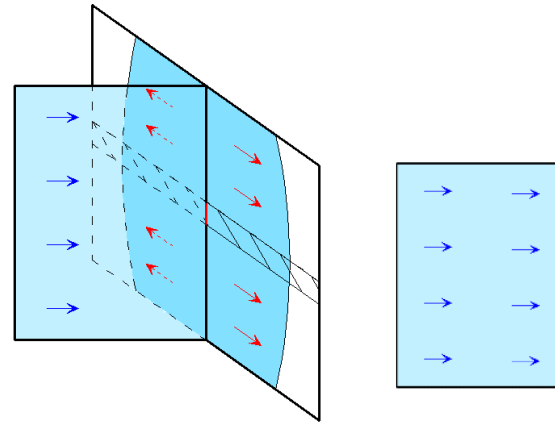
(c1)
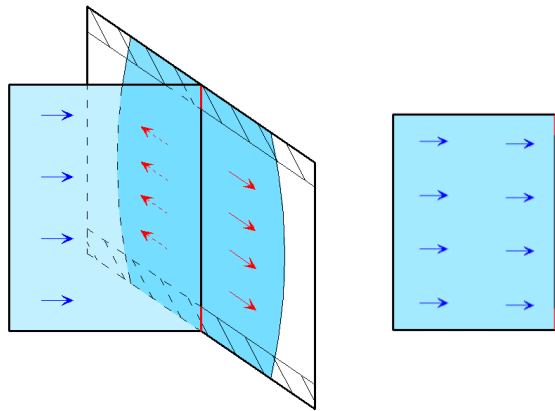
(c2)

Figure 2.8: 3D views and front views of a vertical hydraulic fracture intersecting orthogonally a fully/partially-cemented natural fracture: (a) Corresponds to tests A1 and B1; (b1) corresponds to tests A2, A3 and A4; (b2) corresponds to test B2; (c1) corresponds to tests A5, A6 and A7; (c2) corresponds to tests B3 and B4.

Figure 2.8 illustrates the behaviors of a vertical hydraulic fracture intersecting orthogonally a fully/partially-cemented natural fracture. The diagrams each show a single fracture wing with the wellbore at the left edge. In the 3D diagrams on the left, the hatched areas represent the cemented regions in the experimental block. The segment intersection of the growing hydraulic fracture and the cemented regions is highlighted in red. The blue, red and black arrows show the directions of fluid coming out from the wellbore, deflecting into the interface and crossing the interface, respectively. Light, dark and darker blue regions show the fluid distribution before crossing the interface, along the interface and after crossing the interface, respectively.

By inspecting Figure 2.7 and Figure 2.8, we observe that, for both central region cemented and top-bottom region cemented cases, as the ratio of the cemented to total height of an interface decreases, hydraulic fracture behaviors in the interaction with a fully/partially and strongly cemented interface transition as follows:

a.   Complete crossing (tests A1, B1, 100% cemented); see Figure 2.5a, Figure 2.6a.

b.   Crossing at cemented region(s) with "offset" at uncemented region(s) (tests A2, A3, A4, B2); see Figure 2.5b, Figure 2.6b.

c.   No crossing (tests A5, A6, A7, B3, B4), see Figure 2.5c, Figure 2.6c.

These experiments, therefore, lead to two main observations. The first is that, the size of cemented region(s) of the interface can strongly influence the hydraulic fracture propagation patterns. Under considered conditions, a hydraulic fracture can cross the interface directly or be completely deviated into the interface. Also, the hydraulic fracture is able to cross the interface and grow to full layer (i.e. reservoir) height on the other side of the interface even if only around 50% the interface is cemented. Hence, ignoring the fact that the natural fractures can be partially

23

cemented and/or of a height that is less than the reservoir height may lead to misleading predictions of the hydraulic fracture propagation in fractured reservoirs.

The second main observation is the "offset" of the hydraulic fracture path formed at the uncemented regions when the hydraulic fracture crosses partially cemented interfaces. But it is important to realize that even the terminology "crack path offset" is potentially misleading because it could lead to an erroneous impression of two-dimensional crack propagation that offsets when crossing an interface (e.g. the offsetting case of Zhang et al. 2007). In fact, the hydraulic fracture appears to cross directly, with no offset, at the cemented portion of the interface after which it grows to full height, resulting in a mismatch in the crack path and an offset to subsequent flow through the hydraulic fracture. We henceforth employ the terminology mismatched crack path because it is more purely observational rather than embedding a potentially incorrect interpretation based on a 2D view of the problem (Figure 2.9).
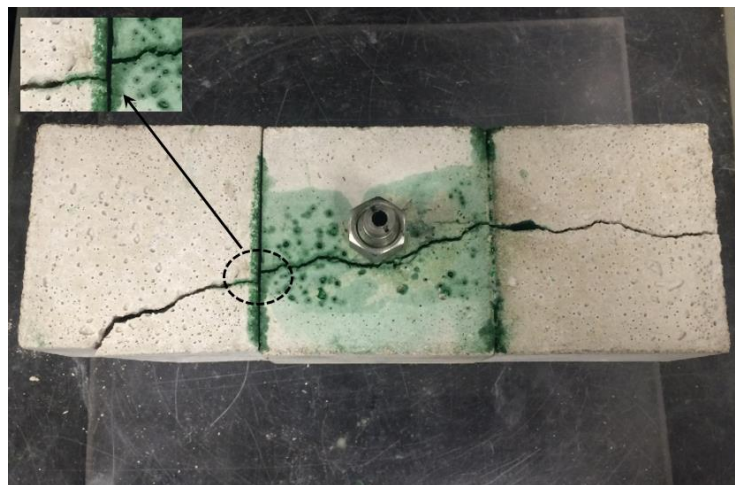
Figure 2.9: Photo of the hydraulic fracture path "offset": a 2D view, test A4.

2.7   CONCLUSIONS

These experiments reveal the influence of partially and strongly-cemented natural fractures on the hydraulic fracture propagation. The results indicate that, for a partially cemented natural fracture with relatively large cemented region, or an uncemented natural fracture persisting through only a small proportion of the height of the reservoir, the hydraulic fracture tends to cross directly at the cemented/intact region, then radiates and attains the full layer height after this crossing. This also results in mismatched fracture path at the uncemented regions, which must be interpreted with caution since the geometry was formed through fundamentally 3D growth process and cannot be captured in a 2D interpretation.

When the area of the cemented region decreases, the interaction between hydraulic fractures and natural fractures has three main patterns:

- Complete crossing

- Crossing with mismatched crack path

- No crossing

These three major interaction behaviors obtained from both sets of the experiments prove that the spatial heterogeneity of the natural fracture (size of the cemented region(s), total height of the natural fracture) can significantly influence the hydraulic fracture path and cause asymmetrical and multiple-strand propagation.

Here we reiterate that for the "crossing with mismatched crack path" case, it is critical to realize that the mechanism is fundamentally different from the 2D view that has been previously used to describe observed offsets (Warpinski and Teufel 1987; Zhang and Jeffrey 2006; Zhang et al. 2007). Indeed the 2D view may be sufficient in some growth geometries – for example, the offsetting observed by Bunger et al. (2016) can probably be well-explained in a 2D paradigm and simulated by 2D models. However, in the present experiments, the "crossing with mismatched crack path" geometry is fundamentally 3D, consisting of a portion over which there is no crossing, a portion of direct crossing with no offset, and an apparent offset that results from the fracture again attaining full height after crossing the interface.

Perhaps the most striking observation from the perspective of hydraulic fracture applications is that a relatively small cemented region(s) can be sufficient to promote crossing. Besides showing the inadequacy of 2D treatments of the problem, this observation calls into question the validity of the often-used assumptions of: 1) natural fracture height coinciding with reservoir height, and 2) uniform properties of the natural fracture. Such models carry the potential to underestimate the ability of hydraulic fractures to cross natural fractures, thereby overpredicting network-like complexity. Ongoing efforts are therefore directed towards making better predictions in light of the inherent and seemingly inescapable uncertainty in the distribution of strength properties for natural fractures.

3.0 ANALYTICAL CRITERION PREDICTING THE IMPACT OF NATURAL FRACTURE STRENGTH, HEIGHT AND CEMENTED PORTION ON HYDRAULIC FRACTURE GROWTH

3.1 PREAMBLE

This chapter comprises a preprint of (Fu et al. 2018a). In this chapter, a new analytical crossing criterion and its laboratory verification are presented for predicting the outcome when a hydraulic fracture impinges orthogonally on a natural fracture. Different from existing 2D criteria, this criterion considers the spatial variations of the natural fracture properties, including the proportion of cemented region(s), cementation strength and height of the natural fracture. It is compared with experimental results from four sets of hydraulic fracturing tests and observed to provide good predictions for the 3D hydraulic fracture-natural fracture interaction behaviors.

3.2 ABSTRACT

Natural fractures (NFs) are commonly encountered in unconventional reservoirs, sometimes strongly impacting hydraulic fracture (HF) propagation. The HF-NF interaction has been studied extensively as a 2D problem. However, outcrop and core observations indicate that many NFs are fully or partially cemented. The NF height also is variable relative to the full height of the reservoir

27

layers(s). These features of NFs - including the proportion of the cemented region(s), cementation strength, and NF height - may lead to distinctive interaction behaviors that can only be understood in a 3D setting. This paper presents a new analytical crossing criterion, and its laboratory verification, for predicting the outcome when a HF impinges orthogonally on a NF. Consistent with laboratory results, this criterion captures the dependence of crossing/no crossing behaviors on the proportion of cemented region(s), cementation strength, and the NF height relative to the total reservoir/HF height. Crossing of the NF is shown to be promoted by stronger cementation, larger cemented region, and/or shorter NF height. While these observations are not surprising, quantifying the dependencies using an analytical model that can be deployed within the framework of HF simulators is an unresolved challenge. Here an analytical criterion has been developed based on linear elastic fracture mechanics to quantitatively assess the influence of NF heterogeneity on the HF's crossing/no crossing behaviors. The criterion shows good agreement with hydraulic fracturing experiments. It is therefore shown to be capable of predicting the 3D interaction behaviors of HFs intersecting partially/fully cemented NFs.

3.3   INTRODUCTION

Natural Fractures (NFs) are discontinuities in rocks resulting from the stress history of a given formation. NFs can influence the host rock's physical characteristics in many ways, including the overall integrity, anisotropy, mechanical strength, permeability, and fluid/gas storage/transportation properties. According to the relative displacement direction of the fracture interfaces during the formation, NFs can be classified into two types: 1) extension fractures, commonly termed joints or veins, and 2) shear fractures such as faults (Twiss and Moores 1992).

NFs in unconventional, and indeed also many conventional, oil and gas reservoirs are widely observed through core samples, image logs, mineback experiments, and outcrop studies (Warpinski and Teufel 1987; Hennings et al. 2000; Gale et al. 2007, 2014; Jeffrey et al. 2009a). In both field-scale and small-scale hydraulic fracturing experiments, hydraulic fractures (HFs) are observed to be able to cross, cross with offsetting, divert into, or become arrested by NFs (Hanson et al. 1981; Blanton 1982; Teufel and Clark 1984; Warpinski and Teufel 1987; Jeffrey et al. 2009b). Hence, it has long been a concern that NFs can interact with HFs and eventually influence the effectiveness of reservoir stimulation and oil and gas production, both for better and for worse. Microseismic mapping often shows wider event clouds surrounding the HF path in shale reservoirs than conventional sandstone formations, indicating that in some settings the HFs might interact with the NFs in the reservoirs to form highly complex fracture networks (Maxwell et al. 2002; Fisher et al. 2004, 2005; Warpinski et al. 2005). These interactions can also influence the propagation length of the main HF(s), leading to incorrect well spacing, and they can disturb the proppant transport and placement, leading to poor HF conductivity.

The mechanism of the different interaction behaviors is often understood through some now-classical mechanical models. Blanton (Blanton 1982, 1986) derived a criterion which is based on the elastic solution for the stresses in the interaction zone and is a function of the differential in-situ stresses and angle of interaction, while the stress redistribution on the NF induced by the approaching HF tip was not considered. Warpinski and Teufel (Warpinski and Teufel 1987) proposed an analytical model to estimate whether a NF will be dilated or activated (shear slippage) by the HF based on the Coulomb linear friction law. The perturbation of the nearby stress field induced by a dilated NF and the effect of the pore pressure change resulting from fluid leak off on the near-fracture stress field were considered. Renshaw and Pollard (Renshaw and Pollard 1995)

developed an analytical criterion that predicts whether an orthogonally approaching NF will cross a frictional interface. It is based on the near-tip stress field solution from linear elastic fracture mechanics and considers the stress condition when the HF tip is still some distance away from the interface, with a plastic zone (fracture process zone) developed around the HF tip. Extensive studies have also been conducted experimentally and numerically (Blanton 1982; Renshaw and Pollard 1995; Beugelsdijk et al. 2000; Zhang et al. 2007, 2009; Zhou et al. 2008; Olson and Dahi Taleghani 2009; Gu and Weng 2010; Chuprakov et al. 2011; Dahi-Taleghani and Olson 2011), with recent contributions aimed at experimental evaluation of interaction criteria and/or development of more generalized approaches (Gu et al. 2012; Chuprakov et al. 2013).

In spite of these advances, most of the analyses of HF-NF interaction treat NFs as frictional interfaces with no cohesion (Hanson et al. 1981; Blanton 1982; Renshaw and Pollard 1995) or very weak cohesion (Gu and Weng 2010; Gu et al. 2012). Furthermore, almost all studies assume NFs to be continuous with the same properties over the entire NFs. However, NFs in shale reservoirs are nearly always filled with mineralization, and these NFs can naturally be either fully or partially cemented, leading to varying properties along the NFs for the latter case (Laubach 2003; Gale et al. 2007, 2014; Fidler 2011). Indeed, core samples and outcrops from shale reservoirs show that most shale fractures are fully or partially sealed with mineralization. For example, fractures up to 3 m high, 40 m long, <1 mm wide, and partially filled with calcite cement occur in outcrops of the Marcellus Shale (Gale et al. 2014). Also, depending on the cement composition, the cement-to-host rock strength varies widely. For the Barnett Shale (Texas), the cementing material is often calcite. Calcite is usually around half as strong as the intact rock and therefore it may serve as weak cementation during HF treatments (Gale and Holder 2008; Lee et al. 2014). Meanwhile, in the highly siliceous Woodford Shale and tight-gas sandstone reservoirs, it is

common to encounter quartz-filled veins that are stiffer/stronger than the host rock (Gale et al. 2014; Lander and Laubach 2014; Laubach et al. 2016). From a mechanical perspective, the existence of partially or fully cemented NFs with different cementation strength ought to be an important distinction that should lead to differences in HF growth in reservoirs.

Our previous research demonstrated three main patterns in the interaction between HFs and fully/partially cemented NFs: (1) complete crossing, (2) crossing at cemented region(s) with mismatched crack paths at uncemented region(s) (3) no crossing (Fu et al. 2016). Wang and Li (Wang and Li 2017) conducted laboratory-scaled experiments considering the HF's interaction with multiple orthogonal fractures and qualitatively illustrated that cemented NFs do have an effect on the morphology of fracture network. So far, however, there has been very limited published research in this area, and so the mechanism of HFs encountering partially/fully cemented NFs remains unclear. Also, existing analytical models for predicting crossing/no-crossing behavior assume uniform properties on NFs that persist through the entire height of the reservoir/HF (Blanton 1986; Warpinski and Teufel 1987; Renshaw and Pollard 1995; Gu and Weng 2010; Gu et al. 2012). We note that these cases allow treatment of problems within a two-dimensional (2D) framework, but dealing with partial cementation and/or NFs with a height that is less than the reservoir/HF height requires a three-dimensional (3D) framework.

There are no relevant 3D analytical models that account for spatially-varied NF properties, and several fundamentally 3D questions that are of great importance to the fracturing work design remain poorly understood. For example, would partially cemented NFs affect HF propagation differently from uncemented/fully cemented NFs? Do small NFs matter in real hydraulic fracturing applications? Hence, the interaction between HFs and partially-cemented and/or non-persistent (i.e. with height smaller than the reservoir/HF height) NFs comprises a topic with the potential to

contribute important insights into the 3D interaction behaviors and the mechanics behind the complex and multi-strand HF propagation in real reservoirs.

In this paper, we present an analytical criterion for HFs crossing partially-cemented and/or non-persistent NFs. We also present a series of analogue laboratory experiments, firstly as motivation for and, eventually, as quantitative validation of the crossing criterion. The paper therefore begins with a description of these experiments, which, for completeness includes a re-iteration of the experimental data previously presented in Fu et al. (Fu et al. 2016) and expands this data set to include a wider range of contrasts between the rock and NF cementation strength. Once these data are presented in detail, an analytical criterion is presented in 2D, following in the spirit of Renshaw and Pollard (Renshaw and Pollard 1995) but with a subtle, yet important modification to ensure the stress components acting to cross/debond the interface are evaluated at the location where they are maximized. Next, we present the generalization of this 2D criterion into 3D by integrating the stress components acting along the interface over the entire interface height (cemented and uncemented regions) based on a mechanical argument of stress (force) equilibrium. Finally, we show comparisons between the analytical predications and the experimental data, which demonstrate the ability of the criterion to capture the observed behaviors.

3.4   LABORATORY EXPERIMENTS

3.4.1 Experimental Setup

The experimental setup and procedure are similar to what was presented in Fu. et al. (Fu et al. 2016) but here we reiterate some details due to their importance for the experimental design and

the comparison with our criterion. Specimens are loaded symmetrically with hydraulic actuators in a true-triaxial loading frame (Figure 3.1). PMMA spacers are placed around the specimen to promote an evenly distributed compressive stress field. The minimum horizontal stress (σ_{hmin}) is set to zero and a vertical stress (σ_V) is applied to the specimen such that the HF is contained between PMMA plates. The maximum horizontal stress (σ_{Hmax}) is applied to the specimens to attain a sufficient horizontal stress difference and control the HF propagation orientation. Note that HFs will not cross a discontinuity to grow into the PMMA because of the lack of flaws in the PMMA that could nucleate growth.
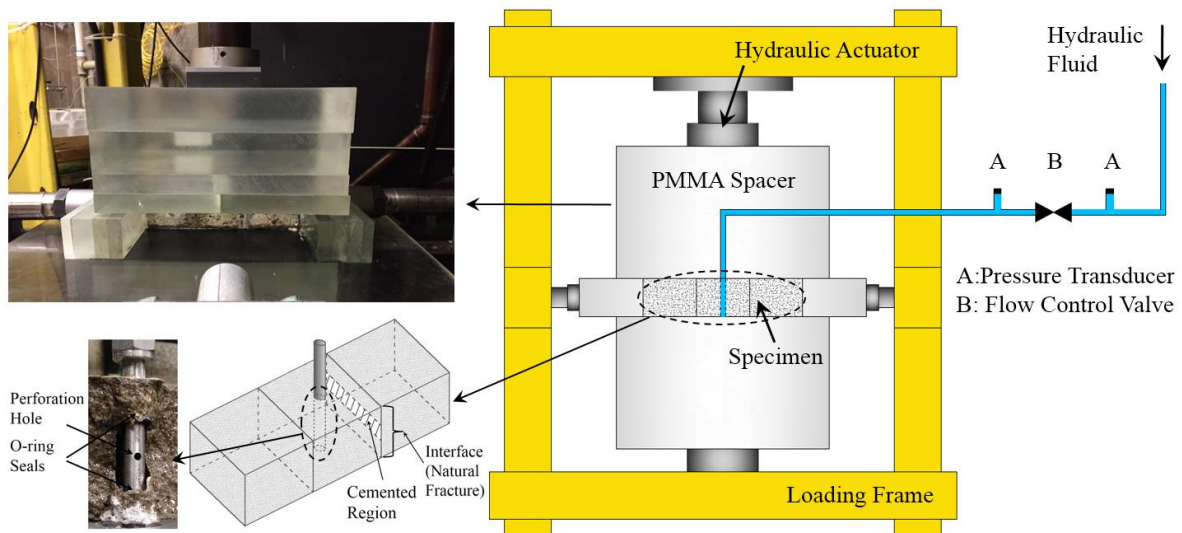
Figure 3.1: Experimental setup and specimen geometry.

The hydraulic fluid used for initiating the HF is a solution of glycerine and water with food dye added to aid in tracking the HF geometry inside the specimen. The viscosity of the solution is 0.3 Pa·s at 20℃ and kept consistent in all experiments. Possible impacts of the role of fluid flow are discussed in Chapter 3.6. The fluid is delivered from an interface vessel pressurized by a

syringe pump with the capability to provide both flow rate control and pressure control. In real reservoirs, the lag region between the fluid front and the fracture tip, or simply the "fluid lag", is expected to be extremely small in comparison with the length of the HF (Economides and Nolte 2000). Therefore it is important to minimize the fluid lag in laboratory experiments in order to make the experiments comparable to the field treatments (Lecampion and Detournay 2007). In our design, fluid lag is minimized by adjusting the viscosity of the fluid and the injection rate, which in turn dictates the fluid tip velocity (Garagash and Detournay 2000). The comparison between the length of surface crack and the wetted region inside the specimen proves that we are able to suppress fluid lag at the scale of observation in these experiments.

At the beginning of the experiment, a constant wellbore fluid pressure of 0.69 MPa (100 psi) is applied briefly in order to monitor for possible leaks in the injecting system. Then the fluid is pumped at a constant volumetric rate of 2.1 ml/min which is maintained throughout the HF growth. Pumping rate, wellbore fluid pressure, fluid pressure at the pump, and confining stresses are recorded during the whole procedure. Specimens are separated manually after the completion of each experiment to enable detailed inspection of HF behavior through the specimen and at the cemented interface.

The specimen geometry is designed such that the HF will be roughly planar and propagate uni-directionally at the time it impinges on the cemented NF. Also, the HF growth is restricted within the host rock layer. This desired growth behavior is achieved using the specimens and loading geometry portrayed in Figure 3.1. The specimens consist of three blocks. The dimensions of each block are 76mm × 76mm × 51mm (3 inches × 3 inches × 2 inches). The interfaces are partially or fully cemented together by an adhesive that can be either weaker or stronger than the matrix material. A 100mm long stainless steel tube, acting as the wellbore casing, is placed in the

central block. This tube has an outer diameter of 9.5 mm and it is perforated over its central region (Figure 3.1). The tube is sealed in place with an adhesive that is stronger than the specimen, using O-rings to define an approximately 25-30 mm long open-hole section in the central part of the 51 mm high specimen. During testing, an axially-oriented HF will be initiated from the center of the wellbore, in the isolated region between two rubber O-rings, as shown in Figure 3.1.

Two synthetic rock-analogue materials are used: Portland cement mortar and concrete. Specimens constructed with mortar consist of a uniformly blended mixture of sand and type N masonry cement and have a fine grain size. The concrete specimens contain larger aggregate and are stronger. All specimens were cured for a 28-day period at 100% humidity. The mechanical properties of the specimens were characterized (Table 3.1) following ASTM Standards or ISRM suggested methods, at laboratory temperature of ~20 °C.

Table 3.1: Mechanical properties of specimens.

Mechanical Property	Unit	Case 1 (Mortar)	Cases 2 and 3 (Mortar)	Case 4 (Concrete)	Test Method
Young's Modulus	GPa	12.1	14.7	25.3	Uniaxial Compression(ASTM: C39/C39M-15a 2012)
Poisson's Ratio	-	0.16	0.17	0.16	
Unconfined Compressive Strength	MPa	12.8	16.8	41.7	
Tensile Strength	MPa	1.75	2.14	3.87	Direct Tension (Surface Pull-off Test) (ASTM International 2010)
Cohesion	MPa	1.81	2.16	4.11	Triaxial Compression (Kovari et al. 1983)
Internal Friction Coefficient	-	0.96	1.03	1.46	
Interface Friction Coefficient	-	0.86	0.83	0.94	Symmetric Direct Shear (Hoskins et al. 1968; Dieterich 1972)

It has been shown in many core samples and outcrops that NFs in shale reservoirs are commonly cemented and typically have small natural apertures (width). NFs observed in four Barnett Shale cores range from 50 μm to 0.2 mm in width with high length/width aspect ratios (>1000:1) (Gale et al. 2007). Core and outcrop data from 18 shale plays also show that most shale-fracture apertures have a size range between 30 μm and 1 mm with an overall decrease in frequency of occurrence for wider apertures (Gale et al. 2014). To promote the physical similarity between the laboratory and field systems, the aperture of the analogue NFs is designed to be very small relative to the dimensions of the laboratory specimens. Also, the strength of cemented NF, as well as the size of the cemented region, is varied systematically. To address these challenges, a suite of adhesives serves as cementation materials, which are able to form very thin cementation layers (sub-millimeter scale) with controllable cemented region size, and provide proper bonding strengths with sufficient repeatability. This is different from the experimental cases presented by Bahorich et al. (Bahorich et al. 2012), in which glass slides are used as strong planar inclusions with a finite thickness of 2.54mm that cannot be neglected.

The shear strength of the cemented interfaces was tested using triaxial compression test following the same approach as Heck and Lane (Heck and Lane 1964), and the tensile strength of the cemented interfaces was tested using direct tension test (pull-off method) with a DYNA pull-off tester, after the adhesives reached full bonding strength (Table 3.2). Note that the cemented interfaces are prepared by gluing the interfaces of the rock specimens directly. Therefore, for interfaces cemented by adhesives that are stronger than the host rock, the strength of the cemented interfaces is limited by the strength of the corresponding host rock material. For example, the 7-day tensile strength of the strong adhesive (Sikadur32-HiMod) determined from standard dumbbell-shaped test specimens is 48 MPa (Corporation 2016), while the tensile strength of the

interfaces in Case 4, although cemented by this strong adhesive, is controlled in its failure by the tensile strength of the corresponding host rock, i.e. it fails at applied tensile stress of 3.87 MPa. We also observe that, for the laboratory tensile/shear strength tests, the failure of the specimens always takes place inside the host rock, instead of the interfaces that are glued together with a thin layer of strong adhesive. Here a word of caution is that, micromechanically, this thin layer of strong adhesive may still alter the interlocking relations between grains of rock materials. Hence, it is possible that rocks with strongly-glued interfaces might show behaviors mechanically different from intact rocks, but we nonetheless proceed with the assumption that these differences between intact rock and strongly glued interfaces will be of secondary importance compared to bonded height and overall bond strength.

Table 3.2: Mechanical properties of cemented interfaces.

Mechanical Properties	Unit	Case 1	Case 2	Case 3	Case 4
Interface Tensile Strength	MPa	1.75	2.14	1.62	3.87
Interface Cohesion	MPa	1.81	2.16	0.90	4.11
Internal Friction Coefficient	-	0.96	1.03	0.89	1.46

3.4.2 Experimental Cases

Four sets of experiments were conducted to study the influence of height and strength of cemented regions in the NFs on the HF propagation (Table 3.3). In each set, a fully-cemented interface experiment is presented as the base test (Figure 3.2a), which is the analogue of the field condition in which a HF encounters a large NF (e.g. long veins) that spans throughout the reservoir height and is fully sealed and cemented (Figure 3.2b and Figure 3.2c). Partially-cemented interface

experiments are presented for comparison (Figure 3.2d and Figure 3.2g), which are the analogue of field conditions when HFs encounter large NFs that persist over the height of the reservoir/HF and are partially filled with mineral cementation (Figure 3.2e, Figure 3.2f, Figure 3.2h and Figure 3.2i).

Table 3.3: Experimental cases.

Test Case	Host Rock Type	Cement-filling Material	Tensile Strength of Cement Relative to Host Rock	Locations of the Cemented regions
Case 1	Mortar	Sikadur32-HiMod	$\gg 1$	Middle of the Interface
Case 2	Mortar	Sikadur32-HiMod	$\gg 1$	Top and Bottom of the Interface
Case 3	Mortar	Elmer's Multi-Purpose Glue	0.76	Middle of the Interface
Case 4	Concrete	Sikadur32-HiMod	$\gg 1$	Middle of the Interface

Note that the strongly and thinly cemented regions in our cases are behaving analogously to intact rock. That is, there is no observable impact of a strong, thin bond relative to intact rock. At a strong bond there is direct, undeviated crossing of the cemented interfaces (as described by Fu et al. (Fu et al. 2016)). Therefore, the experimental findings from the cases with strongly and partially cemented fractures and the analytical criterion developed in this paper also apply to the analogue cases of uncemented fractures with limited height, i.e. uncemented NFs that do not persist over the height of the reservoir.
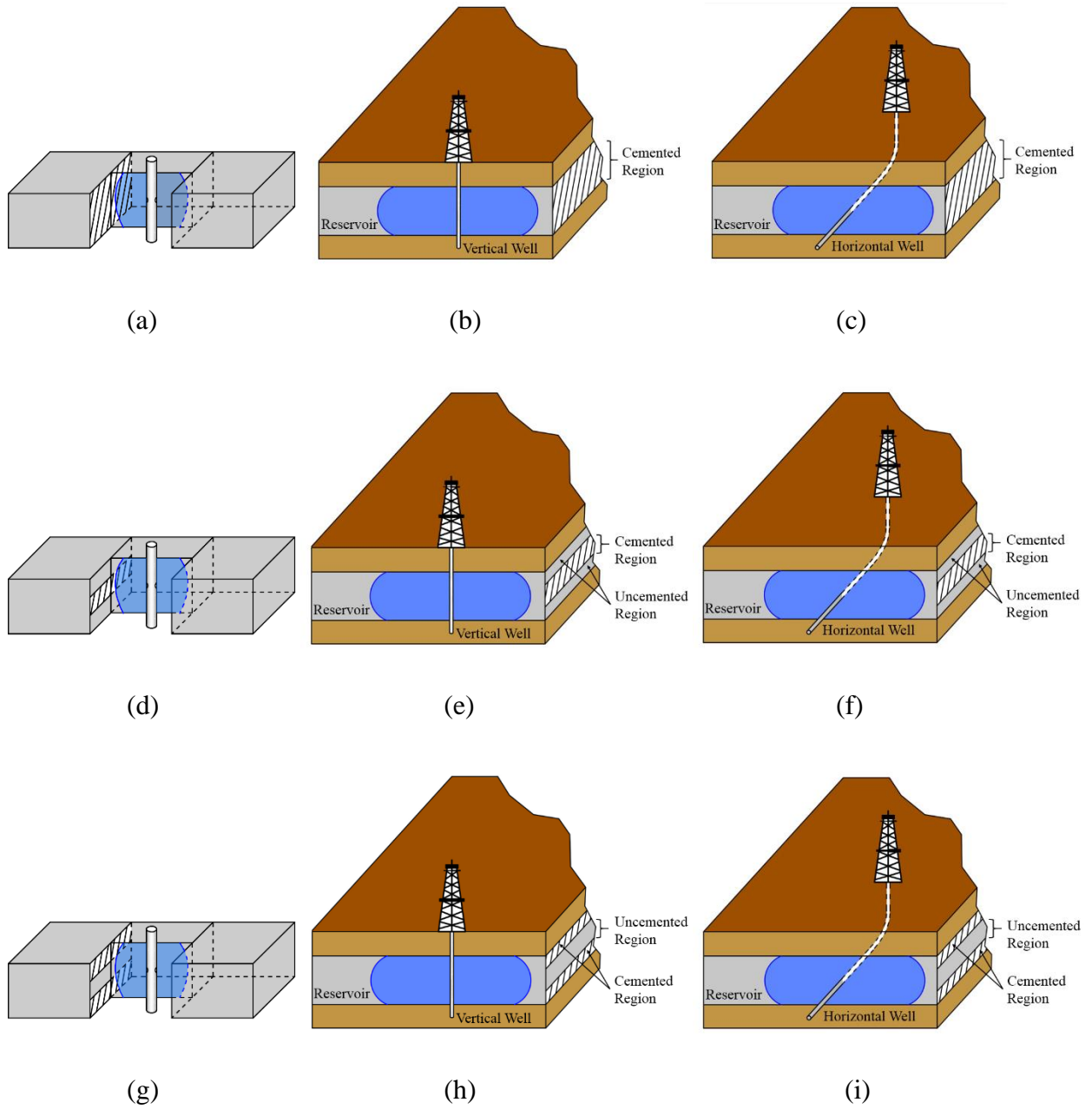
Figure 3.2: Sketches of experimental conditions (a, d, g) and corresponding field examples for vertical (b, e, h) and horizontal (c, f, i) wells.

3.4.3 Experimental Results

Table 3.4-Table 3.7 summarize the experimental conditions and results for the four cases. We previously published some of the experimental results (Cases 1 and 2 from (Fu et al. 2016)), which will be reiterated here along with new experimental results from Cases 3 and 4 (Table 3.6 and Table 3.7). Apparent dependence of crossing/no crossing behaviors was observed on the heterogeneity of NFs, including the proportion of the cemented region/NF height relative to the total reservoir height and the cementation strength.

In all the tested cases, as the proportion of the cemented height to total height of an interface decreases, HF behavior upon interaction with the partially/fully cemented interface is as follows:

a.   Complete crossing when the NF was fully cemented,

b.   Crossing at cemented region(s) with mismatched crack paths at uncemented region(s) when the NF was partially cemented with a relative large cemented region,

c.   No crossing when the NF was partially cemented with a relative small cemented region.

Figure 3.3 and Figure 3.4 show the traces of the HF on the adjacent faces of the blocks forming the interface for Cases 1 and 2. The overlap of two traces indicates the HF crossed the interface directly. Where they do not match, their separation indicates the HF didn't cross the interface at that location. Examining Figure 3.4, we can observe clearly that the overlap of two traces disappears eventually as the proportion of the cemented region (vertical black lines) reduces, indicating a transition of interaction behaviors from complete crossing to no crossing.
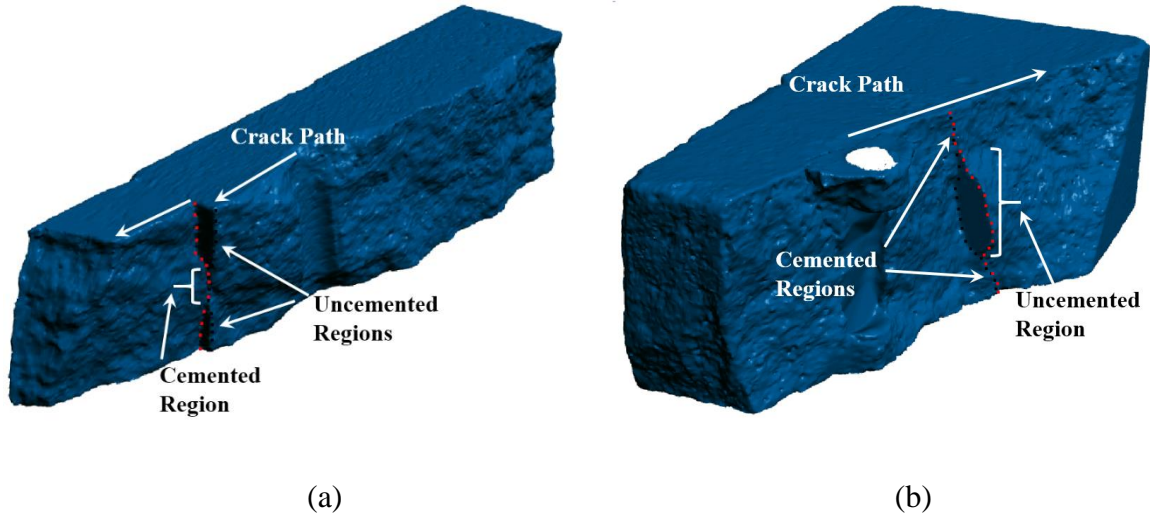
Figure 3.3: 3D digital scan of specimens after testing and manual separation: (a) Case A4; (b) Case B2.

Figure 3.5 shows the influence of NF cementation strength on the proportion of cemented regions that promotes interface crossing. Anticipating that we will demonstrate analytically that cases with interfaces cemented at different regions are equivalent in terms of our crossing criterion, here we compare Cases 2 and 3 directly, regardless of their different cementation locations (Case 2 has top and bottom regions cemented while Case 3 has the middle region cemented). Cases 2 and 3 both use mortar specimens with same mechanical properties, while the cementation material in Case 2 is 32% and 140% stronger in tensile strength and cohesion respectively than that in Case 3. It can be found that, for the same rock matrix, a smaller critical cemented height of the NF is sufficient to promote crossing when the cement filling material is stronger. Figure 3.6 shows selected experimental photos for Cases 2 and 3, in each case the interaction behavior changes from no crossing to crossing as the proportion of the cemented region increases.
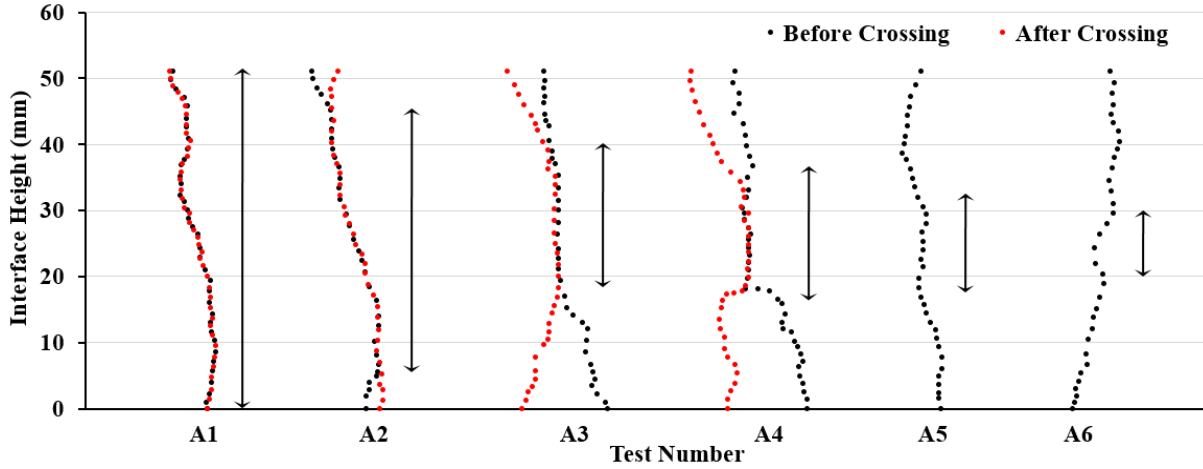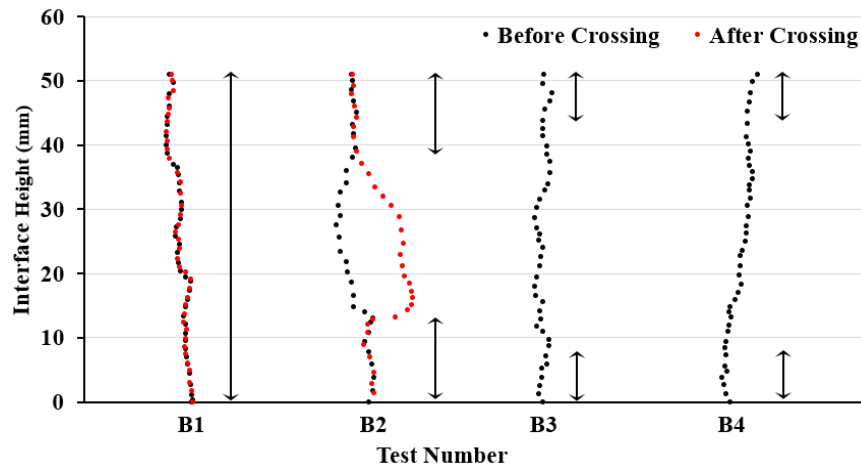
Figure 3.4: Digitized trace of cracks at the partially cemented interface before and after crossing (as illustrated in Figure 3.3), the ratio of the cemented to total height of an interface decreases to the right. Vertical black lines indicate the height and location of cemented regions. (a) Case 1, central region cemented; (b) Case 2, top-bottom region cemented. The HF half-length at the time of intersection with the interface was the same (~38 mm) in all cases (Fu et al. 2016).
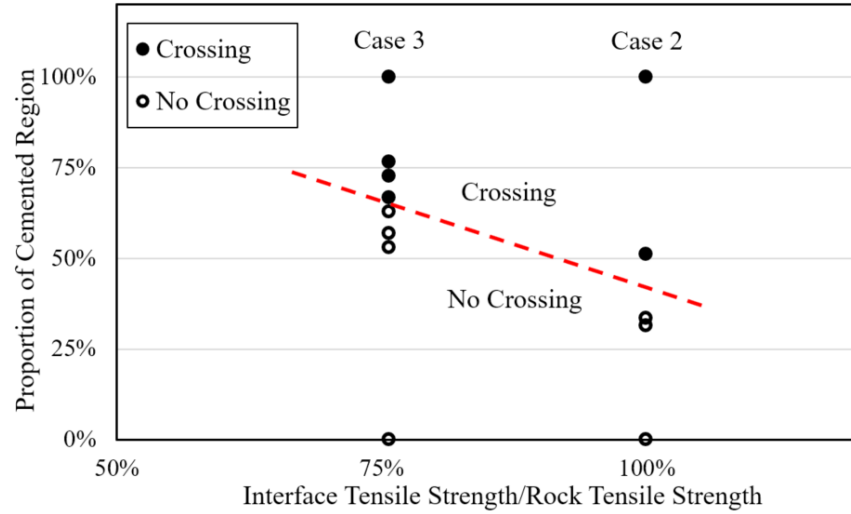
Figure 3.5: The influence of cementation strength on the crossing/no crossing behaviors.
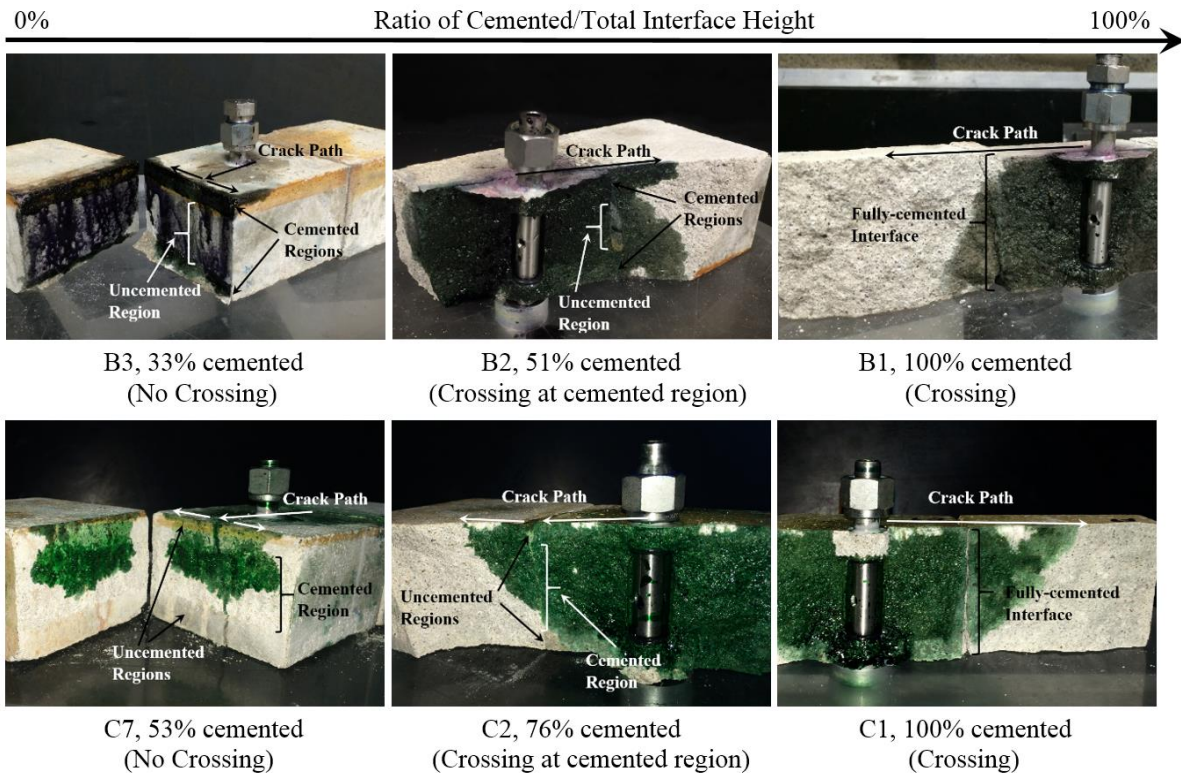
Figure 3.6: The Photos for experiments in Case 2 (B3, B2, B1) and Case 3 (C7, C2, C1).

43

Figure 3.7 shows the influence of rock matrix strength on the proportion of cemented regions that promotes interface crossing. The specimens in Case 4 are made from concrete with a tensile strength 121% stronger than the mortar specimens in Case 1. The interfaces in Cases 1 and 4 are both strongly cemented with the same cementation material. As mentioned before, when the interfaces are thinly cemented with material stronger than the rock matrix, the strength of interface will be limited by the strength of the rock. Therefore, if the experimental data for Cases 1 and 4 are interpreted by the ratio of interface cementation to rock matrix strength, as the cases in Figure 3.5, this ratio will be 100% for both Cases 1 and 4. However, it can be found clearly in Figure 3.7a that there is an apparent dependence on the rock matrix strength; when the rock matrix is stronger, a larger cemented region is needed for the HF to cross the interface. Figure 3.8 summarizes selected experimental photos from Cases 1 and 4, showing the crossing/no crossing behaviors as the rock type/proportion of cemented regions change.

In the previous discussion, the NF is implicitly considered to have a height equal to that of the reservoir, with varying strength cementation over some portion of this height. Alternatively, the strongly cemented regions of the interface in Cases 1 and 4 can be interpreted as equivalent to the intact rock. Therefore, they are analogous to cases in which the reservoir contains uncemented NFs that are shorter than the reservoir height (as discussed in Chapter 3.4.2). Figure 3.7b, then, illustrates the impact of the uncemented NF height on the HF propagation as the rock matrix strength increases. It is shown that when the rock matrix is weaker, HFs are able to cross taller uncemented NFs. In other words, short NFs are more prone to hamper the HF propagation in reservoirs with higher rock matrix strength.

(a)   (b)
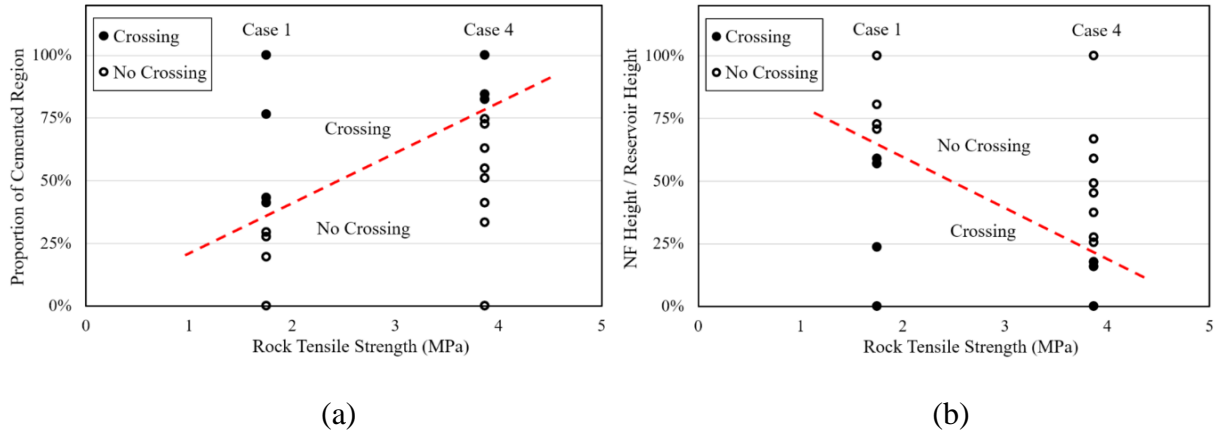
Figure 3.7: The influence of rock matrix strength on the crossing/no crossing behaviors. (a) Interfaces are interpreted as NFs that span throughout the reservoir height and are partially cemented; (b) interfaces are interpreted as uncemented NFs that are shorter than reservoir height.
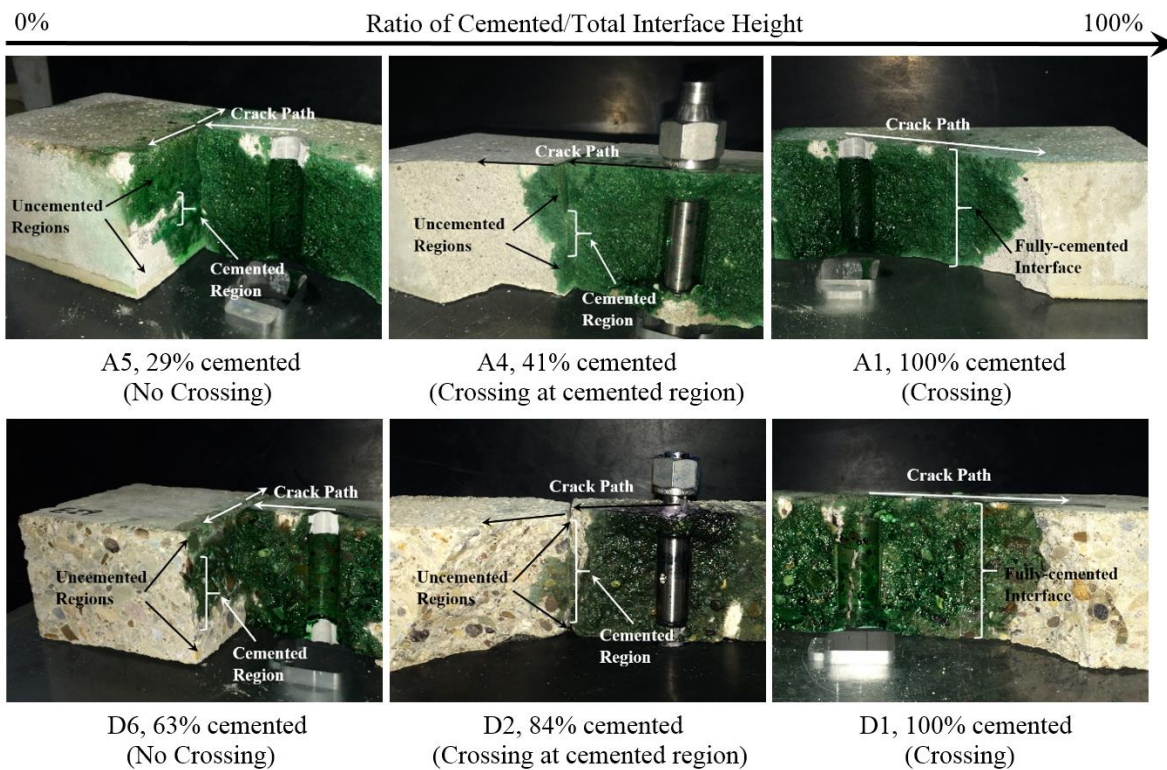
Figure 3.8: Photos for experiments in Case 1 (A5, A4, A1) and Case 4 (D6, D2, D1).

Table 3.4: Summary of experimental conditions and results for Case 1.

Test	Height of Cemented Area (mm)	Cemented Height/ Total Height	σ_V (MPa)	σ_{Hmax} (MPa)	Results
A1	51	100%	1.3	1.1	Crossing
A2	39	76%	1.3	1.1	Crossing at cemented region
A3	22	43%	1.3	1.1	Crossing at cemented region
A4	21	41%	1.3	1.1	Crossing at cemented region
A5	15	29%	1.3	1.1	No crossing
A6	14	27%	1.3	1.1	No crossing
A7	10	20%	1.3	1.1	No crossing
A8	0	0%	1.3	1.1	No crossing

Table 3.5: Summary of experimental conditions and results for Case 2.

Test	Height of Cemented Area (mm)	Cemented Height/ Total Height	σ_V (MPa)	σ_{Hmax} (MPa)	Results
B1	51	100%	1.2	1.0	Crossing
B2	26	51%	1.2	1.0	Crossing at cemented region
B3	17	33%	1.2	1.0	No crossing
B4	16	31%	1.2	1.0	No crossing
B5	0	0%	1.2	1.0	No crossing

Table 3.6: Summary of experimental conditions and results for Case 3.

Test	Height of Cemented Area (mm)	Cemented Height/ Total Height	σ_V (MPa)	σ_{Hmax} (MPa)	Results
C1	51	100%	1.4	1.2	Crossing
C2	39	76%	1.4	1.2	Crossing at cemented region
C3	37	73%	1.4	1.2	Crossing at cemented region
C4	34	67%	1.4	1.2	Crossing at cemented region
C5	32	63%	1.4	1.2	No crossing
C6	29	57%	1.4	1.2	No crossing
C7	27	53%	1.4	1.2	No crossing
C8	0	0%	1.4	1.2	No crossing

Table 3.7: Summary of experimental conditions and results for Case 4.

Test	Height of Cemented Area (mm)	Cemented Height/ Total Height	σ_V (MPa)	σ_{Hmax} (MPa)	Results
D1	51	100%	1.4	1.2	Crossing
D2	43	84%	1.4	1.2	Crossing at cemented region
D3	42	82%	1.4	1.2	Crossing at cemented region
D4	38	75%	1.4	1.2	No Crossing
D5	37	73%	1.4	1.2	No crossing
D6	32	63%	1.4	1.2	No crossing
D7	28	55%	1.4	1.2	No crossing
D8	26	51%	1.4	1.2	No crossing
D9	21	41%	1.4	1.2	No crossing
D10	17	33%	1.4	1.2	No crossing
D11	0	0%	1.4	1.2	No crossing

3.5   ANALYTICAL MODELING

In this section, we develop an analytical model that accounts for the NF properties, including the variation of cement strengths, the proportion of the cemented region(s), and the NF height. We start by deriving a 2D criterion that is based on near-tip stress field solution from linear elastic fracture mechanics and considers the crack tip plasticity during the fracture propagation. The approach is similar to that of the Renshaw-Pollard (R-P) Criterion (Renshaw and Pollard 1995), but with a subtle, yet important modification to ensure the stress components acting to cross/debond the interface are evaluated when they are maximized, instead of at the same locations where $\theta = \pm 90°$ (Figure 3.11d). Then we extend the 2D criterion to a 3D criterion by integrating the stress components acting along the interface over the entire interface height (cemented regions and uncemented regions) based on global force equilibrium.

3.5.1   Analytical Criterion in 2D

For a homogenous, isotropic solid, the crack tip stress field for a Mode I crack can be obtained from linear elastic stress analysis (Irwin 1957):

$$
\begin{Bmatrix} \sigma_{xx}(\theta) \\ \sigma_{yy}(\theta) \\ \tau_{xy}(\theta) \end{Bmatrix} = \frac{K_I}{\sqrt{2\pi R}} \begin{Bmatrix} \cos\left(\frac{\theta}{2}\right)\left[1 - \sin\left(\frac{\theta}{2}\right)\sin\left(\frac{3\theta}{2}\right)\right] \\ \cos\left(\frac{\theta}{2}\right)\left[1 + \sin\left(\frac{\theta}{2}\right)\sin\left(\frac{3\theta}{2}\right)\right] \\ \sin\left(\frac{\theta}{2}\right)\cos\left(\frac{\theta}{2}\right)\cos\left(\frac{3\theta}{2}\right) \end{Bmatrix} \qquad (3.1)
$$

where $\sigma_{xx}(\theta), \sigma_{yy}(\theta)$ and $\tau_{xy}(\theta)$ are the crack-induced stresses, K_I is the Mode I stress intensity

factor, and R and θ are the polar coordinates illustrated in Figure 3.9. The above equations are valid provided that inelastic or otherwise non-linear behavior in any region is negligibly small compared with the scale of the crack. It is recognized, however, that a non-linear zone exists at/near the crack tip characterized by progressive softening, for which the stress decreases at increasing deformation and prevents the stresses from being infinite at the crack tip. The size of the inelastic zone, also known as the fracture process zone (FPZ), is dependent on the material's microstructure, loading rate, grain size and specimen type (Labuz et al. 1987). A simple estimate of the FPZ size for elastic/perfectly-plastic materials was proposed by Irwin (Irwin 1960), which assumes the limit of the admissible stress in the FPZ equal to the yield strength. Similar to Irwin's solution, the size of the FPZ for quasi-brittle materials can be roughly estimated by assuming that the crack tip has already completely softened and the boundary of the FPZ just starts to soften. The length of the FPZ at the $\theta = 0°$ direction will be double that of Irwin's estimate, or perhaps even bigger, depending on whether one assumes a linear or parabolic stress distribution in the zone (Bažant and Planas 1997).

An accurate estimate of the size of the FPZ is largely influenced by the material property and loading configurations. The estimation becomes more difficult for quasi-brittle materials because of the physical and mechanical heterogeneity. It is common to assume that the stresses within the FPZ are equal to or less than the stresses at the boundary of the FPZ because of plastic deformation and stress relaxation. We will employ the same assumption as in the *R-P Criterion* (Renshaw and Pollard 1995), namely that there exists some critical radius R_{FPZ} at the boundary of the FPZ around the crack tip. We also consider a fracture propagating orthogonally towards an interface (pre-existing NF). The thickness of the interface is assumed to be infinitely small and the material before and after the interface is homogeneous with the same mechanical and physical

properties. Hence, Equation 3.1 will hold in the regions outside of the FPZ. The interface of the

pre-existing fracture is assumed to follow the Mohr–Coulomb failure criterion.

Now, let a small distance r be the horizontal separation between the crack tip and the

interface and $R = r/\cos\theta$. Equation 3.1 can then be rewritten as:

$$
\begin{Bmatrix} \sigma_{xx}(\theta) \\ \sigma_{yy}(\theta) \\ \tau_{xy}(\theta) \end{Bmatrix} = \frac{K_I}{\sqrt{2\pi r}} \begin{Bmatrix} \varphi_{xx}(\theta) \\ \varphi_{yy}(\theta) \\ \varphi_{xy}(\theta) \end{Bmatrix},
$$

$$
\text{where } \begin{Bmatrix} \varphi_{xx}(\theta) \\ \varphi_{yy}(\theta) \\ \varphi_{xy}(\theta) \end{Bmatrix} = \begin{Bmatrix} \sqrt{\cos\theta}\cos\left(\dfrac{\theta}{2}\right)\left[1 - \sin\left(\dfrac{\theta}{2}\right)\sin\left(\dfrac{3\theta}{2}\right)\right] \\ \sqrt{\cos\theta}\cos\left(\dfrac{\theta}{2}\right)\left[1 + \sin\left(\dfrac{\theta}{2}\right)\sin\left(\dfrac{3\theta}{2}\right)\right] \\ \sqrt{\cos\theta}\sin\left(\dfrac{\theta}{2}\right)\cos\left(\dfrac{\theta}{2}\right)\cos\left(\dfrac{3\theta}{2}\right) \end{Bmatrix} \tag{3.2}
$$

where $\varphi_{xx}(\theta), \varphi_{yy}(\theta)$ and $\varphi_{xy}(\theta)$ are defined as the stress coefficients. For a certain r, the stress

coefficients indicate the magnitude of σ_{xx}, σ_{yy} and σ_{xy} along the interface. The magnitude of

σ_{xx}, σ_{yy} and σ_{xy} at the interface can thus be readily obtained from Equation 3.2. For a crack with

the distance of r away from the interface, the crack-induced stresses will maximize at different

locations along the interface (Figure 3.10). Specifically:

$$
\begin{cases} \sigma_{xx(max)} = \sigma_{xx(\theta=\pm0°)} \\ \sigma_{yy(max)} = \sigma_{yy(\theta=\pm36°)} \\ \left|\tau_{xy(max)}\right| = \left|\tau_{xy(\theta=\pm30°)}\right| \end{cases} \tag{3.3}
$$

Now consider the interaction between an orthogonally approaching HF and a pre-existing

NF, our criterion can be stated as follows: no interface slipping or opening have occurred when

the stress components that promote interface crossing are maximized and sufficient to initiate a

fracture on the interface. Specifically, for the HF to cross the NF, the following three criteria must

all be satisfied.
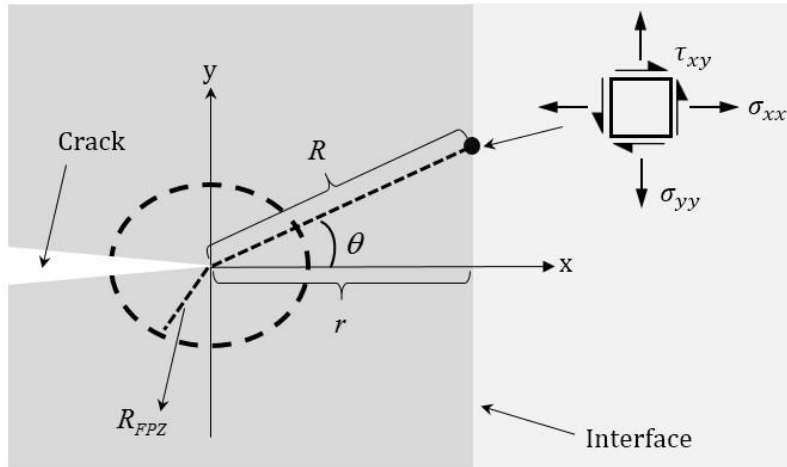
Figure 3.9: Crack induced stress components. All stresses are drawn as positive.
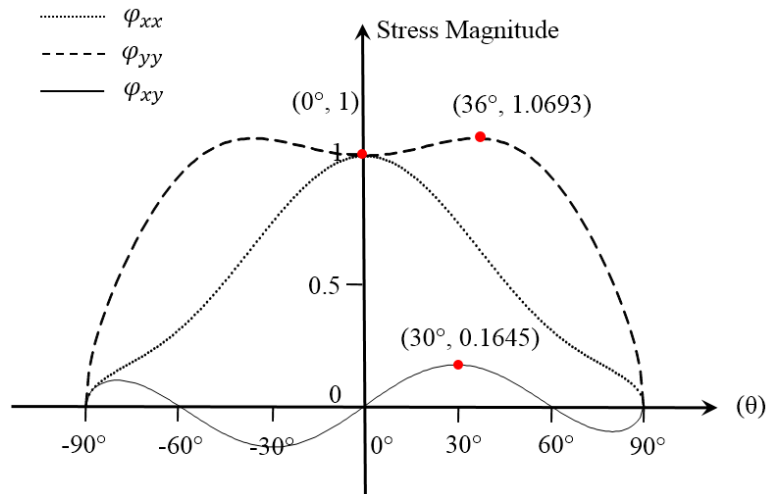
Figure 3.10: The magnitude of crack induced stresses at the interface.

2D Criterion 1 (Fracture Initiation): The maximum stress that promotes crack nucleation by exceeding the tensile strength of the rock is sufficient to initiate a new fracture somewhere on the opposite side of the NF interface:

$$\sigma_{yy}(\theta) + \sigma_{yy}^r = T_0, \exists \, \theta = \theta_{crossing} \in (-90°, 90°) \tag{3.4}$$

where T_0 is the tensile strength of the rock, $\sigma_{xx}^r, \sigma_{yy}^r, \tau_{xy}^r$ are the in-situ stresses, and $\theta_{crossing}$ is the angle at which the stress that promotes crack nucleation reaches its maximum.

2D Criterion 2 (No-NF Tensile Failure): The tensile strength of the NF is sufficient to prevent any opening along the NF before the fracture initiation occurs:

$$A_0 > \sigma_{xx}(\theta) + \sigma_{xx}^r, \forall \, \theta \in \left[-\left|\theta_{crossing}\right|, \left|\theta_{crossing}\right|\right] \tag{3.5}$$

where A_0 is the tensile strength of the cemented interface.

2D Criterion 3 (No-NF Shear Failure): The shear resistance of the NF is sufficient to prevent any slippage along the NF before the fracture initiation occurs:

$$C_0 - \mu[\sigma_{xx}(\theta) + \sigma_{xx}^r] > \left|\tau_{xy}(\theta) + \tau_{xy}^r\right|, \forall \, \theta \in \left[-\left|\theta_{crossing}\right|, \left|\theta_{crossing}\right|\right] \tag{3.6}$$

where C_0 and μ are the cohesion and friction coefficient of the cemented interface.

Examining the *2D Criterion 1* (Equation 3.4), we notice that the left side of the equation, the stress that promotes fracture initiation, will maximize when $\sigma_{yy}(\theta)$ peaks. Now consider the process of a crack growing orthogonally towards a pre-existing NF with a FPZ developing around the crack tip (Figure 3.11), the stresses inside the FPZ are assumed equal to or less than the stresses at the boundary. In order for the $\sigma_{yy}(\theta)$ acting on the NF to reach its maximum, the crack should propagate until the boundary of the PFZ intersects the NF at $\theta = \pm 36°$ (Figure 3.11c). Therefore, it will be possible for the HF to initiate a new fracture on the NF if the *2D Criterion 1* holds at $(\theta = \theta_{crossing} = \pm 36°, R = R_{FPZ})$.

Once the locations where the possibility of fracture initiation peaks are obtained, *2D Criteria 2* and 3 should hold for every $\theta \in \left[-\left|\theta_{crossing}\right|, \left|\theta_{crossing}\right|\right]$, assuming that the radius of the fracture process zone (R_{FPZ}) is the same. That is, to ensure that no interface opening or slipping take place before the fracture initiation occurs, Equations 3.5 and 3.6 should both hold from the moment when the boundary of the FPZ first contacts the NF at $\theta = 0°$ to the moment when the boundary of the PFZ intersects the NF at $\theta = \pm36°$.

For *2D Criterion 2*, the stress that promotes interface opening, the right side of Equation 3.5 will maximize when $\sigma_{xx}(\theta)$ reaches its maximum in the range of $\theta \in [-36°, 36°]$. It can be readily obtained that $\sigma_{xx}(\theta)$ acting on the NF peaks at the moment when the boundary of the FPZ first contacts the NF at $\theta = 0°$ (Figure 3.11a). Therefore, no opening will take place on any part of the NF as long as the *2D Criterion 2* holds at ($\theta = \theta_{opening} = 0°, R = R_{FPZ}$).

Similarly, for *2D Criterion 3* to hold in the range of $\theta \in [-36°, 36°]$, we substitute Equation 3.1 into Equation 3.6 to find:

$$\frac{(C_0 - \mu\sigma_{xx}^r)\sqrt{2\pi R_{FPZ}}}{K_I} > \left\{\left|\sin\left(\frac{\theta}{2}\right)\cos\left(\frac{\theta}{2}\right)\cos\left(\frac{3\theta}{2}\right)\right| + \cos\left(\frac{\theta}{2}\right)\left[1 - \sin\left(\frac{\theta}{2}\right)\sin\left(\frac{3\theta}{2}\right)\right]\right\} \quad (3.7)$$

Here $\tau_{xy}^r = 0$, since the HF propagates perpendicularly to the minimum principle stress. It can then be obtained from Equation 3.7 that the stress which promotes the NF slippage attains its maximum when the boundary of the FPZ intersects the NF at a certain $\theta = \theta_{slipping}$. This critical angle depends on the friction coefficient of the NF. For example, when μ changes from 0.01 to 1, $\theta_{slipping}$ changes from $\pm31.3°$ to $\pm13.6°$. The slippage of the NF will be suppressed as long as *2D Criterion 3* holds at ($\theta = \theta_{slipping}, R = R_{FPZ}$).

It is to be noted that in Renshaw and Pollard's approach, the maximum magnitude of the stress components $(\sigma_{ij})_{max}$ along the interface was evaluated at the top and bottom edges of an assumed FPZ when $\theta = \pm 90°$ (Figure 3.11d), while in our case, we evaluate the stress components that promote interface crossing/debonding at the locations of their maximum as the HF approaches.

(a)

(b)

(c)

(d)
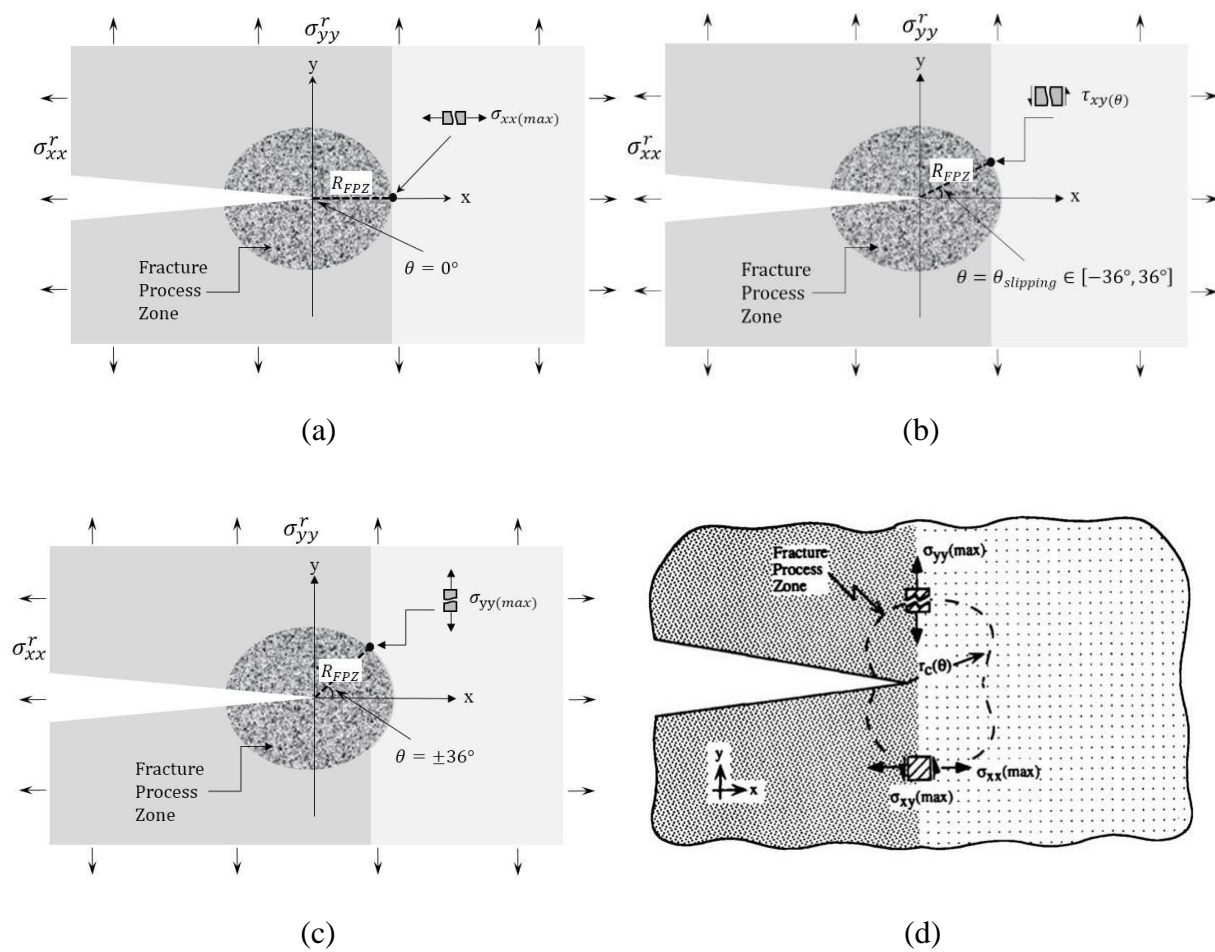
Figure 3.11: (a), (b), and (c) A fracture approaching an interface; (d) geometry of the fracture propagation in *R-P Criterion* (Renshaw and Pollard 1995). All stresses are drawn as positive.
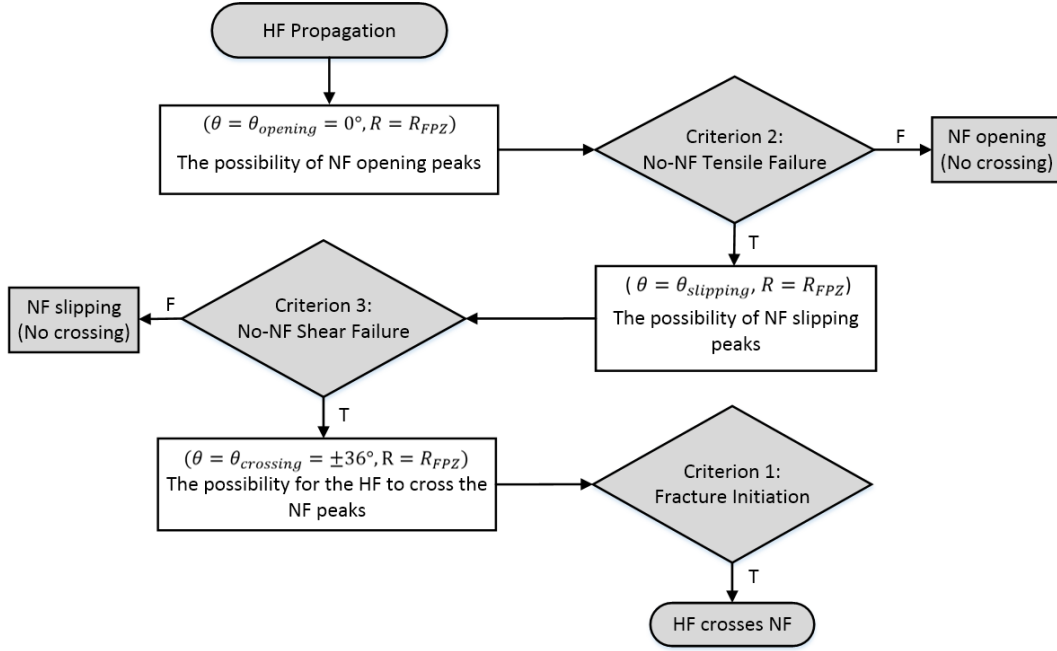
Figure 3.12: The algorithm for evaluating the crossing/no crossing behaviors.

The 2D criterion for evaluating the crossing/no crossing behaviors during the fracture propagation can be obtained following the algorithm illustrated in Figure 3.12, the threshold for fracture initiation on the NF will be evaluated when both tension and shear failures along the NF are suppressed. Following this algorithm, for *2D Criterion 2*, substituting $\theta = 0°$ and Equation 3.1 into Equation 3.5 gives

$$A_0 - \sigma_{xx}^r > \frac{K_I}{\sqrt{2\pi R_{FPZ}}} \cos(0°)[1 - \sin(0°)\sin(0°)] \tag{3.8}$$

For *2D Criterion 3*, the following is obtained similarly by substituting Equation 3.1 into Equation 3.6:

$$C_0 - \mu\sigma_{xx}^r > \frac{K_I}{\sqrt{2\pi R_{FPZ}}}\left\{\left|\sin\left(\frac{\theta}{2}\right)\cos\left(\frac{\theta}{2}\right)\cos\left(\frac{3\theta}{2}\right)\right| + \mu\cos\left(\frac{\theta}{2}\right)\left[1 - \sin\left(\frac{\theta}{2}\right)\sin\left(\frac{3\theta}{2}\right)\right]\right\} \tag{3.9}$$

For *2D Criterion 1*, substituting $\theta = \pm 36°$ and Equation 3.1 in to Equation 3.4 leads to

$$\frac{K_I}{\sqrt{2\pi R_{FPZ}}}\cos\left(\pm\frac{36°}{2}\right)\left[1 - \sin\left(\pm\frac{36°}{2}\right)\sin\left(3\cdot\pm\frac{36°}{2}\right)\right] + \sigma_{yy}^r = T_0 \tag{3.10}$$

This gives

$$\sqrt{2\pi R_{FPZ}} = 1.1888\frac{K_I}{T_0 - \sigma_{yy}^r} \tag{3.11}$$

Equations 3.8 and 3.9 can then be rewritten as follows respectively by substituting Equation 3.11:

$$\frac{A_0 - \sigma_{xx}^r}{T_0 - \sigma_{yy}^r} > 0.8412 \qquad \textbf{(2D Interface Opening Threshold)} \tag{3.12}$$

$$\frac{\frac{C_0}{\mu} - \sigma_{xx}^r}{T_0 - \sigma_{yy}^r} > \frac{\cos\left(\frac{\theta}{2}\right)\left[1 - \sin\left(\frac{\theta}{2}\right)\sin\left(\frac{3\theta}{2}\right)\right] + \frac{\left|\sin\left(\frac{\theta}{2}\right)\cos\left(\frac{\theta}{2}\right)\cos\left(\frac{3\theta}{2}\right)\right|}{\mu}}{1.1888}, \quad \theta \in [-36°, 36°]$$

$$\textbf{(2D Interface Slipping Threshold)} \tag{3.13}$$

For convenience, an explicit expression for Equation 3.13 can be further obtained by plotting its numerical solution and then using Least Squares curve fitting method, with the coefficient of determination value (R-square) of 0.999:

$$\frac{\frac{C_0}{\mu} - \sigma_{xx}^r}{T_0 - \sigma_{yy}^r} > \frac{0.1467}{\mu} + 0.7301, \mu \in (0, 1.5] \tag{3.14}$$

The HF is thus predicted to cross the fully cemented/uncemented NF as long as both Equations 3.12 and 3.13 are satisfied.
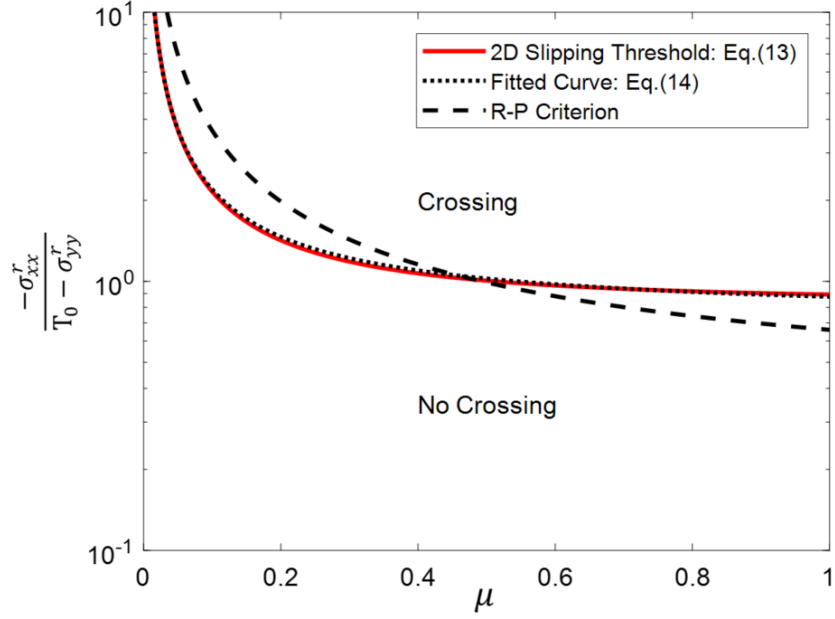
Figure 3.13: Comparison between the 2D Slipping Threshold and the *R-P Criterion*.

Figure 3.13 shows the comparison between the 2D Slipping Threshold and the *R-P Criterion* in a semilogarithmic coordinate system for the special case of zero interface tensile strength and cohesion. The friction coefficient is chosen to be within (0, 1]. The parametric space above each curve represents the crossing condition. As shown in the figure, the two criteria agree when the interface friction coefficient is around 0.5. For small friction coefficient (e.g., smaller than 0.4), the interface crossing condition is more easily satisfied based on our criterion than for the *R-P Criterion*. For relatively large friction coefficient (e.g., larger than 0.5), our criterion predicts a higher limit on stress conditions that result in interface crossing and becomes less dependent on the friction coefficient compared to the *R-P Criterion*. This agrees with the experimental observations presented by Bunger et al. (Bunger et al. 2015), in which the crossing/no crossing behaviors of three sets of experiments appear to be relatively independent of the friction coefficient, whereby a lower stress limit was needed to promote interface crossing for cases with

small friction coefficient (Adelaide Black Granite with 0.17 friction coefficient) while a higher stress limit was needed to achieve interface crossing for cases with large friction coefficient (Wondabyne Sandstone with 0.76 friction coefficient) compared to the prediction from the *R-P Criterion* (Renshaw and Pollard 1995). While Bunger et al. (Bunger et al. 2015) suggests this relatively small dependence on friction coefficient can be an evidence of the importance of fluid flow, our analysis shows that additionally there is a reduced impact of the friction coefficient comparing to the *R-P Criterion* that is a direct consequence of the different locations on the interface (NF) at which the stresses are evaluated.

3.5.2 Analytical Criterion in 3D

After obtaining the 2D criterion, we next generalize it into a quasi-3D criterion by integrating the stress components over the entire interface height based on a mechanical requirement of global force equilibrium. The problem geometry is given by Figure 3.14, which shows a 3D model in which a crack propagates orthogonally towards a partially-cemented NF with an inelastic zone (FPZ) developing around the crack tip. The hatched area (Region A) denotes the cemented region of the NF. Similar to our 2D criterion, we assume: 1) that there exists some critical radius R_{FPZ} which determines the boundary of the crack process zone; 2) the thickness of the interface for both cemented regions and uncemented regions is infinitely small so that the existence of the interface will not disturb the crack tip stress distribution; 3) the materials before and after the NF interface are homogeneous and isotropic; and 4) the interface obeys the Mohr–Coulomb failure criterion.
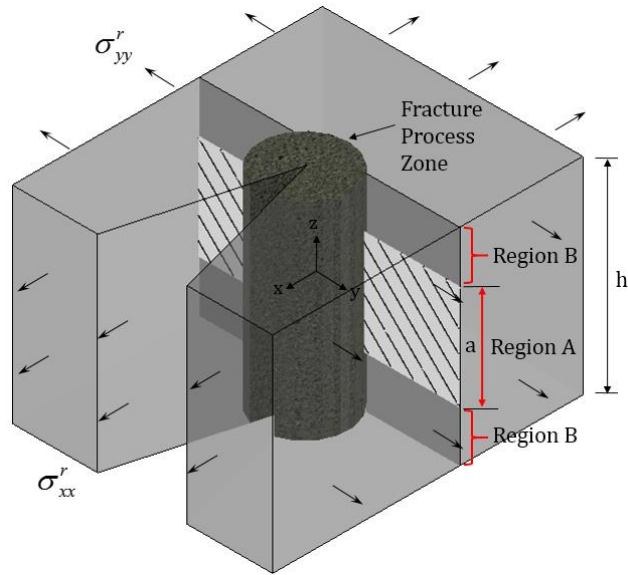
(a)
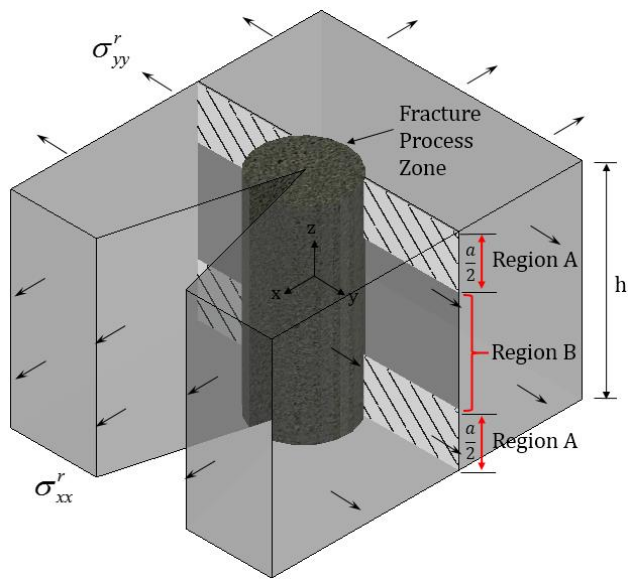
(b)

Figure 3.14: A crack propagating orthogonally towards a partially-cemented interface, Region A is cemented, Region B is uncemented. (a) Central-region cemented interface; (b) top-bottom region cemented interface. All stresses are drawn as positive.

The basic premise of the generalization is, mathematically, to 1) add an explicit constraint of reservoir layer height to the 2D Criterion 1 (Equation 3.4), and, 2) to integrate both sides of the 2D criteria 2 and 3, Equations 3.5 and 3.6, from the bottom to the top of the reservoir layer (-h/2 to h/2). Similar to the 2D Criterion, A_0 and C_0 are used to denote the tensile strength and cohesion of the cemented region(s) (Region A in Figure 3.14). We also define A_u and C_u as the tensile strength and cohesion of the uncemented region(s) (Region B in Figure 3.14) so that a more generalized criterion can be derived, although these two parameters are zero in our experimental cases. This mathematical premise corresponds to a physical argument that global force equilibrium requires the NF to react to the stresses generated by the approaching HF. Our criterion for a crack to cross a partially-cemented interface in 3D space can then be stated as follows:

3D Criterion 1 (Fracture Initiation): The maximum stress along the NF that promotes crack nucleation is sufficient to initiate a fracture on the opposite side of the NF interface:

$$\sigma_{yy}(\theta) + \sigma_{yy}^r = T_0, \exists\, \theta = \theta_{crossing} \in (-90°, 90°), \;\; x > 0^+, z \in \left[-\frac{h}{2}, \frac{h}{2}\right] \qquad (3.15)$$

Note that this local condition for crack nucleation requires only that the tensile stresses generated by the approaching HF are sufficient to exceed the tensile strength somewhere on the opposite side of the NF.

3D Criterion 2 (No-NF Tensile Failure): The total tensile strength over the entire height of the NF is sufficient to prevent any opening along the NF before the fracture initiation occurs:

$$\int_{-\frac{h}{2}}^{-\frac{a}{2}} A_u dz + \int_{-\frac{a}{2}}^{\frac{a}{2}} A_0 dz + \int_{\frac{a}{2}}^{\frac{h}{2}} A_u dz > \int_{-\frac{h}{2}}^{\frac{h}{2}} [\sigma_{xx}(\theta) + \sigma_{xx}^r]\, dz, \forall\, \theta \in \left[-|\theta_{crossing}|, |\theta_{crossing}|\right] (3.16)$$

3D Criterion 3 (No-NF Shear Failure): The total shear resistance over the entire height of the NF is sufficient to prevent any slippage along the NF before the fracture initiation occurs:

60

$$\int_{-h/2}^{-a/2} \{Cu - \mu_u[\sigma_{xx}(\theta) + \sigma_{xx}^r]\}dz + \int_{-a/2}^{a/2} \{C_0 - \mu_c[\sigma_{xx}(\theta) + \sigma_{xx}^r]\} dz +$$

$$\int_{a/2}^{h/2} \{Cu - \mu_u[\sigma_{xx}(\theta) + \sigma_{xx}^r]\}dz > \int_{-\frac{h}{2}}^{\frac{h}{2}} [|\tau_{xy}(\theta) + \tau_{xy}^r|]dz, \forall\, \theta \in \left[-|\theta_{crossing}|, |\theta_{crossing}|\right] (3.17)$$

In all of these equations, z is the coordinate in the direction of the NF height in Cartesian coordinates, a is the height of the cemented region, h is the height of the interface, μ_c is the friction coefficient of the cemented region, and μ_u is the friction coefficient of the uncemented region. Note that equations are derived based on Figure 3.14a, but also apply to the case illustrated in Figure 3.14b because the resulting integral will evaluate to the same final expressions. We observe from the previous 2D criterion that for an approaching crack, the crack-induced tensile stress that promotes interface opening reaches its maximum when the PFZ first contacts the interface at $\theta = \theta_{opening} = 0°$. Also we obtained that the maximized propensity for interface slipping occurs at the moment when the FPZ intersects the interface and at $\theta = \theta_{slipping}$, depending on the friction coefficient of the interface. At last, the crack-induced tensile stress which promotes crack nucleation peaks at the moment when the FPZ intersects the interface and at $\theta = \theta_{crossing} = \pm 36°$. Following a similar algorithm as for the 2D criterion (Figure 3.12), the 3D criterion for evaluating the crossing-no crossing behaviors of a HF interacting with a partially/fully cemented NF can be readily obtained. Namely, for a HF to cross the interface, 3D Criterion 1, substituting $\theta = \pm 36°$ and Equation 3.1 into Equation 3.15, yields $\sqrt{2\pi R_{FPZ}} = 1.1888 \frac{K_I}{T_0 - \sigma_{yy}^r}$, which we note is the same as Equation 3.11.

Additionally, to ensure that no interface opening is induced during the crack propagation, rearranging 3D Criterion 2 by substituting $\theta = 0°$ and Equation 3.1 into Equation 3.16 leads to

$$\int_{-\frac{h}{2}}^{-\frac{a}{2}} Au\, dz + \int_{-\frac{a}{2}}^{\frac{a}{2}} A_0\, dz + \int_{\frac{a}{2}}^{\frac{h}{2}} Au \cdot dz > \int_{-\frac{h}{2}}^{\frac{h}{2}} \left[\frac{K_I}{\sqrt{2\pi R_{FPZ}}} \cos(0°)[1 - \sin(0°)\sin(0°)] + \sigma_{xx}^r \right] dz (3.18)$$

61

Substituting Equation 3.11 into Equation 3.18 yields the condition under which no opening will be induced along the interface:

$$\frac{\frac{(h-a)A_u+aA_0}{h}-\sigma_{xx}^r}{T_0-\sigma_{yy}^r} > 0.8412 \qquad \textbf{(3D Interface Opening Threshold)} \qquad (3.19)$$

Similarly, for *3D Criterion 3* to hold such that no interface slipping is induced along the interface, substituting Equations 3.1 and 3.11 into Equation 3.17:

$$\frac{\frac{(h-a)C_u+aC_0}{h\bar{\mu}}-\sigma_{xx}^r}{T_0-\sigma_{yy}^r} > \frac{\cos\left(\frac{\theta}{2}\right)\left[1-\sin\left(\frac{\theta}{2}\right)\sin\left(\frac{3\theta}{2}\right)\right]+\frac{\left|\sin\left(\frac{\theta}{2}\right)\cos\left(\frac{\theta}{2}\right)\cos\left(\frac{3\theta}{2}\right)\right|}{\bar{\mu}}}{1.1888},$$

$$\theta \in [-36°, 36°] \qquad \textbf{(3D Interface Slipping Threshold)} \qquad (3.20)$$

where $\bar{\mu} = \frac{(h-a)\mu_u+a\mu_c}{h}$ is the weighted friction coefficient over the entire NF. An explicit expression for Equation 3.20 can be obtained using Least Squares curve fitting method to the numerical solution of Equation 3.20 (R-square=0.999), resulting in

$$\frac{\frac{(h-a)C_u+aC_0}{h\bar{\mu}}-\sigma_{xx}^r}{T_0-\sigma_{yy}^r} > \frac{0.1467}{\bar{\mu}}+0.7301, \bar{\mu} \in (0, 1.5] \qquad (3.21)$$

A HF is therefore predicted to cross a partially-cemented interface when both Equations 3.19 and 3.20 are satisfied.

Note that the left side of Equation 3.19 ($\frac{\frac{(h-a)A_u+aA_0}{h}-\sigma_{xx}^r}{T_0-\sigma_{yy}^r}$) is a dimensionless parameter group which compares the interface opening resistance to the fracture initiation resistance, and so we henceforth employ the terminology "Interface Opening Potential". The left side of Equation 3.20 ($\frac{\frac{(h-a)C_u+aC_0}{h\bar{\mu}}-\sigma_{xx}^r}{T_0-\sigma_{yy}^r}$) is a dimensionless parameter group which compares the interface slipping resistance to the fracture initiation resistance and we therefore employ the terminology "Interface Slipping Potential". It is important to note that:

- When Region A represents cemented region(s) and Region B represents uncemented region(s), the 3D criterion applies to large NFs that span throughout the reservoir height and are partially/fully cemented;

- When the cemented regions (Region A) in the model are replaced with intact rock, the derivation of the 3D criterion still holds and applies to small NFs (Region B) that are shorter than the reservoir height;

- When Region A and Region B have the same properties, the whole interface is fully cemented/uncemented ($A_u = A_0, C_u = C_0$) and the 3D criterion (Equations 3.19 and 3.20) will reduce to the previous 2D criterion (Equations 3.12 and 3.13);

- In our experimental cases, the tensile strength and cohesion for Region B are zero ($A_u = C_u = 0$), and the 3D criterion reduces to:

$$\frac{\frac{a}{h}A_0 - \sigma_{xx}^r}{T_0 - \sigma_{yy}^r} > 0.8412 \tag{3.22}$$

$$\frac{\frac{a}{h}\frac{C_0}{\bar{\mu}} - \sigma_{xx}^r}{T_0 - \sigma_{yy}^r} > \frac{0.1467}{\bar{\mu}} + 0.7301, \bar{\mu} \in (0, 1.5] \tag{3.23}$$

A comparison is made between the *3D Slipping Threshold* and the *Extended R-P Criterion* (Gu et al. 2012) in the parametric space where one dimension is the crossing stress ratio ($\frac{-\sigma_{xx}^r}{T_0 - \sigma_{yy}^r}$) and the other is the interface friction coefficient (Figure 3.15). The 3D Opening Threshold is not compared since both the *R-P Criterion* and the *Extended R-P Criterion* do not consider the condition of interface opening induced by an approaching crack. The region above each curve represents the crossing condition and below represents no crossing condition.
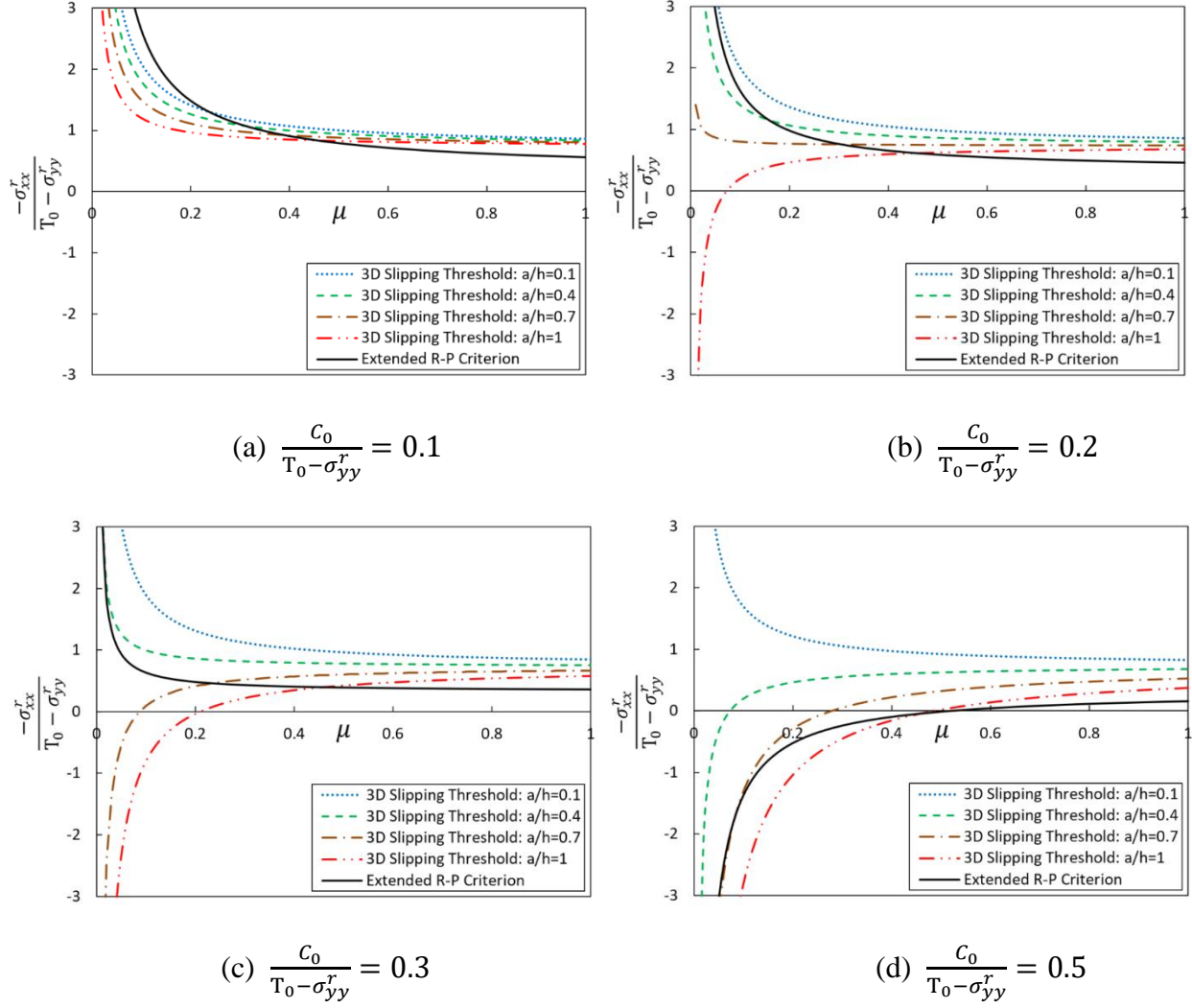
Figure 3.15: Comparison between the 3D Slipping Threshold and *Extended R-P Criterion*.

Note that in order to make the comparison, the criteria are rearranged as follows:

3D Slipping Threshold: $\dfrac{-\sigma_{xx}^r}{T_0-\sigma_{yy}^r} > \dfrac{0.1467}{\bar{\mu}} + 0.7301 - \dfrac{a}{h\cdot\bar{\mu}}\left(\dfrac{C_0}{T_0-\sigma_{yy}^r}\right)$ (3.24)

Extended R-P Criterion: $\dfrac{-\sigma_{xx}^r}{T_0-\sigma_{yy}^r} > \dfrac{0.3302}{\mu} + 0.3302 - \dfrac{1}{\mu}\left(\dfrac{C_0}{T_0-\sigma_{yy}^r}\right)$ (3.25)

For the sake of this comparison, we take $\bar{\mu} = \mu = \mu_c = \mu_u$, which embodies the assumption that the cement filling material and the rock have the same friction coefficient. We

64

also assume $C_u = 0$ so that the cohesion of the cemented regions for the two criteria are both given by C_0. Examining each plot, we observe that, predicted by the *3D Slipping Threshold*, the portion of the parametric space associated with crossing will increase along with the cemented ratio (a/h, the ratio of cemented/total height of the NF). Also, from Figure 3.15a to Figure 3.15d, the criterion shows that as the relative cohesion of the NF ($\frac{C_0}{T_0 - \sigma_{yy}^r}$) increases, the cemented ratio has an increasing influence on the *3D Slipping Threshold*, resulting in divergence from the *Extended R-P Criterion*. Namely, for small-cohesion cases (e.g., $\frac{C_0}{T_0 - \sigma_{yy}^r} = 0.1$), the two criteria have relatively small difference, regardless of the cemented ratio. But, as the interface cohesion increases (e.g., $\frac{C_0}{T_0 - \sigma_{yy}^r} = 0.2$), the curves for the *3D Slipping Threshold* with different cemented ratios become significantly divergent, suggesting that a small change in the cemented ratio is sufficient to greatly impact the crossing behavior.

3.6   COMPARISON WITH EXPERIMENTS AND DISCUSSION

To quantitatively verify the developed 3D Criterion, experimental results from four sets of hydraulic fracturing tests were compared against the 3D Interface Opening Threshold and the 3D Interface Slipping Threshold. The results are plotted in a parametric space where one dimension is the Interface Opening/Slipping Potential and the other is the weighted interface friction coefficient. The HF is predicted to cross the fully/partially cemented interface only when both thresholds are satisfied. In other words, only the points that are above the threshold lines in both Figure 3.16a and Figure 3.16b predict the interface crossing result. When both criteria are satisfied, the prediction of crossing is consistent with nearly all experimental cases. Indeed, only two tests

in Case 1 and two tests Case 4, very close to the threshold, are predicted to cross but observed not to cross. Similarly, all the tests predicted not to cross due to failing one or both criteria are observed as no crossing cases, except for one test in Case 3. A comparison of the derived crossing criterion and experimental results therefore shows clear agreement.

In spite of the positive comparison with experiments, some words of caution are in order. Firstly, it is to be noted that the fluid flow parameters, such as the injection rate, fluid viscosity and NF conductivity could also make a difference in the HF propagation behavior, as illustrated in past experiments (Beugelsdijk et al. 2000; Bunger et al. 2015). These parameters are often accounted for by numerical simulations (Zhang and Jeffrey 2008; Chuprakov et al. 2013; Kresse et al. 2013b). In our case, the fluid pumping rate and viscosity were kept consistent in all the experiments in order to focus on the influence of the NF heterogeneity, and it can be readily shown that this restricts our study to the so-called "viscosity-toughness transition" regime and "toughness-dominated" regime (Savitski and Detournay 2002; Bunger et al. 2004; Detournay 2004). In other words, our experiments are limited to regimes in which fluid flow is expected to be of limited or negligible importance. Secondly, the criterion only applies to orthogonal intersections between HFs and NFs, with isotropic and homogenous rock matrix. An extension to oblique intersection is certainly possible, but we do not carry out the analysis here. Finally, the experiments presented were conducted assuming a symmetric distribution of the cemented/uncemented regions along the NF. In natural reservoirs, the morphology of geological discontinuities can be complex non-symmetric bonded areas and different inclination angles. Future work should therefore be aimed at developing more comprehensive solutions to include these additional factors.
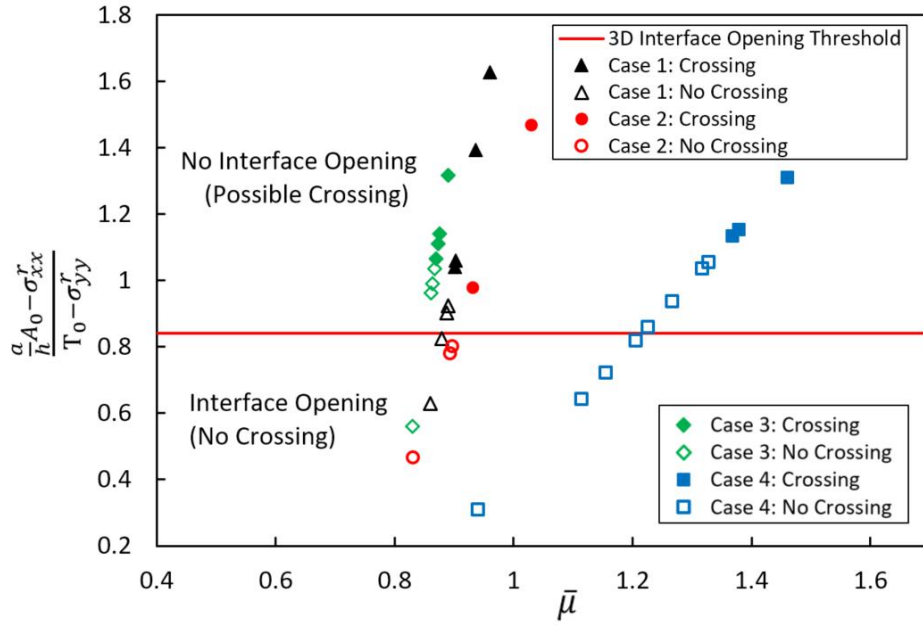
(a)
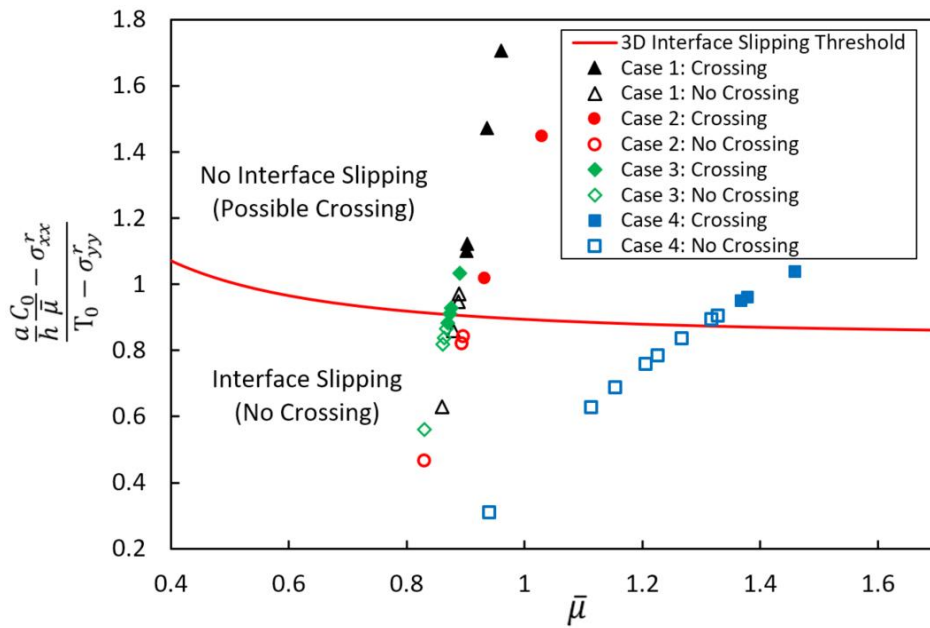
(b)

Figure 3.16: Comparison between test results and analytical criterion, (a) comparison with Interface Opening Threshold; (b) comparison with Interface Slipping Threshold.

3.7   CONCLUSIONS

The existence of NFs is one main issue that can greatly influence the HF propagation in reservoirs and eventually engineering design. Existing criteria with a 2D view may be sufficient in some growth geometries, but the 3D criterion we proposed here overcomes some of the limitations arising from the often-used assumptions that 1) the NF height coinciding with the reservoir/HF height, and 2) uniform properties of the NF, and therefore is able to give more realistic prediction of the fracture network in reservoirs.

Motivated by an objective to derive a new HF crossing criterion for partially cemented and non-persistent NFs, we have firstly presented laboratory experiments in which the HF impinges orthogonally on a partially or fully cemented NF. Apparent dependence of crossing/no crossing behaviors was observed on the heterogeneity of NFs, characterized by the proportion of cemented region(s), cementation strength, and NF height. When the proportion of cemented region decreases, the HF's behavior changes from crossing the whole interface directly, to crossing the interface at cemented region(s) with a mismatched crack path at uncemented region(s), and eventually to diverting completely into the interface (i.e. not crossing). When the strength of the cement filling material increases, a smaller critical cemented height in an otherwise weak NF can completely control the crossing behavior of a HF. When the strength of the host rock is larger, larger cemented region(s) of the interface are needed to promote interface crossing, and small NFs become more prone to hamper the HF propagation.

Guided by these experiments, an analytical criterion based on linear elastic fracture mechanics has been derived to predict the crossing/no crossing behaviors. The criterion evaluates

68

the stress components acting along the interface to promote interface crossing/debonding at the locations where they are maximized, and determines the threshold for the fracture initiation when both the opening and the slipping of NFs are suppressed. The criterion is the first analytical criterion that evaluates the dependence of HF propagation on partial bonding and/or non-persistence of NFs. It is compared with experimental results from four sets of hydraulic fracturing tests and is observed to provide accurate predictions for the 3D HF-NF interaction behaviors. Because of its computational simplicity, the criterion can be readily embedded in HF simulators and help establish more rational estimations of the complex and multi-strand HF propagation in real reservoirs.

4.0   THREE-DIMENSIONAL LATTICE SIMULATION OF HYDRAULIC FRACTURE INTERACTION WITH NATURAL FRACTURES

4.1   PREAMBLE

This chapter comprises a preprint of Fu et al. (Fu et al. 2018b). It presents fully-coupled 3D lattice simulation of the interaction between hydraulic fractures and natural fractures with varying mechanical and geometrical properties. In a large parametric space of natural fracture properties, the simulation results match the 3D analytical criterion well (Fu et al. 2018a) for twenty series of simulation cases with different natural fracture cohesion, tensile strength, friction coefficient, location of cemented regions, cemented proportions, and/or host rock materials. It also reveals that the 3D interaction between hydraulic fractures and natural fractures is an outcome of global interaction mechanism which is influenced by the overall properties of encountered natural fractures, not just a localized hydraulic fracture-natural fracture interaction determined by local interface conditions alone. Consistent with experiments and analytical prediction, the simulation demonstrates that the consideration of spatial variations of natural fracture properties is crucial for more realistic estimation of hydraulic fracture propagation patterns.

4.2   ABSTRACT

Determination of the hydraulic fracture (HF) propagation patterns in fractured unconventional reservoirs typically assumes that natural fractures (NFs) persist through the full height of the reservoir/HF with uniform properties. Here a fully-coupled lattice simulator is employed to simulate the 3D interaction between HFs and NFs with varying mechanical and geometrical properties, thus capturing the dependence of HF propagation patterns on the NF cemented proportions and/or height observed in analogue laboratory experiments, and matching a 3D analytical criterion for simulation cases with different NF cohesion, friction coefficient, tensile strength, location of cemented regions, cemented proportions, and/or host rock materials.

4.3   INTRODUCTION

Hydraulic fracturing, together with horizontal drilling, is the main technology that triggered the increasing production of hydrocarbons trapped in low-permeability unconventional reservoirs. One of the main factors that can greatly influence the hydraulic fracture (HF) propagation is the existence of natural fractures (NFs), which have been widely observed in reservoirs from core samples, mineback experiments, and outcrop studies (Warpinski and Teufel 1987; Hennings et al. 2000; Gale et al. 2007, 2014; Jeffrey et al. 2009a). HFs have been found to cross, cross with offsetting, or be deviated by NFs (Hanson et al. 1981; Blanton 1982; Warpinski and Teufel 1987; Jeffrey et al. 2009b), leading to the potential for complicated propagation trajectories. Field

microseismic mapping during hydraulic fracturing also provides qualitative evidence of strong NF-HF interactions in shales, which caused complex event clouds surrounding the HF paths (Maxwell et al. 2002; Fisher et al. 2004, 2005; Warpinski et al. 2005).

In the midst of such an inhomogeneous subsurface environment, various factors have been found to influence the HF propagation when impinging on NFs. A HF tends to cross a NF under high differential stress and/or intersection angle. On the other hand, a HF can be deviated by a NF in situations with low differential stress and/or intersection angle (Blanton 1982, 1986; Doe and Boyce 1989; Gu and Weng 2010; Gu et al. 2012). The influence of fluid flow parameters, such as injection rate and fluid viscosity, has also been studied through experiments and numerical/analytical modeling (Beugelsdijk et al. 2000; Zhang et al. 2009; Chuprakov et al. 2013; Kresse et al. 2013a; Llanos et al. 2017).

While these studies have provided essential information on the HF-NF interaction mechanisms, most of them focus on NFs that have no cohesion or small cohesion (Blanton 1982, 1986; Teufel and Clark 1984; Warpinski and Teufel 1987; Renshaw and Pollard 1995; Jeffrey et al. 2015; Llanos et al. 2017). Extensive field observations and geologic characterization of unconventional reservoirs, on the other hand, reveal that NFs are commonly sealed with mineral cementation (Laubach 2003; Gale et al. 2007). Shales are typically prone to have sealed fractures because of the diagenetically reactive nature. In the Barnett Shale, calcite sealed NFs appear to be dominant and may serve as weak planes (Gale et al. 2007; Gale and Holder 2008; Lee et al. 2014). Meanwhile, in the highly siliceous Woodford Shale and tight-gas sandstone reservoirs, quartz sealed NFs are more frequently found with strength/stiffness larger than the reservoir rock (Gale et al. 2014; Lander and Laubach 2014; Laubach et al. 2016). The sealed NFs, therefore, possess

72

different mechanical characteristics than uncemented fractures, and may not contribute to reservoir storage or enhance permeability without being activated.

Research on the influence of cemented NFs during HF propagation has increased in recent years. Laboratory hydraulic fracturing experiments and semicircular bend tests demonstrate that cemented fractures may influence HF propagation patterns and the morphology of the induced fracture networks (Zhou et al. 2008; Lee et al. 2014; Wang and Li 2017). Analytically, the Renshaw-Pollard (R-P) criterion has been extended to include the impact of NF cohesion and intersection angles (Renshaw and Pollard 1995; Gu and Weng 2010; Gu et al. 2012). A recently-developed analytical model (OpenT) evaluates NF's local activation and re-initiation and accounts for NF mechanical properties and fluid flow effects (Chuprakov et al. 2013).

In spite of these advances, two simplifying assumptions have been continuously made in almost all the aforementioned approaches: 1) the height of the HF is comparable or less than the height of the pre-existing NF, and 2) the properties of the NF are uniform. However, NF height is found to vary widely in reservoirs (Philipp 2008; Gale et al. 2014). Core samples and outcrops from eighteen shale plays show that NFs have different heights ranging from <1 cm to 1.8 m (Gale et al. 2014). Meanwhile, NFs can be partially sealed instead of fully cemented or uncemented (Laubach 2003; Fidler 2011; Gale et al. 2014). The mechanical and geometrical heterogeneities of NFs may generate HF-NF interaction behaviors that are distinct from the observations made on fully cemented/uncemented NFs.

Indeed, the non-persistence and spatial variability of discontinuities comprise one of the most challenging problems in practical rock engineering and are shown to have significant influences on overall rock mass behavior (Einstein et al. 1983; Kim et al. 2007; Bahaaddini et al. 2009; Shang et al. 2017). In the hydraulic fracturing area, recent research demonstrates that the

73

partially cemented and/or non-persistent NFs can greatly impact the HF propagation patterns (Fu et al. 2015, 2016). As the cemented proportion of the NF decreases, three interaction patterns are observed in laboratory experiments: (1) complete crossing, (2) crossing with mismatched crack path, and (3) no crossing. Perhaps the most striking observation is that a relatively small cemented portion (≤30%) in an otherwise cohesionless NF can be sufficient to promote crossing, with the HF attaining the full height of the host rock after crossing. HFs were also found to be able to engulf hard inclusions during propagation (Olson et al. 2012). These findings show that NFs' realistic spatial variation in mechanical properties and height can have a first-order impact on HF propagation. In response to these observations, Fu et al. (Fu et al. 2018a) developed an analytical criterion to quantify the dependence of crossing/no crossing behaviors on the heterogeneity of NFs, characterized by the proportion of cemented region(s), NF height and cementation strength.

Numerical modeling is another common approach to study the HF propagation in fractured reservoirs. Models that consider NFs can be generally divided into three categories in terms of HF geometry and HF-NF interaction mechanisms. The first category includes 2D models that normally employ a plane strain assumption. For example, a fully coupled 2D model (MineHF2D) based on displacement discontinuity method (DDM) (Crouch and Starfield 1983) to solve the crack nucleation, growth and arrest at NFs has been developed by Zhang and co-authors (Zhang and Jeffrey 2006; Zhang et al. 2007). Extended-finite-element-method (XFEM) has also been adopted in HF-NF interaction simulation, with the advantage of overcoming computationally burdensome remeshing procedures in FEM (Budyn et al. 2004; Dahi-Taleghani and Olson 2011; Dahi Taleghani et al. 2013). In other approaches, 2D models based on hybrid schemes, such as the finite-discrete element method or discrete-continuum method, are also being developed (Fu et al. 2012; Lisjak et al. 2017; Zhang et al. 2017).

A second category of simulators consists of Pseudo-3D models and some fully 3D models that couple with simplified 2D HF-NF interaction criteria (Olson and Dahi Taleghani 2009; Weng et al. 2011, 2014; McClure et al. 2016). For example, the complex-fracture-network model developed by Weng and co-authors (Weng et al. 2011, 2014), normally referred to as unconventional fracture model (UFM), implements 2D analytical criteria to control the fracture interaction (Gu and Weng 2010; Gu et al. 2012; Chuprakov et al. 2013). Wu and Olson (Wu and Olson 2014, 2015) developed a model from fully 3D DDM, with the crossing criterion modified from the extended *R-P criterion* (Renshaw and Pollard 1995; Gu and Weng 2010). These models break the 2D limitations and solve fluid flow and fracture deformation in pseudo-3D or fully 3D approaches, but they can be limited in estimating 3D HF-NF interaction behaviors (Olson et al. 2012; Fu et al. 2015, 2016) because of implementing 2D analytical criteria and/or ignoring the spatial variation of NFs' cemented regions and height.

A third category of simulators includes 3D models that are capable of solving fully-coupled interaction between HFs and NFs with different geometry and/or non-uniform properties (Damjanac et al. 2010, 2016, Nagel et al. 2011, 2013; Damjanac and Cundall 2016; Settgast et al. 2017). Among these models, one promising approach is the synthetic rock mass (SRM) concept (Pierce et al. 2007), which overcomes the limitation of predefined fracture trajectory in models such as traditional DEM simulators (Nagel et al. 2011, 2013) or continuum models (Settgast et al. 2017). The SRM scheme has been implemented in DEM codes PFC2D (Itasca Consulting Group 2008a) and PFC3D (Itasca Consulting Group 2008b), in which brittle rock is presented by bonded particle model (BPM) and discontinuities are presented by the smooth joint model (SJM). The most recent advance of SRM implementation is a lattice scheme code (XSite) developed by Itasca. The lattice model aims to represent all essential physics for 3D hydraulic fracturing simulation. At

the same time, it provides improved computational efficiency compared to previous PFC2D/3D implementations (Cundall 2011; Damjanac and Detournay 2013; Damjanac and Cundall 2016; Damjanac et al. 2016).

In this study, the fully coupled lattice simulator (XSite) is adopted to model 3D interactions between HFs and NFs. The mechanical and geometrical heterogeneities of the NFs are taken into consideration, including the variation of NF cemented regions, NF height and cementation strength. We first conduct numerical simulation based on four sets of experimental data presented by Fu and co-authors (Fu et al. 2016, 2018a). Meanwhile, we add simulations to expand the parametric study of NF properties. At the end, detailed comparisons are made between numerical results and the analytical criterion developed by Fu et al. (Fu et al. 2018a) that accounts for 3D HF-NF interactions.

4.4   LATTICE MODELING METHODOLOGY

The lattice simulator employed in this research is developed based on the implementation of the SRM in the lattice. It is capable of solving fully coupled interactions between HFs and pre-existing joints more efficiently without restricting the fractures' trajectories or interaction conditions (Cundall 2011). In the simulator, the deformation and fracturing of the brittle rock matrix are simulated by the lattice. The pre-existing joints are presented by the SJM. Fluid flow is implemented in the HFs and pre-existing joints and fully coupled with mechanical deformation.

4.4.1   Mechanical Model

The lattice used for representing the rock matrix consists of a number of quasi-randomly distributed lattice nodes (discrete masses) connected by springs (Figure 4.1a). Two lattice tessellation methods are available in the model: default tessellation and Voronoi tessellation. The default lattice tessellation derives the location of nodes from the centroids of a packed assembly of spheres created in PFC3D. For upscaled models, the default lattice may overpredict the contact strain and stress dispersion. These undesired effects can be improved significantly with the Voronoi lattice, which determines the node location by Voronoi tessellation in 3D space for quasi-randomly distributed nodes (Damjanac et al. 2016).

In the model, the motions of the nodes (three translations and three rotations) are solved explicitly. For each node, the following central difference formulae of linear momentum balance and displacement-velocity relation are used to calculate the translational degrees of freedom, that is (Damjanac and Cundall 2016):

$$\dot{u}_i^{(t+\Delta t/2)} = \dot{u}_i^{(t-\Delta t/2)} + \sum F_i^{(t)} \Delta t/m \tag{4.1}$$

$$u_i^{(t+\Delta t)} = u_i^{(t)} + \dot{u}_i^{(t+\Delta t/2)}\Delta t \tag{4.2}$$

where $\dot{u}_i^{(t)}$ and $u_i^{(t)}$ are the velocity and position of component i (i = 1, 3) at time t, $\sum F_i$ is the sum of all force-components acting on the node of mass m, with time step Δt. Similarly, the angular velocities are calculated with the central difference formula of angular momentum balance:

$$\omega_i^{(t+\Delta t/2)} = \omega_i^{(t-\Delta t/2)} + \frac{\sum M_i^{(t)}}{I}\Delta t \tag{4.3}$$

Here ω_i is the angular velocity of component i (i $= 1,3$) at time t, and $\sum M_i$ is the sum of all moment-components i acting on the node of moment of inertia I.

The velocities of the nodes are then used to calculate the relative displacement and spring force change:

$$F^N \leftarrow F^N + \dot{u}^N k^N \Delta t \tag{4.4}$$

$$F_i^S \leftarrow F_i^S + \dot{u}_i^S k^S \Delta t \tag{4.5}$$

where "N" denotes "normal", "S" denotes "shear", k^N and k^S are the spring normal and shear stiffnesses, respectively, and F is the spring force. The spring will break and form a microcrack if the spring force along the same degree of freedom exceeds the spring strength.

The pre-existing joints (planar discontinuities) are simulated using SJM in the model and may be inserted in the lattice at arbitrary locations and orientations. If the two nodes of a given spring are located on the opposite sides of a joint plane, then the spring is designated as a joint spring and obeys the SJM. Joint springs respect the direction of the joint plane rather than the direction of the line connecting the corresponding nodes. Slipping and opening behaviors of an unbonded joint are modeled on the joint plane following the relationships (Cundall 2011):

$$\text{If } F^n - pA < 0, \text{then } F^n = 0, F_i^S = 0; \text{ else, } F_i^S \leftarrow \frac{F_i^S}{|F_i^S|} \min\{(F^n - pA)\tan\phi, |F_i^S|\}. \tag{4.6}$$

Here F^n is the normal force (compression positive), F_i^S is the shear force vector, p is the fluid pressure, A is the apparent area of the joint segment, and ϕ is the friction angle.
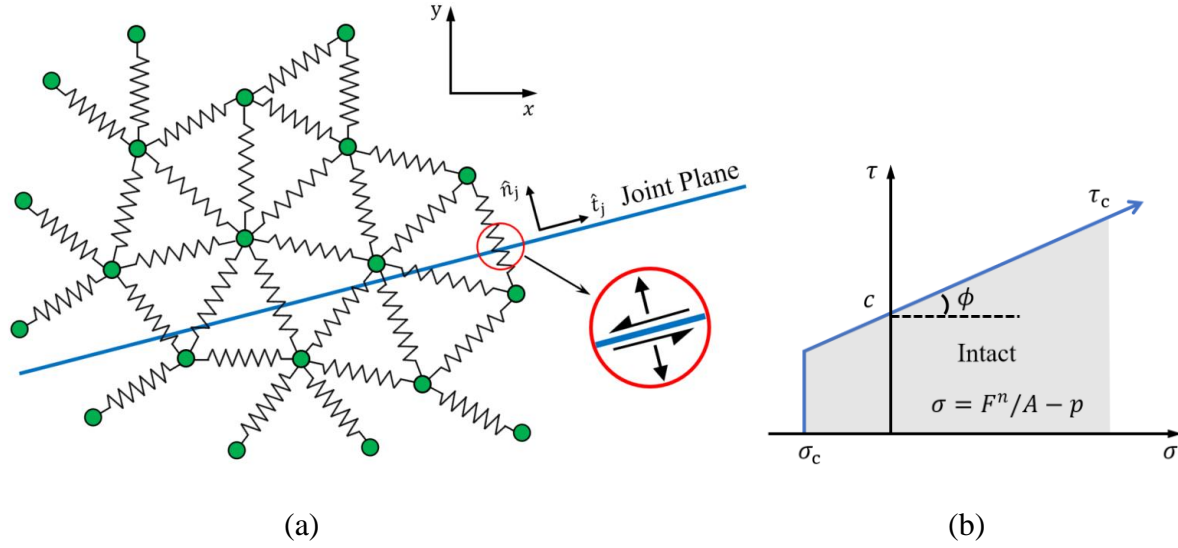
Figure 4.1: Mechanical model: a) schematic of a lattice array in which a discontinuity cuts certain springs. Green circles denote lattice nodes and black zig-zags represent springs. The constitutive equations for the cut springs respect the joint plane orientation $(\hat{t}_j, \hat{n}_j)$ rather than the directions of local springs. The slipping and opening of the joint are modeled on the joint plane. Modified from (Cundall 2011). b) Bond strength envelope, σ_c is the bond tensile strength, τ_c is the bond shear strength, c is the joint cohesion. Modified from (Itasca Consulting Group 2008b).

When the SJM is bonded, the joint bonding status is updated based on the following logic: If $F_n - pA + \sigma_c A < 0$ or $|F_i^s| > \tau_c A$ (bond breaks in tension/shear, Figure 4.1b): joint condition follows Equation 4.6; else, $F_i^s \leftarrow F_i^s$ (bond remains intact).

The overall fracturing of the lattice model includes the breakage of matrix springs as well as the yield of joint springs. The broken springs form microcracks, which may eventually merge into macroscopic fractures.

4.4.2   Flow Model

Transient fluid flow is simulated both within intact rock matrix and the joints. The flow in the rock matrix uses pore pressures stored in the matrix springs to account for the permeability, fluid storage and leak-off. The flow in the joints, including pre-existing joints and newly-created fractures, is modeled with a network of fluid nodes connected by pipes (one-dimensional flow elements) that allow fluid to flow between the fluid nodes. Although the pipes are linear elements, the average hydraulic conductivity of the pipe network matches that of an equivalent planar joint by using pre-computed calibration factors. The fluid nodes are located at the centers of broken springs or springs intersected by the surfaces of pre-existing joints. Fluid pressures are stored in the fluid nodes and flow rates are calculated in flow pipes. As the lattice springs break and form microcracks, the model automatically generates new fluid nodes and connects them with pipes to the existing flow network.

The classical lubrication equation is used to describe the fluid flow within a pipe. The flow rate along the pipe from fluid node "A" to node "B" is calculated as (Damjanac and Cundall 2016):

$$q = \beta k_r \frac{a^3}{12\mu_f} [p^A - p^B + \rho_w g(z^A - z^B)] \tag{4.7}$$

where a is hydraulic aperture, μ_f is viscosity of the fluid, p^A and p^B are fluid pressures at nodes "A" and "B", respectively, z^A and z^B are elevations of nodes "A" and "B" respectively, ρ_w is fluid density, and g is the acceleration due to gravity. Additionally, k_r is the relative permeability, which is a function of saturation ($k_r = 0$ for unsaturated conditions and 1 for fully saturated conditions), and β is a dimensionless calibration parameter, which is a calibrated function of model resolution.

4.4.3 Hydro-Mechanical Coupling

The mechanical and fluid models are fully coupled through simultaneous numerical solution of fluid flow in joints and matrix springs, fracture nucleation and propagation, and deformation of the rock matrix. Specifically, the following hydro-mechanical coupling processes are implemented:

1. The fluid pressure acts as loading on the solid model and joint elements, leading to model deformation and potentially inducing the opening or sliding of fractures.

2. The mechanical deformation of solid model influences the joint aperture and hence the permeability of the rock matrix.

3. The mechanical strain on joint elements causes the change in joint pressure.

4.4.4 Macro-Micro Parameter Relation

Similar to the bonded partial model, the lattice model uses lattice springs characterized by neither engineering nor microscopic material properties. Previously, trial-and-error adjustments of micro-parameters (spring stiffness and strengths) were necessary to recover the required macroscopic properties (e.g. in PFC2D/3D, see (Potyondy and Cundall 2004)). The calibration procedure of the lattice model is conducted in a similar way. The calibration factors that relate the strength and stiffness of springs to the macroscopic strength and elastic moduli of the rock fabric are a function of arrangement of the nodes, which is the same irrespective of the model resolution. Hence, these calibration factors are calibrated and built into the lattice codes directly. The calibration step is therefore avoided, while retaining the characteristic of reproducing macroscopic behaviors from

microscopic mechanisms (Cundall 2011; Damjanac and Detournay 2013; Damjanac and Cundall 2016; Damjanac et al. 2016). Typical macroscopic properties, such as Young's modulus and tensile/shear strength, can be directly specified as it is done for conventional numerical models. For example, Figure 4.2 shows a 10 m × 10 m × 30 m rock specimen. The macroscopic tensile strength of 3.87 MPa is a direct input to the model. Direct tension tests conducted in the lattice simulator render a tensile strength of 3.894 MPa for model with 0.2 m resolution and 3.869 MPa for model with 0.4 m resolution (strength calculated via maximum calibration force/specimen cross-sectional area), both of which are within 1% from the original input value.
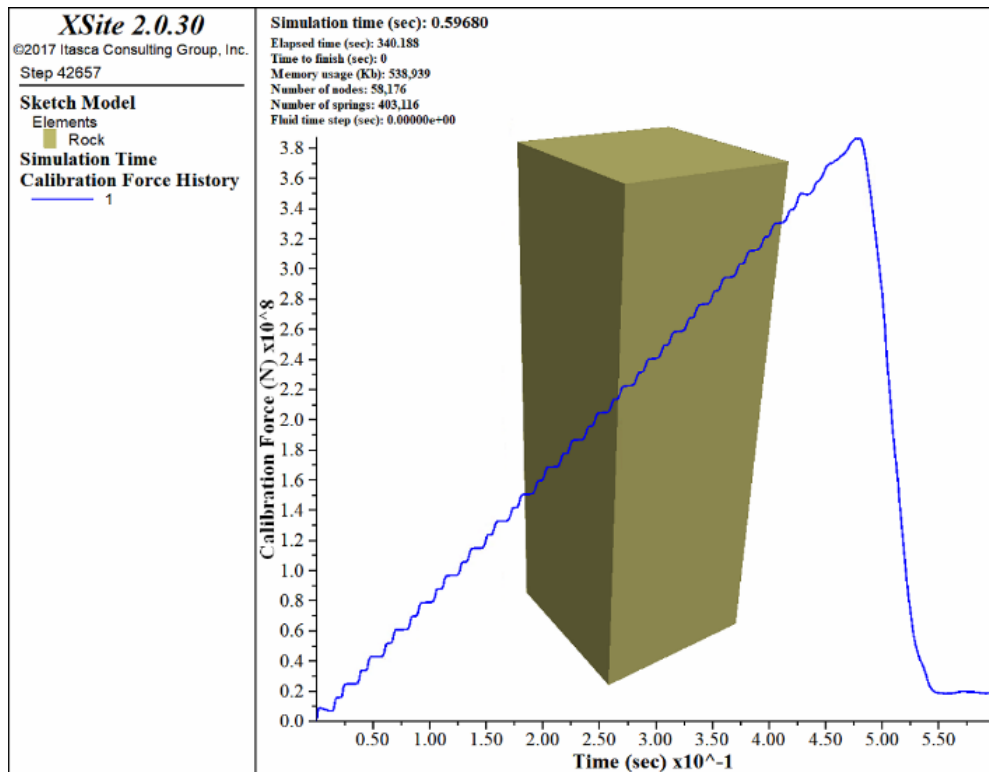
Figure 4.2: Sketch of the cross-sectional view of the experimental setup.

4.5   LATTICE MODEL VERIFICATION

In the experiments carried out by Fu et al. (Fu et al. 2018a), the heterogeneity of NFs is the main interest of research, while the fluid parameters (e.g. pumping rate, viscosities) are chosen so as to have limited influence by restricting the experimental cases to the so-called "toughness-dominated" regime, in which the internal fluid pressure may be considered uniform to first order and fluid lag is neglected (Savitski and Detournay 2002; Bunger et al. 2004; Detournay 2004). Hence, before simulating the hydraulic fracturing experiments, here we first benchmark the lattice model to the large-toughness asymptotic solution for the propagation of a penny-shaped HF in an impermeable elastic rock. The verification test of HF propagation in the viscosity-dominated regime has been presented by (Damjanac and Cundall 2016).

For the HF to propagate in the toughness-dominated regime, the modeling parameters should satisfy that the dimensionless toughness $\kappa \geq 3.5$ (Savitski and Detournay 2002), where

$$\kappa = \mathrm{K}' \left(\frac{t^2}{{\mu_f'}^5 Q_0^3 E'^{13}} \right)^{\frac{1}{18}} \tag{4.8}$$

Here $\mathrm{K}' = 4\sqrt{\frac{2}{\pi}} K_{Ic}$, $\mu_f' = 12\mu_f$, $E' = \frac{E}{1-v^2}$, Q_0 is injection rate, K_{Ic} is material toughness (or critical stress intensity factor), E is Young's modulus, v is Poisson's ratio, and t is pumping time.

In the verification test, the injection rate (0.001 m³/s), fluid viscosity (0.001 Pa · s), lattice resolution (0.2 m), lattice tessellation method (Voronoi tessellation) and mechanical properties of the rock (Type 1 material in Table 4.1) are all set to be the same as those used in the hydraulic fracturing simulation cases of concrete specimens in Chapters 4.6.3 and 4.6.4. The material

toughness is not directly defined in the simulation. Instead, it corresponds to the equivalent toughness of the lattice model, which is controlled by the user-defined rock matrix strength and model resolution. Therefore, displacement-controlled fracture toughness tests are conducted in the simulator to obtain the equivalent toughness. The peak reaction force is recorded at the time of failure for the toughness calculation as (Tada et al. 2000).

$$K_I = \sigma\sqrt{\pi a}F\left(a/b\right) \tag{4.9}$$

$$F\left(a/b\right) = \left\{1 - 0.025\left(a/b\right)^2 + 0.06\left(a/b\right)^4\right\}\sqrt{\sec\frac{\pi a}{2b}} \tag{4.10}$$
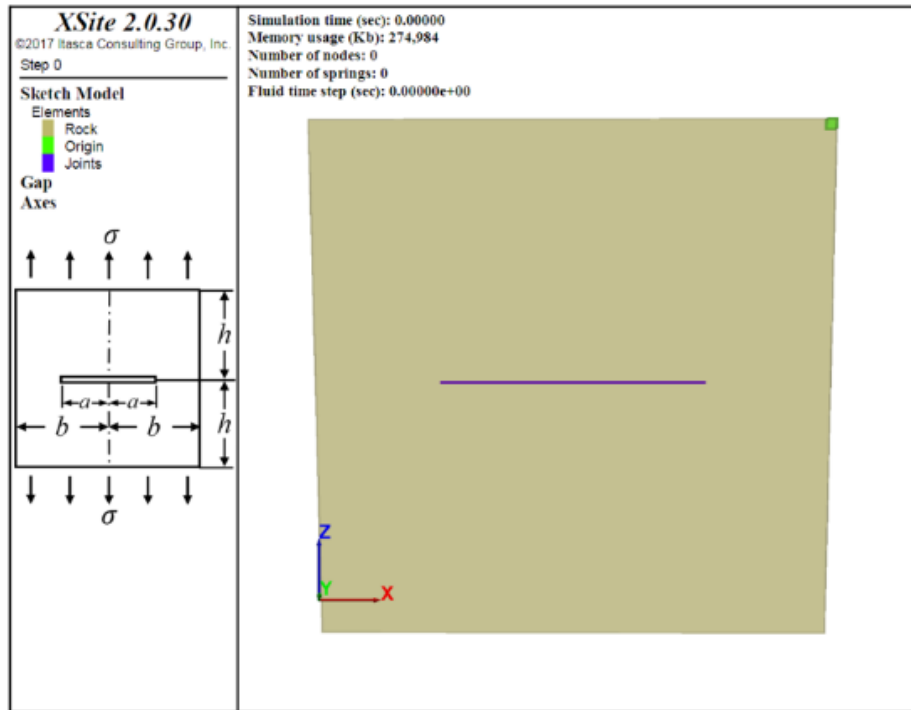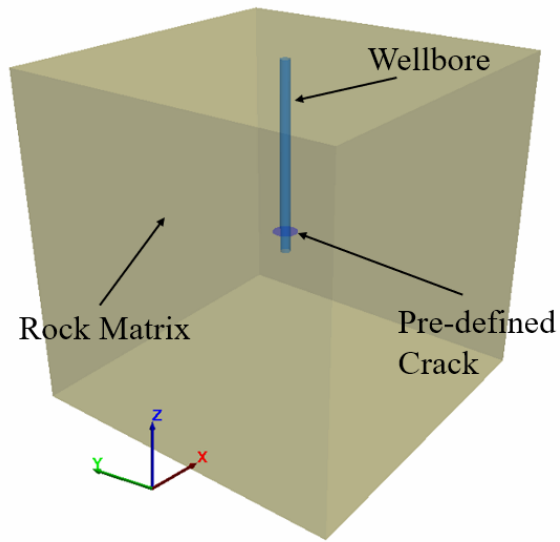

Figure 4.3: Specimen geometry for fracture toughness test.

(a)
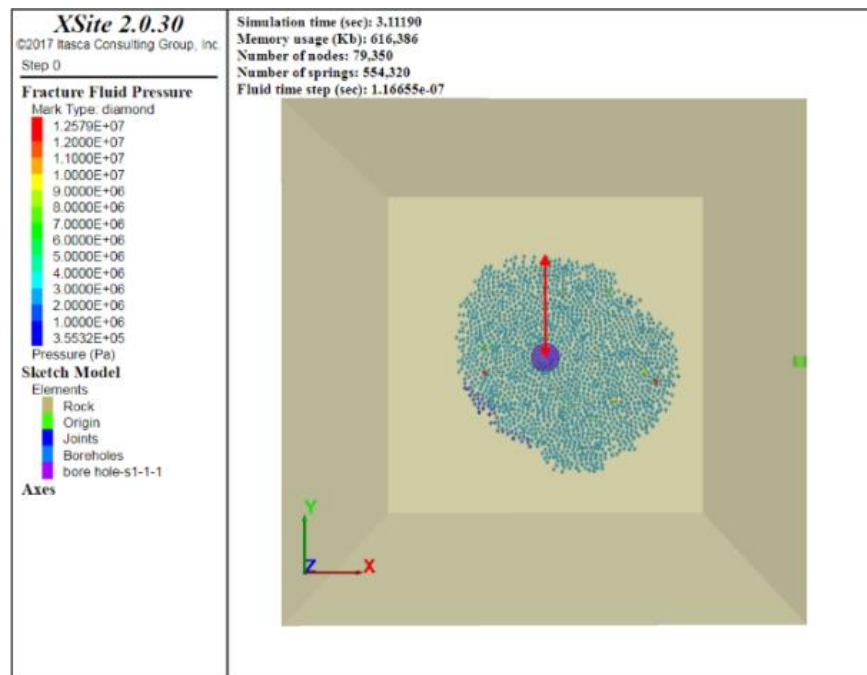
(b)

Figure 4.4: Verification test: (a) specimen geometry; (b) fluid pressure distribution inside the crack after 3s of simulation, top view (x-y plane).

Three tests were conducted on specimens with the same resolution (0.2 m) and different dimensions (60m × 60m × 1m, 70m × 70m × 1m, 100m × 100m × 1m), with an initial uncemented crack (30 m, 40 m, 50 m respectively) located in the center (Figure 4.3). The mechanical properties of specimens and lattice tessellation method are the same as the model of the verification test. The averaged equivalent toughness of three tests is $3.96 \text{ MPa} \cdot \sqrt{m}$. The corresponding dimensionless toughness κ, estimated from Equation 4.8, is 4.11 at pumping time of 1s and 4.64 at 3s.

The model of the verification test under hydraulic fracturing conditions is shown in Figure 4.4, with dimensions of 8 m × 8 m × 8 m. A wellbore is placed vertically into the middle of the specimen. One end of the wellbore passes through the center of a pre-defined weak joint with a radius of 0.3 m and an initial aperture of 10^{-4} m. A small joint lies at the specimen center, perpendicular to the wellbore, and serves as a starter crack to ensure the initiation of the fracture propagation. The horizontal stresses (x and y directions) are chosen to be 1.2 MPa, similar to the magnitude of stresses used in the hydraulic fracturing experiments. The minimum principal stress is set to zero and aligned with the wellbore (z-direction). During simulation, fluid is injected into the wellbore at a constant rate. The HF is anticipated to develop in the x-y plane, starting from the radial, pre-defined joint. The simulation is run for 0.1 second first in the mechanical mode to ensure initial model equilibrium and then 3 seconds in the hydro-mechanical coupling mode.

Figure 4.4b shows the fracture fluid pressure distribution around the wellbore after 3s of fluid injection. Instead of propagating symmetrically about the center of the wellbore, the HF grows into a nearly-elliptical shape, which is similar with the egg-shaped fracture observed by (Bunger et al. 2004) in toughness-dominated hydraulic fracturing lab experiments. Note that Gao and Rice (1987) predict instability of the zeroth order perturbation to a circular crack (crack

remains circular but translates in the plane) when the internal fluid pressure is uniform. The observed instability is slightly stronger, with evidence for slight instability of a first order perturbation (becoming slightly egg-shaped as well as the zeroth order translation).

To quantitatively benchmark the numerical solution, the averaged values (for every 0.1 m of radial distance) of crack opening and net pressure along the path denoted by the red arrow in Figure 4.4b are compared with the leading order and first order asymptotic solutions from (Savitski and Detournay 2002) (Figure 4.5). Note that for the opening profile, aperture of the pre-defined joint (within 0.3 m of radial distance from the wellbore) is not included as it has an initial aperture (10^{-4} m) much larger than the initial aperture of the matrix springs.

It is observed that overall acceptable matches are obtained between the simulations and analytical solutions. The simulation data show more scattered distribution for the opening profile than pressure, and there is a deviation from analytical solutions at the inlet point and crack tip. The deviation may be attributed to different boundary conditions and asymmetric geometry of the crack. At the inlet point, the benchmark solution assumes a point source while the simulation uses a finite-volume cluster with a pre-existing starter crack through it. For the crack tip, the benchmark solution assumes symmetric crack front, while the simulation gives egg-shaped crack geometry. The asymmetric growth may be caused by the uniform internal pressure distribution of the toughness-dominated crack, which promotes the crack growth in random directions influenced by the inherent local heterogeneity of the lattice model, rather than respecting the relative location of the wellbore where maximum pressure takes place in viscosity-dominated cases.
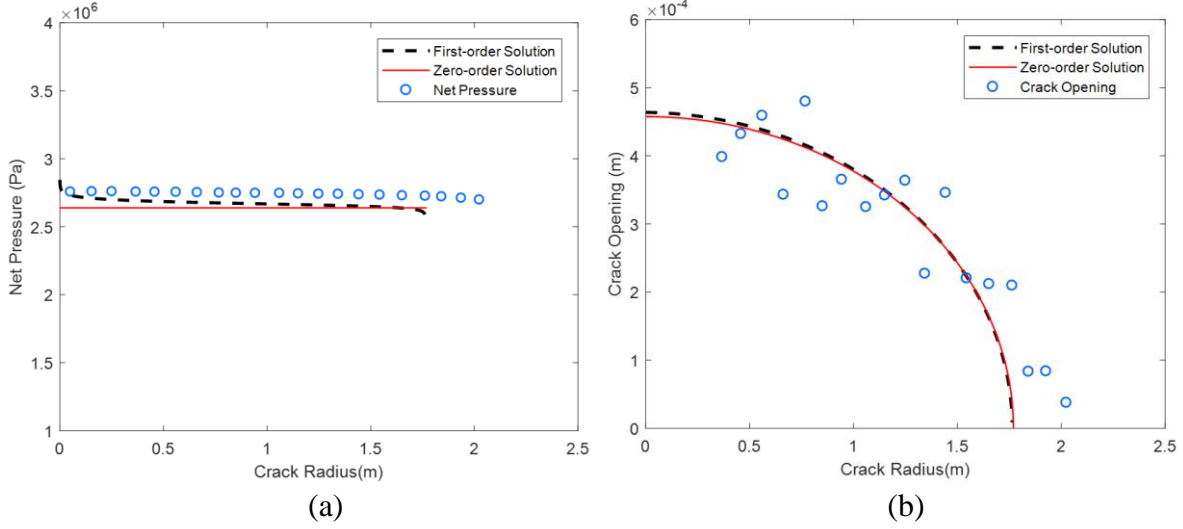
Figure 4.5: Simulation results of the verification test at 3s: (a) net pressure distribution; (b) crack aperture profile.

4.6   LATTICE SIMULATION

In this section, we first briefly introduce, for completeness, the experimental method and analytical criterion for 3D HF-NF interaction presented by Fu et al. (Fu et al. 2018a). Afterwards, we present the fully-coupled 3D lattice simulation of HF-NF interaction based on the experimental cases (Fu et al. 2016, 2018a) but in an expanded parametric space of NF properties. Lastly, we compare the simulation results with the analytical criterion (Fu et al. 2018a).

4.6.1   Experimental Method and 3D Analytical Criterion

Motivated by field observations of NF heterogeneities, Fu et al. (Fu et al. 2016, 2018a) carried out laboratory hydraulic fracturing experiments on concrete/mortar specimens with partially/fully cemented interfaces. The specimens consist of three blocks. The dimensions of each block are 76 mm × 76 mm × 51 mm (3 inches × 3 inches × 2 inches). As illustrated in Figure 4.6a, one of the interfaces is strongly cemented, the other interface, the analogue of a pre-existing NF, is partially or fully cemented by an adhesive with variable strength ranging from weaker to stronger than the matrix material. The thickness of the cemented layer is controlled to be at sub-millimeter scale, which is consistent with the core and outcrop observations that most shale-fracture apertures are in considerably narrow size range of between 30 μm and 1 mm (Gale et al. 2014).

(a)   (b)
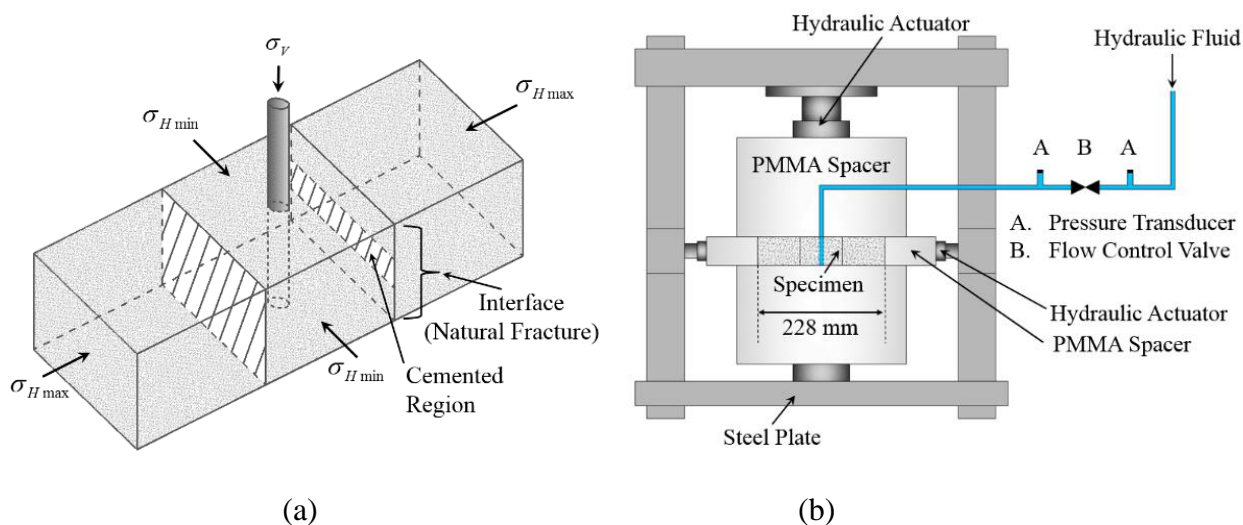
Figure 4.6: (a) Specimen geometry; (b) sketch of the cross-sectional view of the experimental setup (Fu et al. 2016).

For the purpose of creating HFs, a stainless-steel tube with perforation holes at its central region is placed in the central block and acts as the wellbore. Specimens are loaded symmetrically using hydraulic actuators in a true-triaxial loading frame (Figure 4.6b) with vertical stress σ_V, minimum horizontal stress σ_{hmin} (set to zero) and maximum horizontal stress σ_{Hmax}. PMMA spacers are placed around the specimen to promote an evenly distributed compressive stress field. During testing, hydraulic fluid is pumped into the tube at a constant rate throughout the HF growth.

Four sets of hydraulic fracturing experiments were conducted. Within each set of experiments, the height of the cemented region(s) on the interface is varied from full height of the specimen to zero. Four sets of experiments differ from each other in host rock material, location of cemented regions (central region cemented or top-bottom region cemented), and/or NF cementation strength.

Strong dependence of crossing/no crossing behaviors has been observed to be related to the properties of the cemented regions. One of the key findings is that the HF-NF interaction behaviors evolve while the proportion of the cemented region(s) decreases, namely:

a.   Complete crossing, when the NF is fully cemented (Figure 4.7a).

b.   Crossing at cemented region(s) with mismatched crack paths at uncemented region(s), when the NF is partially cemented with a relative large cemented region (Figure 4.7b).

c.   No crossing, when the NF is partially cemented with a relative small cemented region (Figure 4.7c).
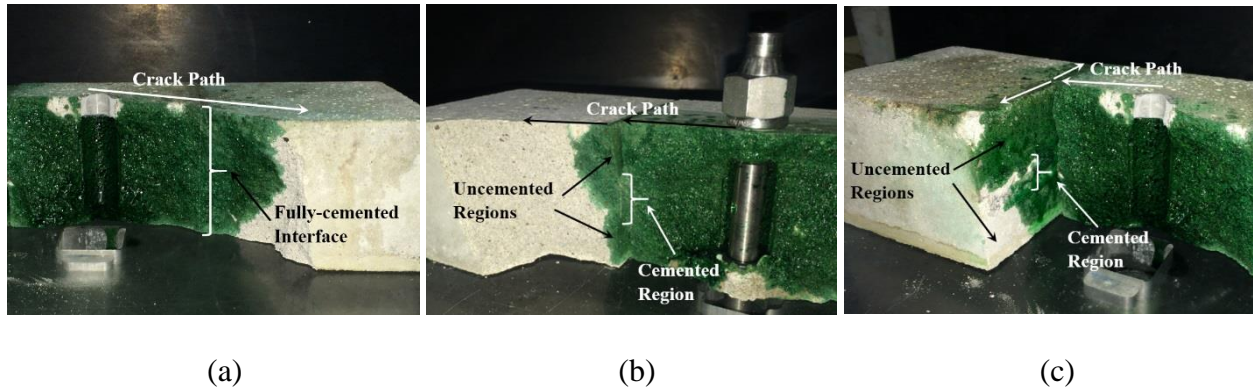
Figure 4.7: Experimental results: (a) complete crossing; (b) crossing at cemented region(s) with mismatched crack paths at uncemented regions; (c) no crossing (Fu et al. 2016).

Note that there are some experimental cases in which the interfaces are partially cemented by adhesives stronger than the host rock material. In these experiments, there is no observable impact of the strong, thin bond on HF propagation relative to the intact rock. In other words, at the strong bond, the direct and undeviated crossing of the interface is observed. Hence, the strongly and thinly cemented regions are behaving analogously to intact rock in the described experiments. Consequently, those partially and strongly cemented interfaces can also be interpreted as uncemented NFs with limited height by treating the cemented regions as the intact rock and the uncemented regions as the NFs, as discussed in (Fu et al. 2016).

Drawing motivation from these experiments, Fu et al. (Fu et al. 2018a) developed an analytical HF-NF interaction model that accounts for the heterogeneities of NF properties, including the variation of cement strengths, cemented region(s), and NF height. The criterion evaluates the stress components acting along the interface to promote interface crossing/debonding at the locations where they are maximized considering the existence of fracture process zone (Figure 4.8). The threshold for the fracture initiation (interface crossing) is determined when both

tension and shear failures along the NF are suppressed. The criterion is compared with four sets of experimental results and found to give acceptable agreement (Figure 4.9). The expressions of the analytical criterion are given as follows:

3D Interface Opening Threshold:

$$\frac{\frac{(h-a)A_u + aA_0}{h} - \sigma_{xx}^r}{T_0 - \sigma_{yy}^r} > 0.8412 \tag{4.11}$$

3D Interface Slipping Threshold:

$$\frac{\frac{(h-a)C_u + aC_0}{h\bar{\mu}} - \sigma_{xx}^r}{T_0 - \sigma_{yy}^r} > \frac{\cos\left(\frac{\theta}{2}\right)\left[1 - \sin\left(\frac{\theta}{2}\right)\sin\left(\frac{3\theta}{2}\right)\right] + \frac{|\sin\left(\frac{\theta}{2}\right)\cos\left(\frac{\theta}{2}\right)\cos\left(\frac{3\theta}{2}\right)|}{\bar{\mu}}}{1.1888}, \theta \in [-36°, 36°] \tag{4.12}$$

An explicit expression for Equation 4.12 can be obtained using least squares curve fitting method (R-square=0.999):

$$\frac{\frac{(h-a)C_u + aC_0}{h\bar{\mu}} - \sigma_{xx}^r}{T_0 - \sigma_{yy}^r} > \frac{0.1467}{\bar{\mu}} + 0.7301, \bar{\mu} \in (0, 1.5] \tag{4.13}$$

Here T_0 is the tensile strength of the rock, σ_{xx}^r and σ_{yy}^r are in-situ stresses, A_0 and C_0 are the tensile strength and cohesion of the cemented interface, respectively. Additionally, A_u and C_u are the tensile strength and cohesion of the uncemented interface, respectively. Also, a is the total height of the cemented region(s), h is the height of the interface/HF, $\bar{\mu} = \frac{(h-a)\mu_u + a\mu_c}{h}$ is the weighted friction coefficient over the entire NF, and μ_c and μ_u are the friction coefficients of the cemented and uncemented region(s), respectively. The HF is thus predicted to cross the NF as long as both Equations 4.11 and 4.12 are satisfied.

(a)   (b)
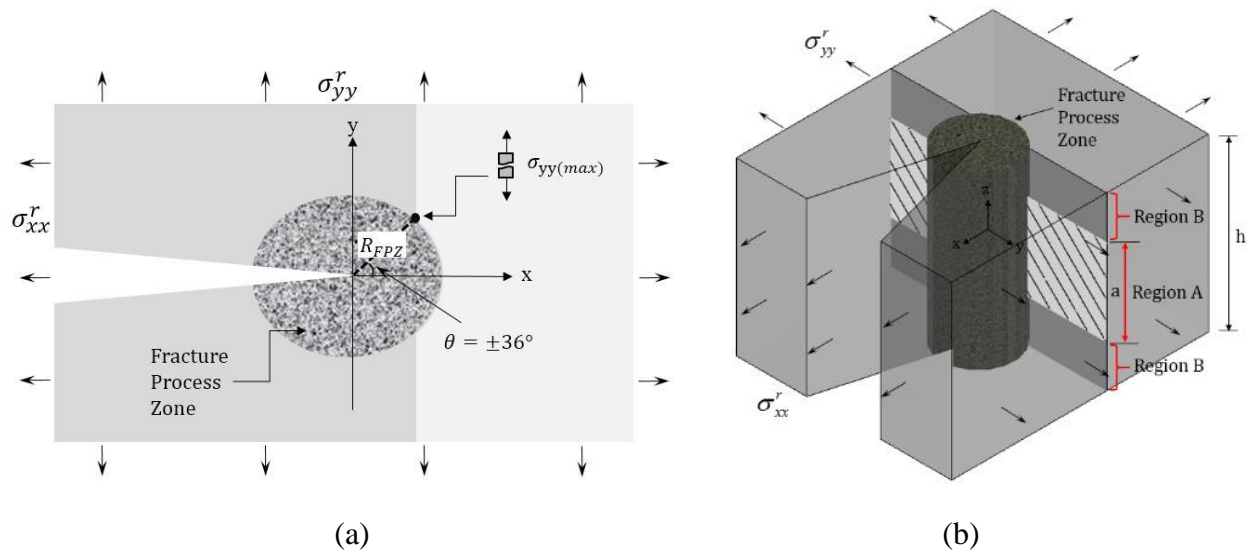
Figure 4.8: A crack propagating orthogonally towards a partially-cemented interface: (a) 2D view;

(b) 3D view, Region A is cemented, Region B is uncemented (Fu et al. 2018a).

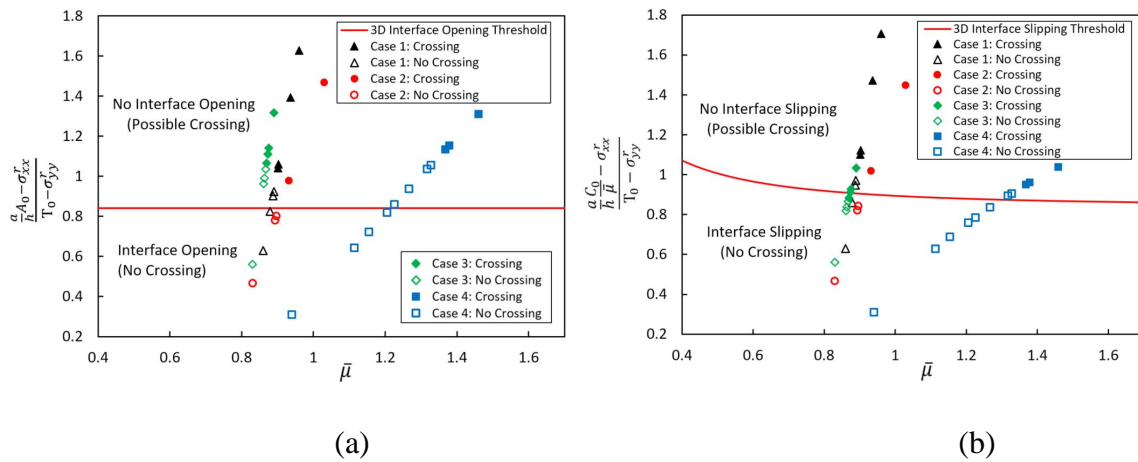(a)   (b)

Figure 4.9: Comparison between experimental results and analytical criterion: (a) comparison

with Interface Opening Threshold; (b) comparison with Interface Slipping Threshold (Fu et al.

2018a).

4.6.2 Lattice Simulation Model Set-up

The geometry of the lattice model is constructed based on the experimental specimens, as illustrated in Figure 4.6a. In the simulation, the mechanical properties of the host rock and the pre-existing interface (NF) are all set to be the same as the experimental cases (Table 4.1). As for fluid parameters, when using the values from the experiments directly (injection rate: 3.5e-8 m^3/s, viscosity: 0.3 Pa·s), the numerical simulation for a single case can take days of computing time due to the small simulation time step decided by the injection rate. Hence, we seek to promote the similarity between the numerical simulation and lab experiments in terms of HF propagation regime, rather than directly employing all the experimental parameters. This is realized by achieving a similar dimensionless toughness (e.g. Equation 4.8) which includes the influence of fluid viscosity, pumping rate and material toughness.

To speed up the numerical simulation, a higher pumping rate is necessary. An examination of Equation 4.8 shows that the dimensionless toughness is positively correlated to the material toughness while negatively correlated to fluid viscosity and pumping rate. Hence, to employ a relatively high pumping rate, a lower viscosity and/or larger fracture toughness is needed in order to maintain the same propagation regime. In the lattice model, fluid pumping rate and viscosity can be directly specified. The fracture toughness is proportional to the square root of model resolution (Potyondy and Cundall 2004). Therefore, it can be increased by scaling up the model dimensions together with the resolution for lattice discretization. The HF propagation is within the same toughness-dominated regime as the lab experiments under the new combination of the pumping rate (0.001 m^3/s), fluid viscosity (0.001 Pa·s) and model resolution (0.2 m).

Figure 4.10: Dimensions of the lattice model.
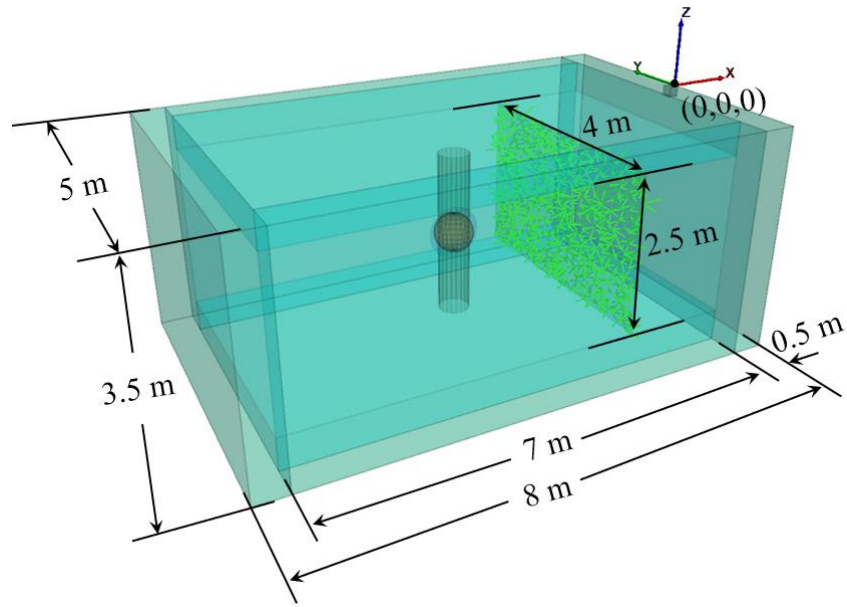

<table>
<tr><td align="center">(a)</td><td align="center">(b)</td></tr>
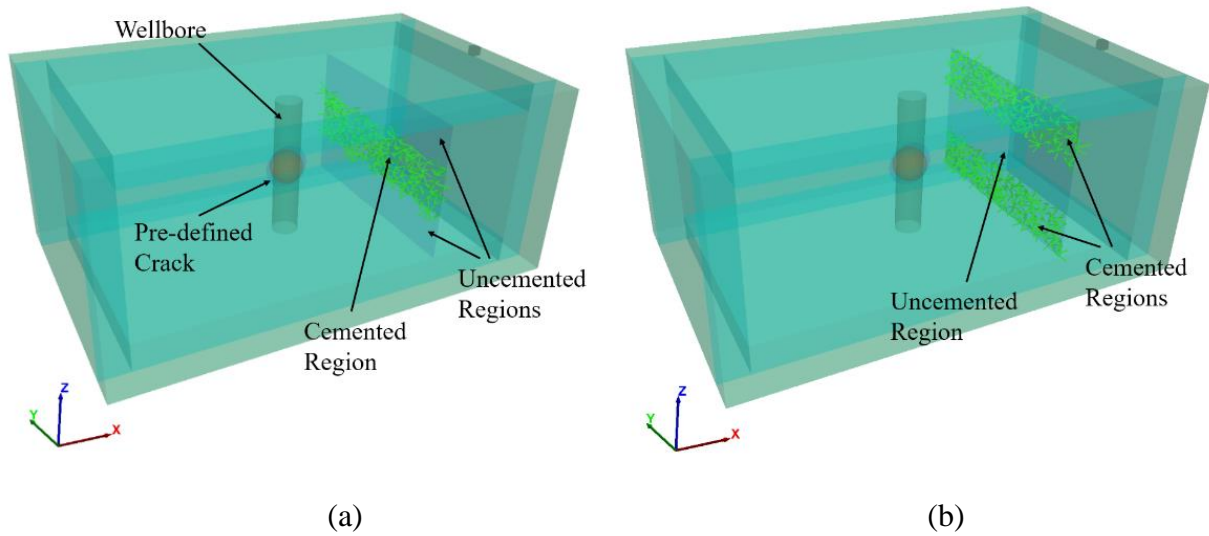</table>

Figure 4.11: Lattice models with partially cemented interface: (a) central region cemented; (b) top-bottom region cemented. Dimensions are the same as the model with fully cemented interface (Figure 4.10).

Table 4.1: Mechanical properties of host rock materials.

Mechanical Property	Unit	Type 1 (Concrete)	Type 2 (Mortar)	Type 3 (Mortar)
Young's Modulus	GPa	25.3	14.7	12.1
Poisson's Ratio	-	0.16	0.17	0.16
Unconfined Compressive Strength	MPa	41.7	16.8	12.8
Tensile Strength	MPa	3.87	2.14	1.75
Cohesion	MPa	4.11	2.16	1.81
Internal Friction Coefficient	-	1.46	1.03	0.96
Interface Friction Coefficient	-	0.94	0.83	0.86

The dimensions of lattice model are 7 m × 4 m × 2.5 m (L × W × H), which are around 50 times greater than the lab specimen dimensions in height and width while relatively short (~30 times) in length to save computing time. A wellbore is placed vertically in the center of the model. A weak starter crack locates at the middle of the wellbore in x-z plane with a 0.3 m radius and 10^{-4} m initial aperture. The interface, which is the analogue of the NF, is 1.9 m away from the wellbore and parallel to the minimum in-situ stress direction (in *y-z* plane). Depending on the location of the cemented regions, the interface can be fully cemented, central region cemented or top-bottom region cemented (Figure 4.10 and Figure 4.11). The cemented region(s) of the interface remains impermeable until the bond fails, the uncemented region(s) is initially permeable and allows fluid inflow. Both regions have a small initial aperture (submillimeter scale, 10^{-4} m) that is taken on a similar order with experimental cases and field observations (Gale et al. 2007, 2014, Fu et al. 2016, 2018a). The wellbore-interface distance relative to the half specimen height is 1.5,

96

which is the same as in the lab experiments. Note that in the experiments, one side of the specimen (left side, Figure 4.6a) was fully and strongly cemented. This strongly and thinly cemented interface has no observable impact on the HF propagation relative to intact rock. Therefore, the fully cemented interface (left side) is replaced by intact rock in the modeling for the simplicity of simulation.

The far field boundaries of the model are one-translation fixed (roller boundary), which is chosen for consistency with experimental constraints. The directions and magnitudes of the in-situ stresses are chosen to be the same as the experimental cases (~1 MPa). The low confining pressure also helps to reduce the influence of potentially significant stress dispersion in the lattice simulation (Damjanac et al. 2016). The lab experiments were conducted under constant-stress boundary condition. This constant-stress condition is approximated in the simulation by adding 0.5 m-thick soft layers along the boundaries of the rock specimen. By setting the Young's modulus of the soft layers to be ~100 times smaller than the rock specimen, the initial in-situ stresses normal to the boundaries change insignificantly. As a result, the soft layers effectively serve as a means to approximate a constant-stress boundary condition.

As with the benchmarking cases, the simulation is first run in the mechanical mode for 0.1 s for initial model equilibrium, after which fluid is injected into the cluster of the wellbore at a constant rate and simulation is continued in the hydro-mechanical coupling mode. A HF is expected to initiate from the starter crack and propagate perpendicularly towards the pre-existing interface.

Note that the simulation is limited to Newtonian fluid and impermeable rock (no fluid leak-off or poroelastic stress changes in the matrix domain). Also, it is assumed that there is no lag between the fluid and fracture front. This is probably consistent, at least to some degree, with the

97

experimental conditions (Fu et al. 2015, 2016, 2018a) and field scale HFs which are typically characterized by vanishing fluid lag compared to the length of the HF (Economides and Nolte 2000; Lecampion and Detournay 2007). Also, as we know, many factors, such as the hydraulic fluid properties, in-situ stresses or poroelastic behaviors of rock matrix may impact the HF-NF interaction process. The goal of our research is to focus on the influence of NF heterogeneities, other parameters are treated as controlled variables and kept constant.

These simulations include 3D interaction cases between HFs and NFs with different locations of cemented regions, cementation proportions and strength. Three types of host rocks from the experiments are employed in the simulation. Besides simulating four experimental cases, we expand the parametric study of NF properties by adding sixteen more numerical cases. We will first present the simulation results of cases with fully cemented interfaces in Chapter 4.6.3, which is the special case corresponding to the 2D condition that has been widely assumed in many previous studies. Afterwards, we will provide simulation results for cases with partially cemented interfaces in Chapter 4.6.4, followed by a discussion in Chapter 4.7.

4.6.3   Simulation Results for Fully Cemented Cases

Simulation conditions for fully-cemented cases are summarized in Table 4.2 and Table 4.3. Within each test set, the mechanical properties of the NF are increased progressively while the other parameters are prescribed. In addition to the NF shear strength, the NF tensile strength can also impact the HF-NF interaction (Fu et al. 2018a). To isolate the influence of strength parameters, the NF tensile strength for cases in Table 4.2 is given a large value (e.g. greater than the matrix tensile strength) such that the interface does not fail due to tension.

Similarly, for cases summarized in Table 4.3, the NF tensile strength is varied while the NF cohesion is set to be big enough to avoid shear failure.

As the NF shear strength or tensile strength increase, the HF-NF interaction behaviors are observed to evolve from no-crossing to crossing in all test sets. Figure 4.12 illustrates a representative crossing case for models with fully cemented interface (Test Set A4, interface cohesion 2.6 MPa). The green elements along the interface represent the impermeable cementation material. Fluid flows into the cemented region(s) only after the cementation material fails. Figure 4.12a shows the fluid pressure distribution in the model, which indicates the propagation path of the HF across the interface. The crossing behavior is further demonstrated in Figure 4.12c, in which the HF aperture profile and fluid pressure distribution both show that the HF propagates approximately 0.6 m farther after crossing the interface located at $x = -2.1$ m. Figure 4.12d shows the crack aperture and fluid pressure along the vertical center of the cemented region ($z = -1.75$ m). Besides the portions close to intersection line ($y = 0$ m), the rest of the interface all remains closed with zero internal fluid pressure, demonstrating that the HF crosses the NF directly with very minor signs of interface debonding close to the crossing location. Figure 4.12b depicts the crack aperture distribution of the whole interface. We observe that all the bigger apertures locate at the central region ($y = 0$ m), which confirms the location where crossing takes place. The nearly-uniform internal fluid pressure (e.g. Figure 4.12c) indicates toughness-dominated HF propagation, which is consistent with the experimental conditions and simulation assumptions.

Table 4.2: Simulation conditions for fully-cemented cases (with pre-defined NF tensile strength), noting that no-crossing results are before the separator mark (|) and crossing result are after the mark.

Test Set	Rock Type	σ_V (MPa)	σ_{Hmax} (MPa)	Rock Tensile strength (MPa)	NF Friction	NF Cohesion (MPa)
A1	1	1.4	1.2	3.87	0.20	0, 0.5, 1.0	1.5, 2.5
A2	1	1.4	1.2	3.87	0.40	0, 0.7, 1.3	1.8, 3
A3	1	1.4	1.2	3.87	0.60	0,1,1.5	2, 3
A4	1	1.4	1.2	3.87	0.84	0, 1, 2	2.6, 3.5
A5	1	1.4	1.2	3.87	1.00	0, 1, 2	3, 4
A6	1	1.4	1.2	3.87	1.20	0, 1, 2	3, 4.1
A7	1	1.4	1.2	3.87	1.46	0, 1.5, 2.5	3.5, 4.1

Table 4.3: Simulation conditions for fully-cemented cases (with pre-defined NF cohesion), noting that no-crossing results are before the separator mark (|) and crossing result are after the mark.

Test Set	Rock Type	σ_V (MPa)	σ_{Hmax} (MPa)	Rock Tensile strength (MPa)	NF Friction	NF Tensile strength (MPa)
B1	1	1.4	1.2	3.87	0.60	0, 1.5	2.5, 3.5
B2	2	1.4	1.2	2.14	1.03	0, 0.5	1, 2
B7	1	1.4	1.2	3.87	1.46	0, 1.5	2.5, 3.5
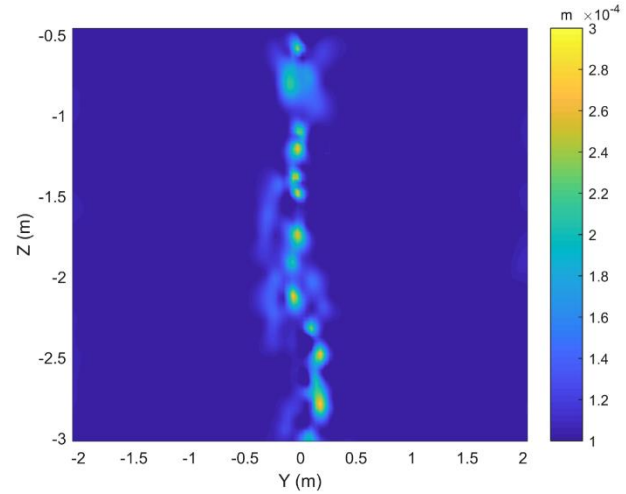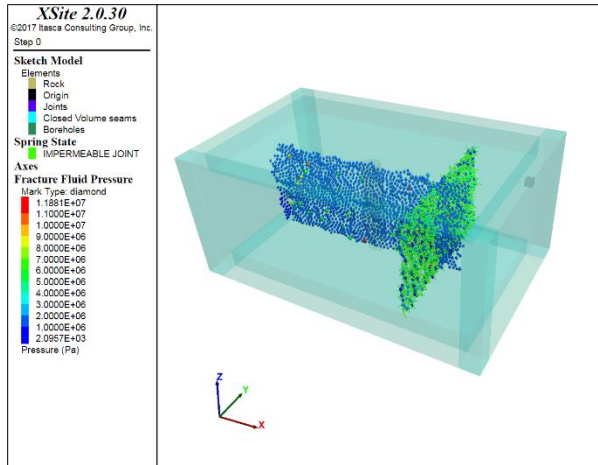
(a)   (b)
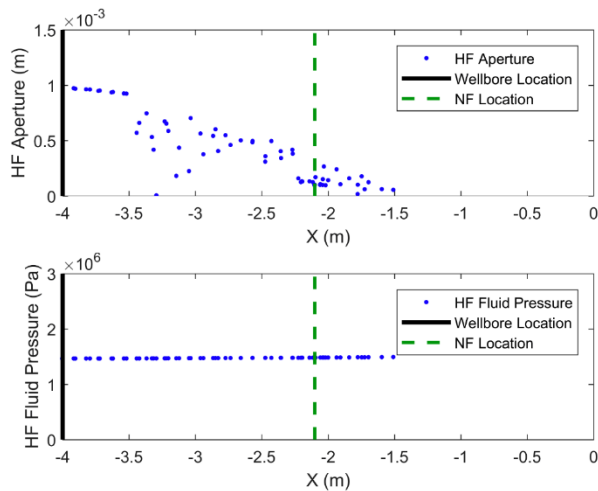
(c)   (d)

Figure 4.12: Crossing case for model with fully cemented interface: Test Set A4, cohesion = 2.6 MPa. a) Fluid pressure distribution; b) crack aperture distribution along the NF, side view (y-z plane); c) crack aperture and fluid pressure of the HF (along the vertical center of model, z = -1.75 m); d) crack aperture and fluid pressure of the NF (along the vertical center of NF, z = -1.75 m).

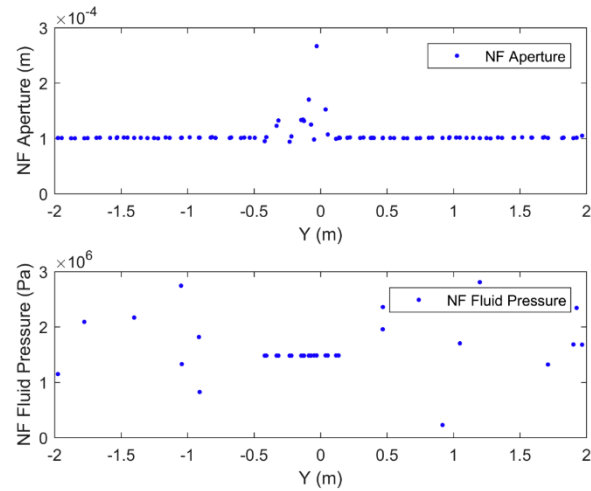(a)   (b)

(c)   (d)

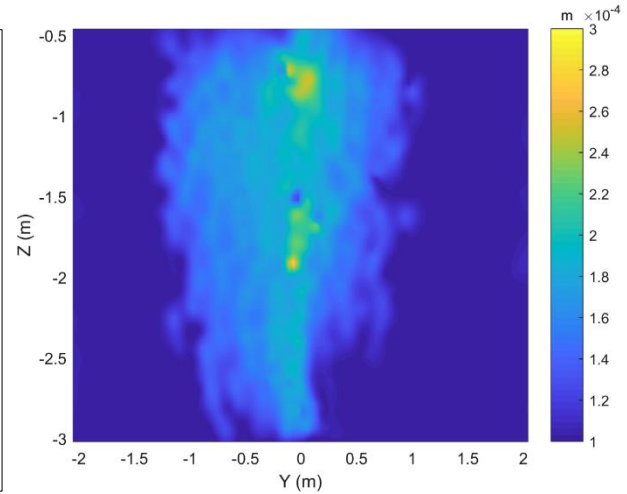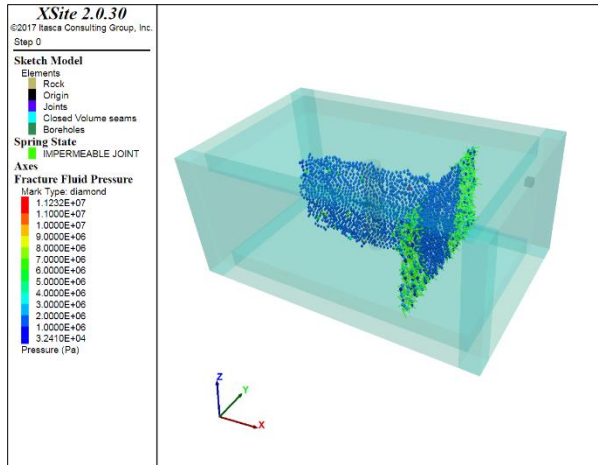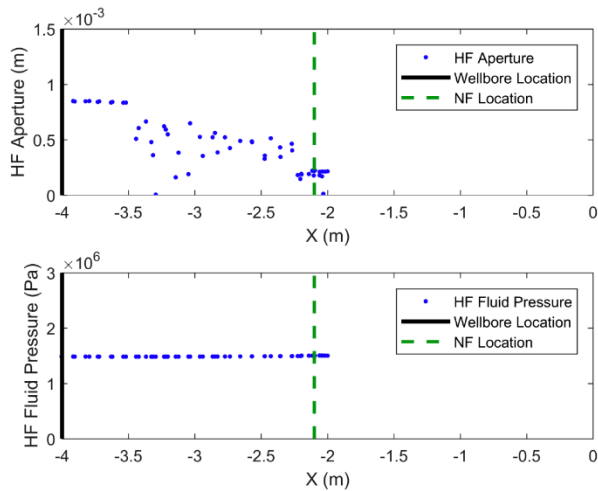**Figure 4.13:** No-crossing case for model with fully cemented interface: Test Set A4, cohesion = 2 MPa. a) Fluid pressure distribution; b) crack aperture distribution along the NF, side view (y-z plane); c) crack aperture and fluid pressure of the HF (along the vertical center of model, z = -1.75 m); d) crack aperture and fluid pressure of the NF (along the vertical center of NF, z = -1.75 m).
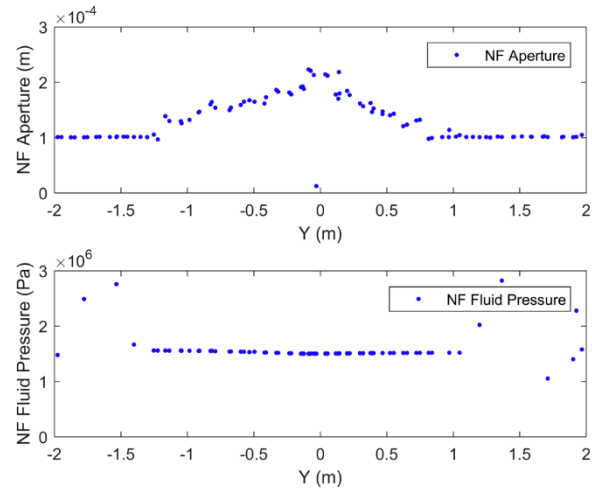
Figure 4.13 shows a typical no-crossing case for models with fully cemented interface. This case is selected from the same test set as the previous crossing case but with smaller NF cohesion (Test Set A4, interface cohesion 2 MPa). We observe that the HF grows perpendicularly to the NF and then get arrested, as illustrated by the fluid pressure distribution in Figure 4.13a. The aperture profile and fluid pressure distribution in Figure 4.13c and Figure 4.13d also indicate that the HF stops after touching the interface ($x = -2.1$ m) and deviates into the interface, leading to the large regions of interface debonding evidenced by increased aperture width and wide distribution of fluid pressure on the interface (Figure 4.13d, from $y \approx -1.2$ m to $y \approx 1$ m). An overall observation of the interface aperture distribution from Figure 4.13b also reveals that almost half of the NF is debonded.

Note that according to the criterion, a HF will cross a NF only when the Interface Slipping Threshold and the Interface Opening Threshold are both satisfied. While in our case, the simulation results are only compared to one corresponding threshold, the other one is automatically satisfied by setting desired strength parameters in the simulation. Figure 4.14 presents the numerical results in a semi logarithmic coordinate system where one dimension is a dimensionless stress ratio, termed as Interface Slipping Potential (Fu et al. 2018a), and the other is the friction coefficient of the cemented interface. Overall, the numerical results are found to match the Interface Slipping Threshold very well. Within each set, the interaction behavior evolves from crossing to no crossing as expected; as the friction coefficient of the interface increases, the crossing/no crossing results demonstrate a much less dependence on friction coefficient as predicted by the Interface Slipping Threshold, compared to the prediction from extended *R-P criterion*. For example, as the friction coefficient increases from 0.5 to 1.5, the Interface Slipping Threshold as well as the simulation

results see a ~15% decrease in the critical dimensionless stress ratio for crossing, in contrast to a 45% decrease predicted by the extended *R-P criterion*.

Similarly, the simulation results for cases with different NF tensile strength are compared to the Interface Opening Threshold, as illustrated in Figure 4.15. The numerical results, as predicted by the analytical criterion, show the substantial impact of the NF tensile strength on crossing/no crossing behaviors. Note that the friction coefficient does not appear in the Interface Opening Threshold, it is employed in the comparison only to indicate different experimental cases.
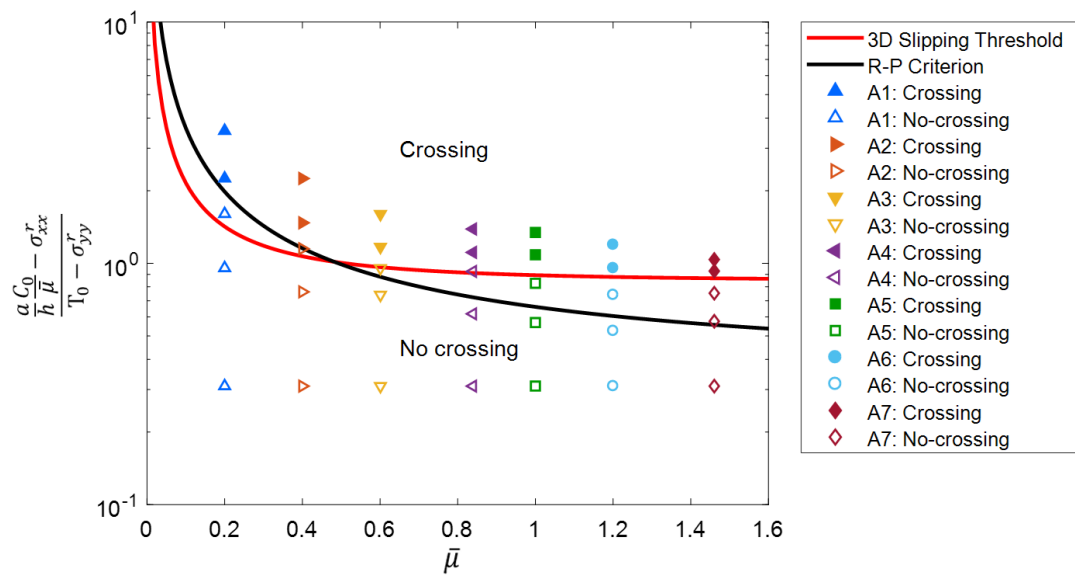
Figure 4.14: Comparison between simulation results of fully-cemented cases and Interface Slipping Threshold.
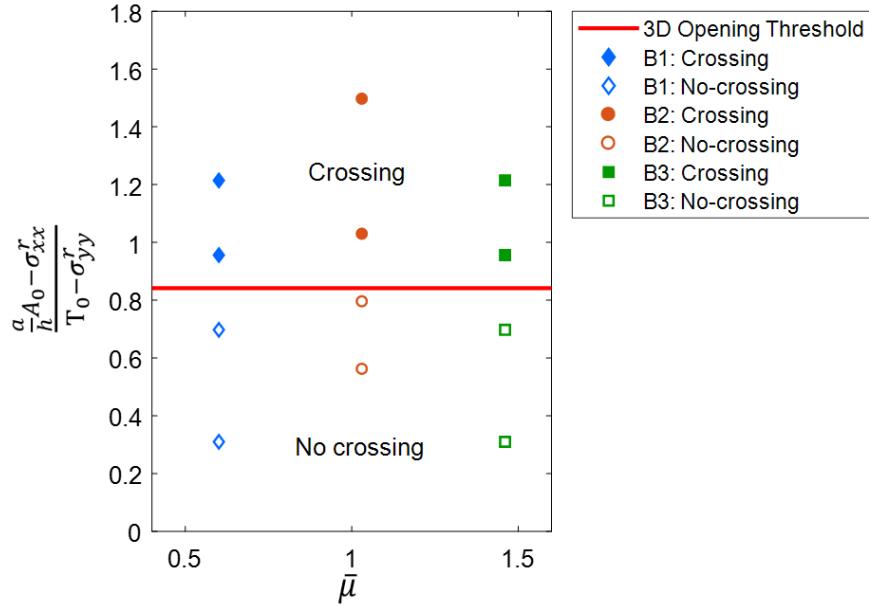
Figure 4.15: Comparison between simulation results of fully-cemented cases and Interface Opening Threshold.

4.6.4 Simulation Results for Partially Cemented Cases

Simulation conditions for the partially-cemented cases are summarized in Table 4.4 and Table 4.5. The test sets of C3, C5, C6, C7 correspond to the experimental conditions of Case 3, Case 1, Case 2 and Case 4 (Figure 4.9), respectively. Six more sets of simulations are added to further expand the parametric space of NF properties. Similar to the fully cemented cases, simulations in Table 4.4 employ large interface tensile strength to avoid the tension failure of the NF. Also, simulations in Table 4.5 use large interface cohesion to ensure the NF does not fail due to slipping, in order to isolate the effects of different strength parameters. Within each test set, the proportion of the cemented region(s) is varied gradually until the NF is fully cemented, the other modeling

parameters are kept constant. Note that in Test Sets C5, C6 and C7, the mechanical properties of the NF are the same as the corresponding host rock. Therefore, the partially cemented cases in these sets can also be interpreted as uncemented NFs with fracture height shorter than the reservoir/HF height, by treating the cemented regions as the intact rock and the uncemented regions as the weak NF, as discussed in Chapter 4.6.1.

Note that only no-crossing results are found in Test Set C3, which indicates that the cementation material is relatively weak and, under the described numerical settings, it is unable to promote interface crossing even if the NF is fully cemented. In spite of Test Set C3, all the other simulations demonstrate a strong impact of cemented regions/NF height on the HF-NF interaction as captured in the lab experiments (Fu et al. 2015, 2016), although the test sets differ from each other in location of cemented region(s), NF tensile/shear strength, and/or host rock materials. Specifically, as the cemented proportions increase, the transition from no-crossing to crossing is commonly observed in nine test sets.

Table 4.4: Simulation conditions for partially-cemented cases (with pre-defined NF tensile strength), noting that no-crossing results are before the separator mark (│) and crossing result are after the mark.

Test Set	Rock Type	Rock Tensile strength (MPa)	σ_V (MPa)	σ_{Hmax} (MPa)	Location of Cemented Region(s)	NF Friction	NF Cohesion (MPa)	NF Cohesion (MPa)
C1	2	2.14	1.4	1.2	Center	0.40	1	0, 20%, 40% │ 60%, 80%, 100%
C2	1	3.87	1.4	1.2	Top/Bottom	0.60	2.5	0, 40%, 48% 60% │ 80%, 100%
C3	2	2.14	1.4	1.2	Center	0.89	0.9	60%, 76%, 100% │
C4	2	2.14	1.4	1.2	Center	0.89	1.5	0, 20%, 40% │ 60%, 76%, 100%
C5	3	1.75	1.3	1.1	Center	0.96	1.81	0, 8% │ 20%, 40%, 100%
C6	2	2.14	1.2	1	Top/Bottom	1.03	2.16	0, 20%, 32% │ 40%, 60%, 72%, 100%
C7	1	3.87	1.4	1.2	Center	1.46	4.11	0, 20%, 48% │ 72%, 100%

Table 4.5: Simulation conditions for partially-cemented cases (with pre-defined NF cohesion), noting that no-crossing results are before the separator mark (│) and crossing result are after the mark.

Test Set	Rock Type	Rock Tensile strength (MPa)	σ_V (MPa)	σ_{Hmax} (MPa)	Location of Cemented Region(s)	NF Friction	NF Cohesion (MPa)	NF Cohesion (MPa)
D1	1	3.87	1.4	1.2	Top/Bottom	0.60	2.5	0, 40%, 60%, 80% │ 100%
D2	2	2.14	1.4	1.2	Center	1.03	1.5	0, 40% │ 60%, 80%, 100%
D3	1	3.87	1.4	1.2	Center	1.46	3	0, 40%, 60% │ 80%, 100%

Figure 4.16 and Figure 4.17 illustrate representative crossing cases for models with top-bottom region cemented interface (Test Set C2, 80% cemented) and central region cemented interface (Test Set C4, 60% cemented), respectively. An overall examination of the fluid pressure distribution indicates that the HF is able to cross the partially cemented NF in both cases (Figure 4.16a and Figure 4.17a). More specifically, the HF aperture profile, as well as the fluid pressure distribution, shows that the HF continues to grow over 1 m after crossing the interface within the simulation time (Figure 4.16c and Figure 4.17c). On the other hand, very limited regions of the interface are debonded and opened. In Case C2-80% (Figure 4.16d), the NF aperture along the vertical center of the cemented region remains 10^{-4} m, which is the initial aperture width, and the fluid pressure is only found near the intersection location ($y \approx 0$ m). For Case C4-60% (Figure 4.17d), the NF is slightly activated near the intersection line, evidenced by the fluid pressure distribution within y= [-0.3 m, 0.5 m]. However, the aperture width within this range is scattered and remains relatively small. The limited interface debonding behavior is more of a local behavior that does not persist. Also, it is consistent with the estimations of the analytical criterion (Equation 4.12), as this simulation case is predicted to be a crossing case but close to the crossing/no crossing threshold. Figure 4.16b and Figure 4.17b further demonstrate the aperture distribution over the whole interface. Note that the interface for C2-80% is uncemented over the region of z = [-1.5 m, -2 m], the interface for C4-60% is cemented over the region of z = [-1 m, -2.5 m]. Signs of aperture changes are found near the boundaries of cemented/uncemented regions and the HF-NF intersection line, indicating that there is local fluid penetration at these locations. But most of the cemented regions still remain closed, consistent with the overall crossing behavior of the simulation.
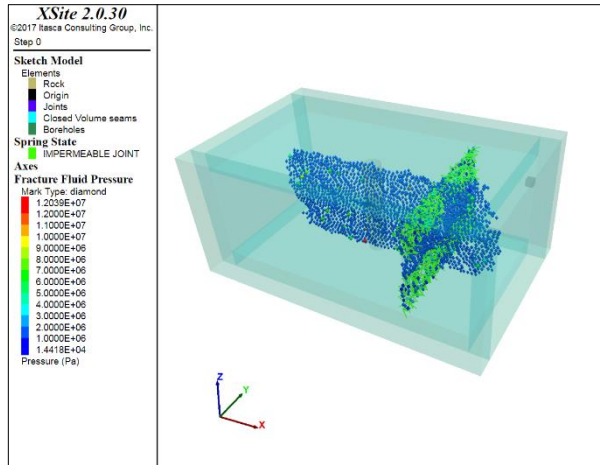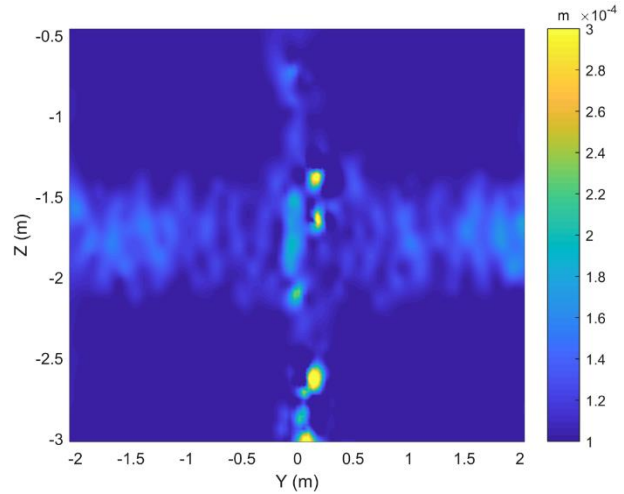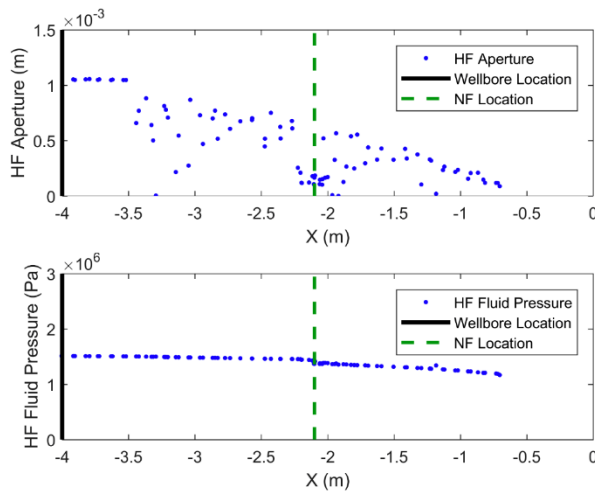
Figure 4.16: Crossing case for model with top-bottom region cemented interface: Test Set C2, 80% cemented. (a) Fluid pressure distribution; (b) crack aperture distribution along the NF, side view (y-z plane); (c) crack aperture and fluid pressure of the HF (along the vertical center of model, z = -1.75 m); (d) crack aperture and fluid pressure of the NF (along the vertical center of the top cemented region, z= -1.0 m).

Figure 4.17: Crossing case for model with central region cemented interface: Test Set C4, 60% cemented. (a) Fluid pressure distribution; (b) crack aperture distribution along the NF, side view (y-z plane); (c) crack aperture and fluid pressure of the HF (along the vertical center of model, z = -1.75 m); (d) crack aperture and fluid pressure of the NF (along the vertical center of NF, z = -1.75 m).

Typical no-crossing results for top-bottom region cemented case (Test Set C2, 48% cemented) and central region cemented case (Test Set D3, 60% cemented) are shown respectively in Figure 4.18 and Figure 4.19. We observe that the HFs in both cases are arrested by the NF (in Figure 4.18a and Figure 4.19a). This is evidenced by the aperture profile and fluid pressure distribution in Figure 4.18c and Figure 4.19c, in which the crack tip stopped close to the location of the NF ($x = 1.9$ m). Similar to the limited debonding captured in the previous crossing case, short crossing (~0.1 m for C2-48% and ~0.3 m for D3-60%) is found in these two no-crossing cases. However, this short-crossing behavior is local and non-persistent, and is eventually suppressed by large regions of interface debonding behavior. Figure 4.18d and Figure 4.19d illustrate the increased aperture width and fluid pressure distribution over a wide range of the cemented region, implying that cementation within this range fails and hydraulic fluid enters the NF. The dominating behavior of interface debonding can be better viewed in Figure 4.18b and Figure 4.19b, in which significant signs of aperture width change are widely found in the originally cemented regions.

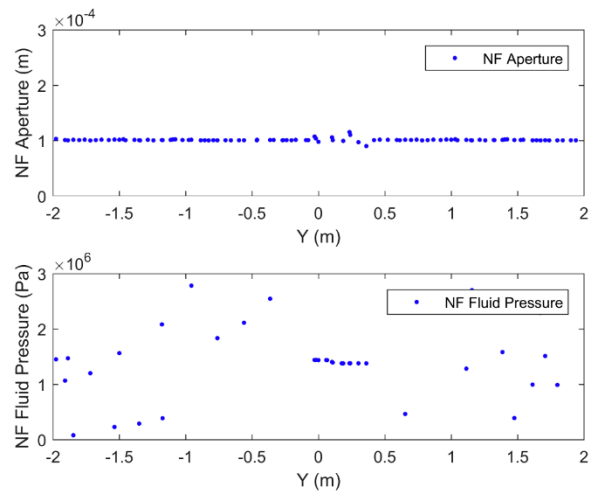(a)   (b)
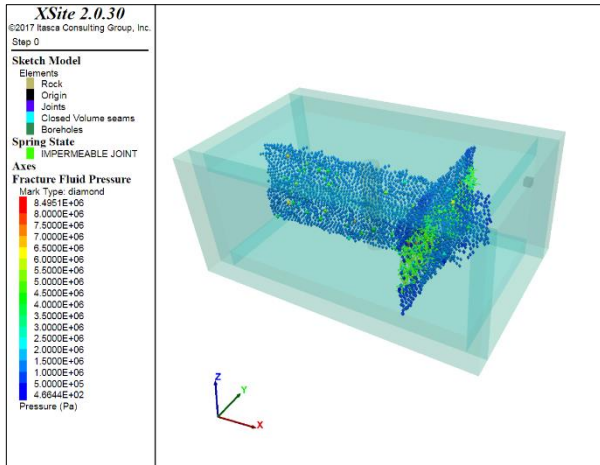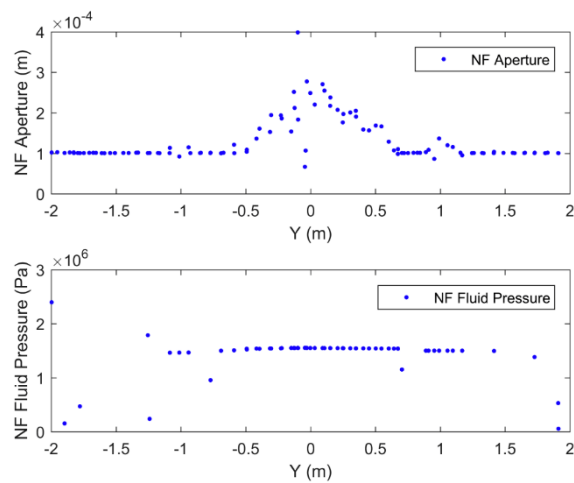

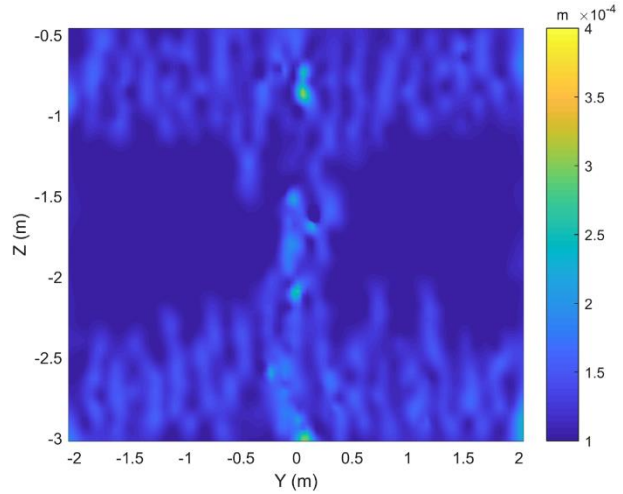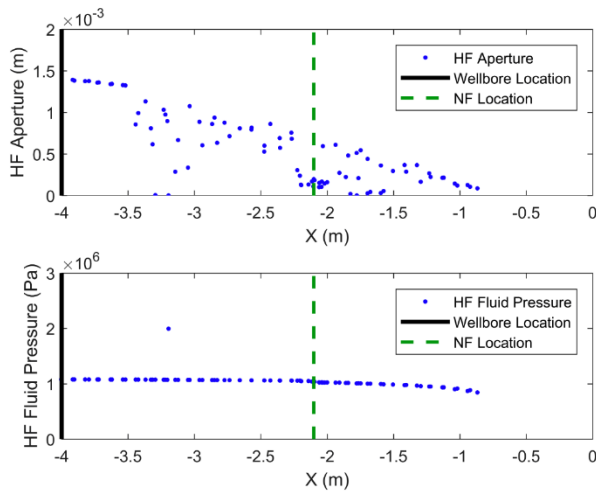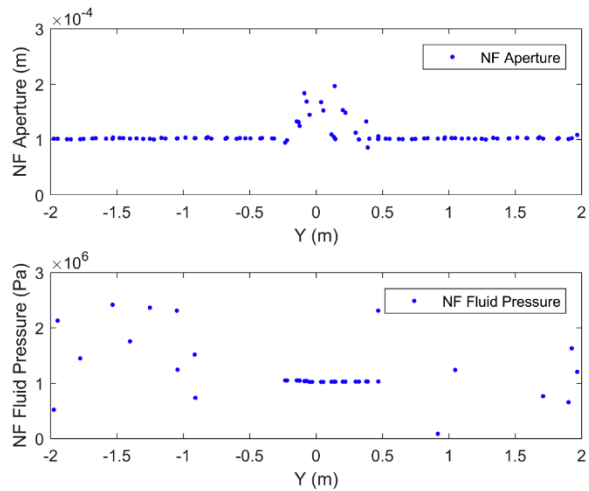(c)   (d)

Figure 4.18: No-crossing case for model with top-bottom region cemented interface: Test Set C2, 48% cemented. (a) Fluid pressure distribution; (b) crack aperture distribution along the NF, side view (y-z plane); (c) crack aperture and fluid pressure of the HF (along the vertical center of model, z = -1.75 m); (d) crack aperture and fluid pressure of the NF (along the vertical center of top cemented region, z = -0.8 m).
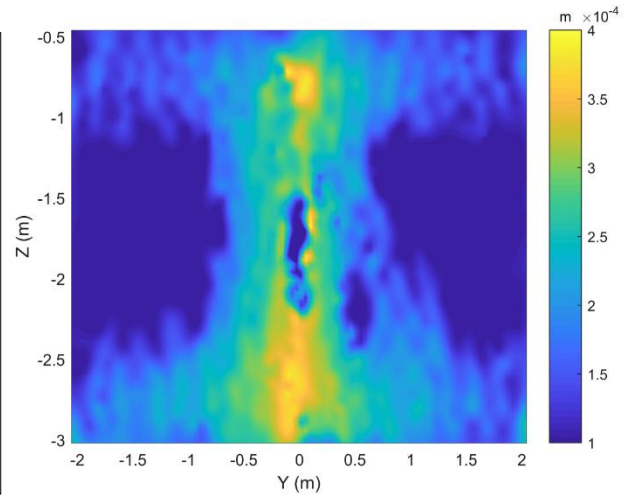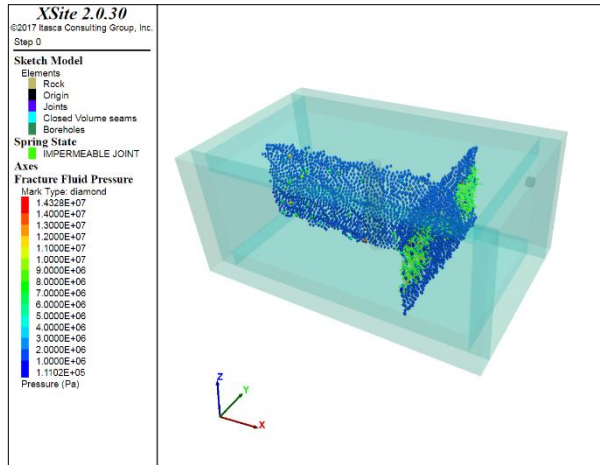
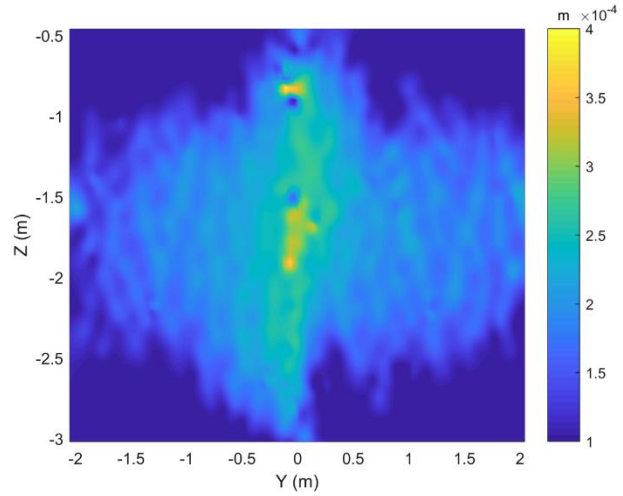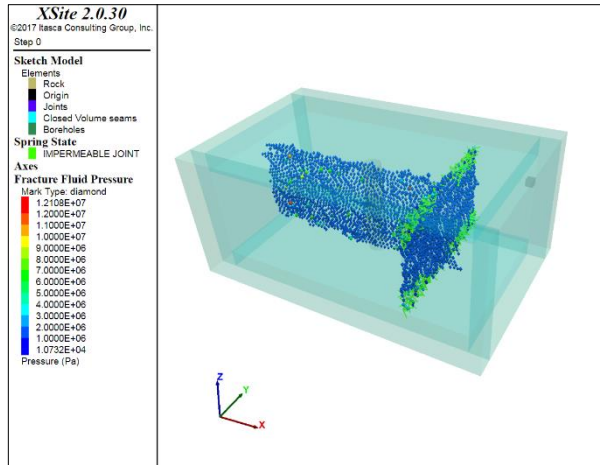<div align="center">(a)</div>

<div align="center">(b)</div>
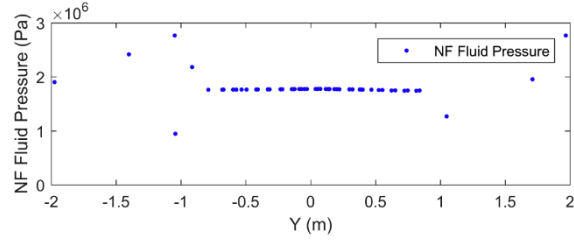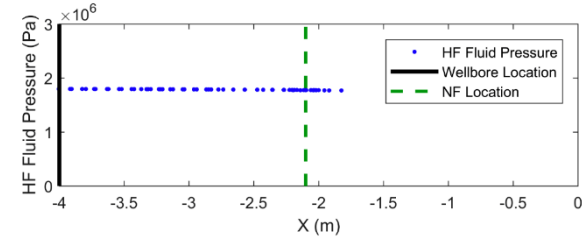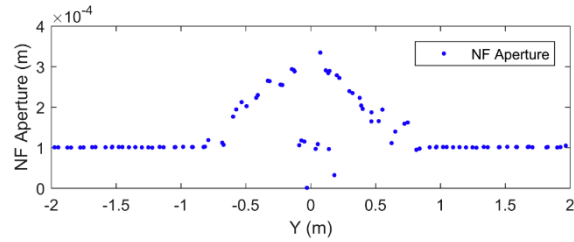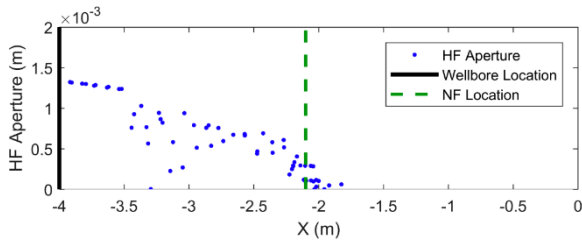
<div align="center">(c)</div>
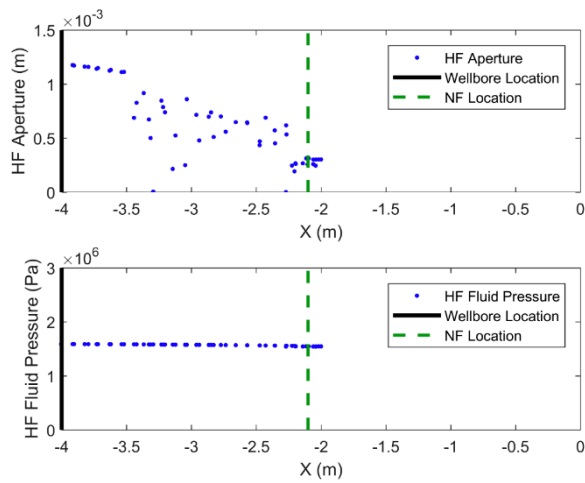

<div align="center">(d)</div>

Figure 4.19: No-crossing case for model with central region cemented interface: Test Set D3, 60% cemented. (a) Fluid pressure distribution; (b) crack aperture distribution along the NF, side view (y-z plane); (c) crack aperture and fluid pressure of the HF (along the vertical center of model, z = -1.75 m); (d) crack aperture and fluid pressure of the NF (along the vertical center of NF, z = -1.75 m).

Now we compare the simulation results of partially cemented cases with the analytical criterion developed by Fu et al. (Fu et al. 2018a). Similar to the comparison of fully cemented cases, only one threshold needs to be satisfied for the HF to cross the NF, as the other threshold is matched in advance by setting proper NF strength parameters. Figure 4.20 presents a comparison between simulation results from Table 4.4 and the Interface Slipping Threshold. Overall, good agreement is observed for NF friction coefficient ranging from 0.4 to 1.46, regardless of NF friction coefficient/cohesion, location of cemented regions, cemented proportions or the host rock material. Indeed, only two cases in Test Set C3 and one case in Test Set C5, all close to the threshold, show different simulation results than predicted by the analytical criterion. The simulation results of cases in Table 4.5 are also found to match the Interface Opening Threshold well, as shown in Figure 4.21. As predicted by the Interface Opening Threshold, a clear transition from no crossing to crossing is observed in all three test sets when the cemented proportions of the NF increase.
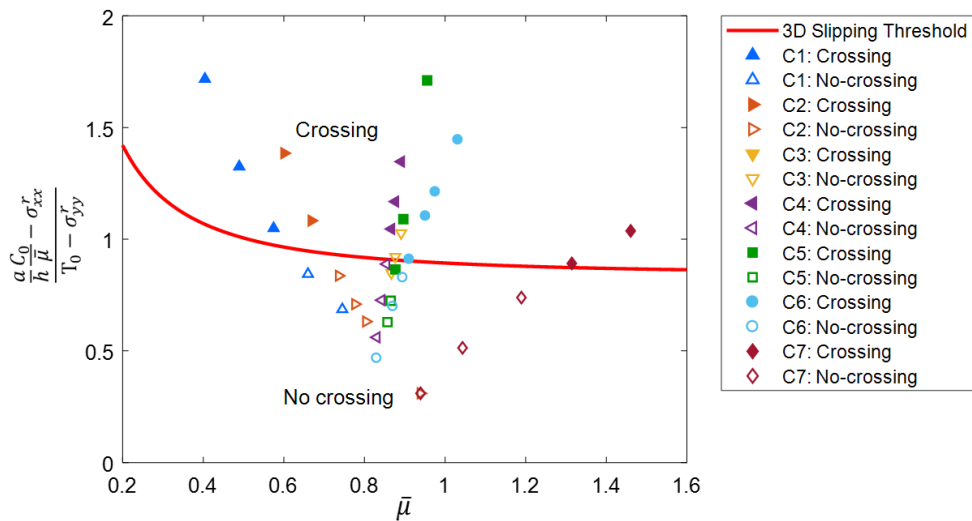
Figure 4.20: Comparison between simulation results of partially cemented cases and Interface Slipping Threshold.
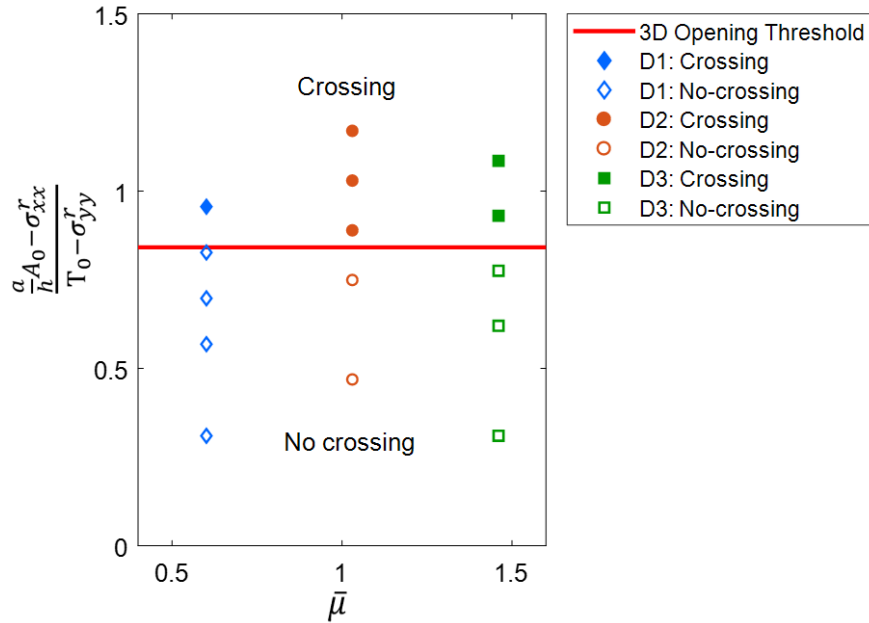
Figure 4.21: Comparison between simulation results of partially cemented cases and Interface Opening Threshold.

4.7 DISCUSSION

The numerical simulations of fully and partially cemented cases generally correspond to the following field conditions, depending on the properties of the pre-existing interface:

- Condition 1: Simulations with fully cemented interface (Test Sets A1-A7, B1-B3). These are an analogue of the field condition in which a HF encounters a large NF that spans throughout the reservoir height/HF height with uniform properties (Figure 4.22a).

- Condition 2: Simulations with partially-cemented interface (Test Sets C1-C7, D1-D3). These are an analogue of the field condition when a HF encounters larger NFs that

persist over the height of the reservoir/HF height and are partially sealed with mineral cementation (Figure 4.22b and Figure 4.22c).

- Condition 3: Simulations with interface that is partially cemented by strong bond which has same mechanical properties as the host rock (Test Sets C5-C7). These are an analogue of the field condition when a HF encounters short, uncemented NFs (Figure 4.22b and Figure 4.22c). For simulations that belong to this condition, the strongly cemented regions are treated as intact rock while the uncemented regions serve as weak NFs.
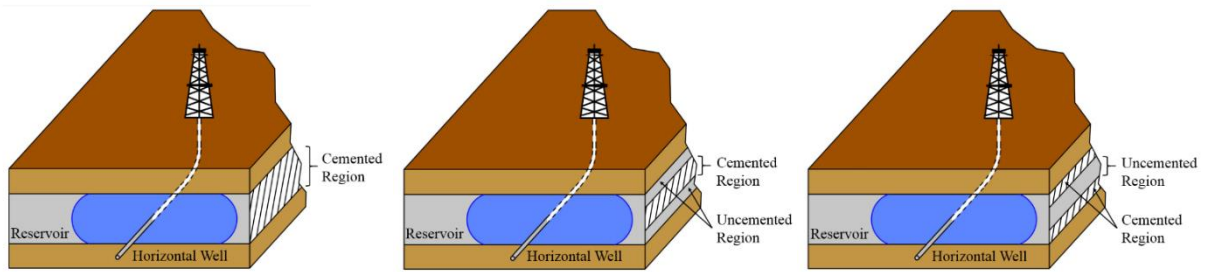
Figure 4.22: Field examples for a) fully cemented case; b) central region cemented case; c) top-bottom region cemented case. Modified from (Fu et al. 2018a).

Condition 1 has been widely assumed in most studies. For this condition, we observe a strong impact of NF shear strength on the HF propagation in the numerical simulation. Also, the crossing/no crossing behaviors demonstrate noticeably less dependence on the friction coefficient as it increases, compared to the prediction of the extended *R-P criterion*. This observation matches the analytical prediction of the Interface Slipping Threshold, and is consistent with recent experimental and/or analytical studies presented by Bunger et al. (Bunger et al. 2015) and Llanos et al. (Llanos et al. 2017), in which the crossing of HF through discontinuities appear to be

116

relatively independent of the friction coefficient. In addition to the NF shear strength, the NF tensile strength is found to exert significant impacts on the HF-NF interaction as well, as predicted by the Interface Opening Threshold, which did not receive full attention in some prior work.

The simulation cases with partially cemented interface correspond to the Conditions 2 and 3. Besides the good agreement observed between the numerical simulation and analytical criterion, one key observation is that the proportion of the NF cemented regions can strongly influence the HF propagation. Strikingly, under simulation conditions, the HF is shown to cross the NF even if over 60% - 80% percent of the interface is uncemented (cases in Test Sets C5 and C6). This is consistent with lab observations in which a HF crossed an interface and attained full layer height again after crossing when somewhere between 70% and 90% of the interface is completely unbonded (Fu et al. 2015). Furthermore, in cases when cemented regions of NF can be treated as intact rock (C5, C6 and C7), the HF is found to be able to engulf uncemented NFs with varying height (80%, 60% and 28% respectively) and continue growing after crossing as observed in lab experiments (Fu et al. 2016, 2018a), in contrast to the behavior of HF bypassing hard inclusions (Olson et al. 2012). On the other hand, we observe in the simulation that the HF still debonds and deviates into the NF when as much as 80% of the interface is cemented (in Test D1). In other words, the HF cannot cross the NF in this case unless the entire interface is mostly bonded. These significant and almost certainly realistic effects for field applications demonstrate that it is crucial to account for the cemented portions and geometrical size of the NF when estimating the HF propagation patterns.

Further insight can be gained by examining the detailed behavior of the HF when impinging on a partially cemented NF. We observe that there may be limited signs of interface debonding in a crossing case, or short fluid penetration across the NF in a no-crossing case (e.g.

Figure 4.17 and Figure 4.19). These cases ideally illustrate that the 3D interaction behavior between HFs and NFs is fundamentally a result of the competition between the localized HF-NF interaction mechanism and the dominating outcome of global interaction influenced by the overall properties of the NF. For instance, the case in Figure 4.19 is 60% cemented, and a short crossing in the cemented region is observed, as predicted by the analytical criterion when evaluating the behavior locally (in 2D). However, as the rest of the uncemented regions fail, the local and limited fluid penetration is suppressed and replaced by large regions of interface slipping or opening, which eventually lead to a dominating global behavior of no-crossing. In contrast, previous 2D and pseudo-3D models will only favor localized behaviors instead of fully coupled interaction, and therefore miss the vital global views of HF-NF interaction.

It is to be noted that we primarily focus on the effects of NF heterogeneities (cemented proportion, NF height, joint tensile strength, cohesion, friction coefficient) on HF propagation in this study. Hence, other parameters are treated as controlled variables and kept constant. As we discussed before, the fluid flow parameters, such as the injection rate and fluid viscosity, may also influence the HF patterns. Also, HFs can encounter NFs at various intersection angles in the field. An extension of study to include those factors is certainly possible, and will comprise a topic for the future research.

4.8   CONCLUSIONS

NFs with varying cementation portions, non-uniform cementation strength and/or different height are widely observed in reservoirs, which are incompatible with the typical assumption of most studies that NFs persist through the full height of the reservoir/HF with uniform properties. In this

study, we employed a fully-coupled lattice simulator (XSite) to simulate the seldom considered but realistically important 3D interactions between HFs and NFs. Consistent with the experimental observations, the numerical simulation captures the strong dependence of HF propagation patterns on NF cemented proportions and height. As the cemented proportion of the NF decreases or the height of the uncemented NF increases, the HF-NF interaction behaviors evolve from crossing to no-crossing. The simulation also demonstrates that for strong bond, a small critical cemented height in an otherwise weak NF is sufficient to promote HF crossing; while in cases when the cement is relatively weak, a HF will get arrested and deviate into the NF unless the NF is nearly fully cemented.

The fully-coupled numerical simulations also reveal that the 3D interaction between HFs and NFs is an outcome of global interaction which is influenced by the overall properties of encountered NFs, not just the localized HF-NF interaction determined by local interface conditions alone. For instance, the initial crossing behavior at a strongly cemented region may end up with very limited fluid penetration, and eventually be suppressed and replaced by large regions of interface slipping/opening. This global interaction mechanism is not typically mentioned in past HF-NF interaction studies, but shown here to be crucial for accurate prediction of interaction behaviors.

Finally, in an extended parametric study of the impact of NF properties, the simulation results are observed to match an experimentally verified 3D analytical criterion well for twenty sets of simulation cases, with different NF cohesion, friction coefficient, tensile strength, location of cemented regions, cemented proportions, and/or host rock materials. As the frictional coefficient increases, the simulation demonstrates notably less dependence of crossing/no crossing behaviors on the frictional properties, as predicted by the analytical criterion and observed in experiments.

The heterogeneities of NFs are shown to play essential roles in controlling the crossing/no crossing behaviors for a wide range of NF properties. Hence, these results provide impetus for better characterization of NFs that includes NF cementation proportion, height and variation of the strength properties, and consideration of NF heterogeneities to achieve more realistic estimation of HF network complexity in reservoirs.

5.0   CONCLUSIONS

Hydraulic fracturing is the main technology for permeability enhancement in unconventional oil/gas or geothermal reservoirs. The wide existence of NFs in reservoirs is one of the key factors that can greatly influence the HF propagation. This dissertation research was carried out to study the impact of NF heterogeneities on the propagation trajectory of the HF. The main contributions of the research begin with the demonstration of strong dependence of HF-NF interaction behaviors on spatially-varied NF properties. When the NFs are partially cemented, interaction with NFs results in three observed behaviors depending upon the proportion of the NF that is cemented. As the relative height of the cemented region is decreased from one laboratory experiment to the next, the interaction behaviors change from (1) complete crossing, to (2) crossing at cemented region(s) with mismatched crack path at uncemented region(s), to (3) no crossing. When the NFs are fully cemented, the interaction behaviors change from no-crossing to crossing as the NF bonding strength increases. In some cases with strong interface cementation, a relatively small cemented region in an otherwise weak NF is sufficient to promote HF crossing; In contrast, when the cement is relatively weak, a HF may get arrested and deviate into the NF even if the NF is mostly cemented. Hence, ignoring the fact that the NFs can be partially-cemented and/or non-persistent may lead to misleading predictions of the HF propagation in fractured reservoirs.

The second main contribution is development of a new analytical criterion based on linear elastic fracture mechanics to quantitatively assess the influence of NF heterogeneity on the HF's

121

crossing/no crossing behaviors. The criterion evaluates the stress components acting along the interface to promote interface crossing/debonding at the locations where they are maximized, and determines the threshold for the fracture initiation when both the opening and the slipping of the NFs are suppressed. This is the first analytical criterion that accounts for the spatial variations of NF properties. Consistent with laboratory results, this criterion captures the dependence of interaction behaviors on the proportion of cemented region(s), cementation strength, and the NF height relative to the total reservoir/HF height. It is compared with experimental results from four sets of hydraulic fracturing tests and observed to provide good predictions for the 3D HF-NF interaction behaviors.

Thirdly, the research provides fully-coupled DEM lattice simulations on the 3D interaction between HFs and partially cemented NFs. The numerical simulation captures the key interaction behaviors in lab experiments, and matches the developed analytical criterion well in a large parametric space of NF properties, which includes twenty series of simulation cases with different NF cohesion, tensile strength, friction coefficient, location of cemented regions, cemented proportions, and/or host rock materials.

Finally, the research reveals, through fully-coupled simulations, that the 3D interaction between HFs and NFs is fundamentally an outcome of global interaction mechanism influenced by the overall properties of encountered NFs, not just a localized HF-NF interaction determined by local interface conditions alone. For instance, the initial crossing behavior at a partially cemented NF may end up with very limited fluid penetration, and eventually be suppressed and replaced by large regions of interface slipping/opening as the uncemented region(s) fails. This observation is important as it illustrates that it is essential to have a global view in the prediction of HF propagation, instead of localized behaviors favored in some 2D and pseudo-3D models.

In summary, from experimental, analytical and numerical approaches, this research shows both qualitatively and quantitatively the impact of NF heterogeneities on the HF propagation. It identifies the role of spatially-varied NF properties in HF-NF interaction, provides an explicit analytical criterion for predicting the 3D interaction behaviors, and brings impetus for better characterization of NFs and consideration of NF heterogeneities to achieve more realistic estimation of potentially complex and multi-stranded HF propagation in unconventional reservoirs.

BIBLIOGRAPHY

ASTM:C39/C39M-15a (2012) Standard test method for compressive strength of cylindrical concrete specimens. ASTM Int 1–7. doi: 10.1520/C0039

ASTM International (2010) Standard test method for tensile strength of concrete surfaces and the bond strength or tensile strength of concrete repair and overlay materials by direct tension (pull-off method). ASTM Stand 1–4. doi: 10.1520/C1583

Bahaaddini M, Hagan P, Mitra R, Hebblewhite BK (2009) Numerical study of the mechanical behavior of nonpersistent jointed rock masses. Int Journals geochanics 16:1–10. doi: 10.1061/(ASCE)GM.1943-5622.0000510.

Bahorich B, Olson JE, Holder J (2012) Examining the effect of cemented natural fractures on hydraulic fracture propagation in hydrostone block experiments. In: SPE Annual Technical Conference and Exhibition. SPE Annual Technical Conference and Exhibition, 8-10 October, San Antonio, Texas

Bažant Z, Planas J (1997) Fracture and size effect in concrete and other quasi brittle material. CRC Press, London

Beugelsdijk LJL, de Pater CJ, Sato K (2000) Experimental hydraulic fracture propagation in a multi-fractured medium. SPE Asia Pacific Conference on Integrated Modelling for Asset Management, 25-26 April, Yokohama, Japan

Blanton TL (1986) Propagation of hydraulically and dynamically induced fractures in naturally fractured reservoirs. SPE Unconventional Gas Technology Symposium, 18-21 May, Louisville, Kentucky

Blanton TL (1982) An experimental study of interaction between hydraulically induced and pre-existing fractures. SPE Unconventional Gas Recovery Symposium, 16-18 May, Pittsburgh, Pennsylvania

Budyn E, Zi G, Moes N, Belytschko T (2004) A model for multiple crack growth in brittle materials without remeshing. Int J Numer Methods Eng 61:1741–1770

Bunger AP, Jeffrey RG, Detournay E (2004) Toughness-dominated near-surface hydraulic fracture experiments. Gulf Rocks 2004, the 6th North America Rock Mechanics Symposium (NARMS), 5-9 June, Houston, Texas

Bunger AP, Kear J, Jeffrey RG, et al (2015) Laboratory investigation of hydraulic fracture growth through weak discontinuities with active ultrasound monitoring. 13th ISRM International Congress of Rock Mechanics, 10-13 May, Montreal, Canada

Chuprakov DA, Akulich A, Siebrits E, Thiercelin M (2011) Hydraulic-fracture propagation in a naturally fractured reservoir. SPE Prod Oper 26:88–97. doi: 10.2118/128715-pa

Chuprakov DA, Melchaeva O, Prioul R (2013) Injection-sensitive mechanics of hydraulic fracture interaction with discontinuities. 47th U.S. Rock Mechanics/Geomechanics Symposium, 23-26 June, San Francisco, California

Corporation S (2016) Product data sheet: Sikadur 32, Hi-Mod, 10th ed. Sika Corporation

Crouch SL, Starfield AM (1983) Boundary element methods in solid mechanics, 1st ed. George Allen & Unwin, London

Cundall PA (2011) Lattice method for modeling brittle, jointed rock. 2nd Int'l FLAC/DEM Symposium on Continuum and Distinct Element Numerical Modeling in Geomechanics, 14-16 February, Melbourne, Australia

Dahi-Taleghani A, Olson JE (2011) Numerical modeling of multistranded-hydraulic-fracture propagation: accounting for the interaction between induced and natural fractures. SPE J 16:575–581. doi: 10.2118/124884-PA

Dahi Taleghani A, Olson JE (2013) How natural fractures could affect hydraulic-fracture geometry. SPE J 19:161–171. doi: 10.2118/167608-PA

Damjanac B, Cundall PA (2016) Application of distinct element methods to simulation of hydraulic fracturing in naturally fractured reservoirs. Comput Geotech 71:283–294. doi: 10.1016/j.compgeo.2015.06.007

Damjanac B, Detournay C (2013) Three-dimensional numerical model of hydraulic fracturing in fractured rock masses. Eff Sustain Hydraul Fract 819–830. doi: 10.5772/56313

Damjanac B, Detournay C, Cundall PA (2016) Application of particle and lattice codes to simulation of hydraulic fracturing. Comput Part Mech 3:249–261. doi: 10.1007/s40571-015-0085-0

Damjanac B, Gil I, Pierce M, Sanchez M (2010) A new approach to hydraulic fracturing modeling in naturally fractured reservoirs. 44th U.S. Rock Mechanics Symposium and 5th U.S.-Canada Rock Mechanics Symposium, 27-30 June, Salt Lake City, Utah

Detournay E (2004) Propagation regimes of fluid-driven fractures in impermeable rocks. Int J Geomech 4:35–45. doi: 10.1061/(ASCE)1532-3641(2004)4:1(35)

Dieterich JH (1972) Time-dependent friction in rocks. J Geophys Res 77:110–122. doi: 10.1029/JB077i020p03690

Doe TW, Boyce G (1989) Orientation of hydraulic fractures in salt under hydrostatic and non-hydrostatic stresses. Int J Rock Mech Min Sci Geomech Abstr 26:605–611. doi: 10.1016/0148-9062(89)91441-1

Economides M, Nolte K (2000) Reservoir stimulation, 3rd ed. Wiley Chichester, New York

Einstein HH, Veneziano D, Baecher GB, O'Reilly KJ (1983) The effects of discontinuity persistence on rock slope stability. Int J Rock Mech Miner Sci Geomech 20:227–236

Fidler LJ (2011) Natural fracture characterization of the New Albany Shale, Illinois Basin, United States. The University of Texas at Austin

Fisher MK, Heinze JR, Harris CD, et al (2004) Optimizing horizontal completion techniques in the barnett shale using microseismic fracture mapping. SPE Annual Technical Conference and Exhibition, 26-29 September, Houston, Texas

Fisher MK, Wright CA, Davidson BM, et al (2005) Integrating fracture mapping technologies to improve stimulations in the barnett shale. SPE Prod Facil 20:85–93. doi: 10.2118/77441-PA

Fu P, Johnson SM, Carrigan C (2012) An explicitly coupled hydro-geomechanical model for simulating hydraulic fracturing in complex discrete fracture networks. Int J Numer Anal Methods Geomech 37:2278–2300. doi: 10.1002/nag.2135

Fu W, Ames BC, Bunger AP, Savitski AA (2015) An experimental study on interaction between hydraulic fractures and partially-cemented natural fractures. 49th U.S. Rock Mechanics/Geomechanics Symposium, 28 June-1 July, San Francisco, California

Fu W, Ames BC, Bunger AP, Savitski AA (2016) Impact of partially cemented and non-persistent natural fractures on hydraulic fracture propagation. Rock Mech Rock Eng 49:4519–4526. doi: 10.1007/s00603-016-1103-0

Fu W, Savitski AA, Bunger AP (2018a) Analytical criterion predicting the impact of natural fracture strength, height and cemented portion on hydraulic fracture growth. Eng Fract Mech In Review

Fu W, Savitski AA, Damjanac B, Bunger AP (2018b) Three-dimensional lattice simulation of hydraulic fracture interaction with natural fractures. Comput Geotech Submitted

Gale JFW, Holder J (2008) Natural fractures in the Barnett Shale: constraints on spatial organization and tensile strength with implications for hydraulic fracture treatment in shale-gas reservoirs. The 42nd U.S. Rock Mechanics Symposium (USRMS), 29 June-2 July, San Francisco, California

Gale JFW, Laubach SE, Olson JE, et al (2014) Natural fractures in shale: a review and new observations. Am Assoc Pet Geol Bull 98:2165–2216. doi: 10.1306/08121413151

Gale JFW, Reed RM, Holder J (2007) Natural fractures in the Barnett Shale and their importance for hydraulic fracture treatments. Am Assoc Pet Geol Bull 91:603–622. doi: 10.1306/11010606061

Gao H, Rice JR (1987) Somewhat circular tensile cracks. Int J Fract 33:155–174. doi: 10.1007/BF00013168

Garagash DI, Detournay E (2000) The Tip Region of a Fluid-Driven Fracture in an Elastic Medium. J Appl Mech 67:183–192. doi: 10.1115/1.321162

Gu H, Weng X (2010) Criterion for fractures crossing frictional interfaces at non-orthogonal angles. 44th U.S. Rock Mechanics Symposium and 5th U.S.-Canada Rock Mechanics Symposium, 27-30 June, Salt Lake City, Utah

Gu H, Weng X, Lund J, et al (2012) Hydraulic fracture crossing natural fracture at nonorthogonal angles: a criterion and its validation. SPE Prod Oper 27:20–26. doi: 10.2118/139984-PA

Hanson ME, Shaffer RJ, Anderson GD (1981) Effects of various parameters on hydraulic fracturing geometry. Soc Pet Eng J 21:435–443. doi: 10.2118/8942-PA

Heck WJ, Lane KS (1964) Triaxial testing for strength of rock joints. The 6th U.S Symposium on Rock Mechanics (USRMS), 28-30 October, Rolla, Missouri

Hennings PH, Olson JE, Thompson LB (2000) Combining outcrop data and three-dimensional structural models to characterize fractured reservoirs: An example from Wyoming. Am Assoc Pet Geol Bull 84:830–849. doi: 10.1306/A967340A-1738-11D7-8645000102C1865D

Hoskins ER, Jaeger JC, Rosengren KJ (1968) A medium-scale direct friction experiment. Int J Rock Mech Min Sci Geomech Abstr 5:143–152

Irwin GR (1957) Analysis of stresses and strains near the end of a crack traversing a plate. J Appl Mech 24:361–364

Irwin GR (1960) Plastic zone near a crack and fracture toughness. 7th Sagamore Conference, 16-19 August, Racquette Lake, New York

Itasca Consulting Group I (2008a) PFC2D (Particle Flow Code in 2 Dimensions)

Itasca Consulting Group I (2008b) PFC3D (Particle Flow Code in 3 Dimensions)

Jeffrey RG, Bunger AP, Lecampion B, et al (2009a) Measuring hydraulic fracture growth in naturally fractured rock. SPE Annual Technical Conference and Exhibition, 4-7 October, New Orleans, Louisiana

Jeffrey RG, Kear J, Kasperczyk D, et al (2015) A 2D experimental method with results for hydraulic fractures crossing discontinuities. 49th U.S. Rock Mechanics/Geomechanics Symposium, 28 June-1 July, San Francisco, California

Jeffrey RG, Zhang X, Thiercelin M (2009b) Hydraulic fracture offsetting in naturally fractured reservoirs: quantifying a long-recognized process. SPE Hydraulic Fracturing Technology Conference, 19-21 January, The Woodlands, Texas

Kim BH, Kaiser PK, Grasselli G (2007) Influence of persistence on behaviour of fractured rock masses. Geol Soc London, Spec Publ 284:161–173. doi: 10.1144/SP284.11

Kovari K, Tisa A, Einstein HH, Franklin JA (1983) Suggested methods for determining the strength of rock materials in triaxial compression: revised version. Int J rock Mech Min Sci 20:283–290

Kresse O, Weng X, Chuprakov D, et al (2013a) Effect of flow rate and viscosity on complex fracture development in UFM model. Eff. Sustain. Hydraul. Fract. 183–210

Kresse O, Weng X, Gu H, Wu R (2013b) Numerical modeling of hydraulic fractures interaction in complex naturally fractured formations. Rock Mech Rock Eng 46:555–568. doi: 10.1007/s00603-012-0359-2

Labuz JF, Shah SP, Dowding CH (1987) The fracture process zone in granite: evidence and effect. Int J Rock Mech Min Sci Geomech Abstr 24:235–246. doi: 10.1016/0148-9062(87)90178-1

Lander RH, Laubach SE (2014) Insights into rates of fracture growth and sealing from a model for quartz cementation in fractured sandstones. Bull Geol Soc Am 127:516–538. doi: 10.1130/B31092.1

Laubach SE (2003) Practical approaches to identifying sealed and open fractures. Am Assoc Pet Geol Bull 87:561–579. doi: 10.1306/11060201106

Laubach SE, Fall A, Copley LK, et al (2016) Fracture porosity creation and persistence in a basement-involved Laramide fold, Upper Cretaceous Frontier Formation, Green River Basin, USA. Geol Mag 153:887–910. doi: 10.1017/S0016756816000157

Lecampion B, Detournay E (2007) An implicit algorithm for the propagation of a hydraulic fracture with a fluid lag. Comput Methods Appl Mech Eng 196:4863–4880. doi: 10.1016/j.cma.2007.06.011

Lee HP, Olson JE, Holder J, et al (2014) The interaction of propagating opening mode fractures with preexisting discontinuities in shale. J Geophys Res Solid Earth 120:169–181. doi: 10.1002/2014JB011358

Lisjak A, Kaifosh P, He L, et al (2017) A 2D, fully-coupled, hydro-mechanical, FDEM formulation for modelling fracturing processes in discontinuous, porous rock masses. Comput Geotech 81:1–18. doi: 10.1016/j.compgeo.2016.07.009

Llanos EM, Jeffrey RG, Hillis R, Zhang X (2017) Hydraulic fracture propagation through an orthogonal discontinuity: a laboratory, analytical and numerical study. Rock Mech Rock Eng 50:2101–2118. doi: 10.1007/s00603-017-1213-3

Maxwell SC, Urbancic TI, Steinsberger N, et al (2002) Microseismic imaging of hydraulic fracture complexity in the Barnett Shale. SPE Annual Technical Conference and Exhibition, 29 September-2 October, San Antonio, Texas

McClure MW, Babazadeh M, Shiozawa S, Huang J (2016) Fully coupled hydromechanical simulation of hydraulic fracturing in 3D discrete-fracture networks. SPE J 21:1302–1320. doi: 10.2118/173354-MS

Nagel NB, Gil I, Sanchez-nagel M, Damjanac B (2011) Simulating hydraulic fracturing in real fractured rocks-overcoming the limits of Pseudo3D models. SPE Hydraulic Fracturing Technology Conference, 24-26 January, The Woodlands, Texas

Nagel NB, Sanchez-Nagel MA, Zhang F, et al (2013) Coupled numerical evaluations of the geomechanical interactions between a hydraulic fracture stimulation and a natural fracture system in shale formations. Rock Mech Rock Eng 46:581–609 . doi: 10.1007/s00603-013-0391-x

Olson JE, Dahi Taleghani A (2009) Modeling simultaneous growth of multiple hydraulic fractures and their interaction with natural fractures. SPE Hydraulic Fracturing Technology Conference, 19-21 January, The Woodlands, Texas

Olson JE, Bahorich B, Holder J (2012) Examining hydraulic fracture-natural fracture interaction in hydrostone block experiments. SPE Hydraulic Fracturing Technology Conference, 6-8 February, The Woodlands, Texas

Philipp SL (2008) Geometry and formation of gypsum veins in mudstones at Watchet, Somerset, SW England. Geol Mag 145:831–844. doi: 10.1017/S0016756808005451

Pierce M, Cundall P, Potyondy D, Mas Ivars D (2007) A synthetic rock mass model for jointed rock. Conference: Rock Mechanics: Meeting Society's Challenges and Demands (1st Canada-U.S. Rock Mechanics Symposium),27–31 May,Vancouver, Canada

Potyondy DO, Cundall PA (2004) A bonded-particle model for rock. Int J Rock Mech Min Sci 41:1329–1364. doi: 10.1016/j.ijrmms.2004.09.011

Renshaw CE, Pollard DD (1995) An experimentally verified criterion for propagation across unbounded frictional interfaces in brittle, linear elastic materials. Int J Rock Mech Min Sci 32:237–249. doi: 10.1016/0148-9062(94)00037-4

Savitski AA, Detournay E (2002) Propagation of a penny-shaped fluid-driven fracture in an impermeable rock: asymptotic solutions. Int J Solids Struct 39:6311–6337. doi: 10.1016/S0020-7683(02)00492-4

Settgast RR, Fu P, Walsh SDC, et al (2017) A fully coupled method for massively parallel simulation of hydraulically driven fractures in 3-dimensions. Int J Numer Anal Methods Geomech 41:627–653. doi: 10.1002/nag.2557

Shang J, Hencher SR, West LJ, Handley K (2017) Forensic excavation of rock masses: a technique to investigate discontinuity persistence. Rock Mech Rock Eng 50:2911–2928. doi: 10.1007/s00603-017-1290-3

Tada H, Paris PC, Irwin GR (2000) The stress analysis of cracks, 3 rd ed. ASME Press, New York

Teufel L, Clark J (1984) Hydraulic fracture propagation in layered rock: experimental studies of fracture containment. Soc Pet Eng J 24:19–32. doi: 10.2118/9878-PA

Twiss RJ, Moores EM (1992) Structural geology, 1st ed. W. H. Freeman, New York

Wang Y, Li CH (2017) Investigation of the effect of cemented fractures on fracturing network propagation in model block with discrete orthogonal fractures. Rock Mech Rock Eng 50:1851–1862. doi: 10.1007/s00603-017-1198-y

Warpinski N, Kramm RC, Heinze JR, Waltman CK (2005) Comparison of single-and dual-array microseismic mapping techniques in the Barnett shale. 2005 SEG Annual Meeting, 6-11 November, Houston, Texas

Warpinski NRR, Teufel LLW (1987) Influence of geologic discontinuities on hydraulic fracture propagation. J Pet Technol 39:209–220. doi: 10.2118/13224-PA

Weng X, Kresse O, Chuprakov D, et al (2014) Applying complex fracture model and integrated workflow in unconventional reservoirs. J Pet Sci Eng 124:468–483. doi: 10.1016/j.petrol.2014.09.021

Weng X, Kresse O, Cohen C-E, et al (2011) Modeling of hydraulic-fracture-network propagation in a naturally fractured formation. SPE Prod Oper 26:368–380. doi: 10.2118/140253-PA

Wu K, Olson JE (2014) Mechanics analysis of interaction between hydraulic and natural fractures in shale reservoirs. Unconventional Resources Technology Conference, 25-27 August, Denver, Colorado

Wu K, Olson JE (2015) Numerical Investigation of Complex Hydraulic Fracture Development in Naturally Fractured Reservoirs. SPE Hydraulic Fracturing Technology Conference, 3-5 February, The Woodlands, Texas

Zhang F, Dontsov E, Mack M (2017) Fully coupled simulation of a hydraulic fracture interacting with natural fractures with a hybrid discrete-continuum method. Int J Numer Anal Methods Geomech 41:1430–1452. doi: 10.1002/nag.2682

Zhang X, Jeffrey RG (2006) The role of friction and secondary flaws on deflection and re-initiation of hydraulic fractures at orthogonal pre-existing fractures. Geophys J Int 166:1454–1465. doi: 10.1111/j.1365-246X.2006.03062.x

Zhang X, Jeffrey RG (2008) Reinitiation or termination of fluid-driven fractures at frictional bedding interfaces. J Geophys Res 113:B08416. doi: 10.1029/2007JB005327

Zhang X, Jeffrey RG, Thiercelin M (2009) Mechanics of fluid-driven fracture growth in naturally fractured reservoirs with simple network geometries. J Geophys Res Solid Earth 114:1–16. doi: 10.1029/2009JB006548

Zhang X, Jeffrey RG, Thiercelin M (2007) Deflection and propagation of fluid-driven fractures at frictional bedding interfaces: A numerical investigation. J Struct Geol 29:396–410. doi: 10.1016/j.jsg.2006.09.013

Zhou J, Chen M, Jin Y, Zhang G (2008) Analysis of fracture propagation behavior and fracture geometry using a tri-axial fracturing system in naturally fractured reservoirs. Int J Rock Mech Min Sci 45:1143–1152. doi: 10.1016/j.ijrmms.2008.01.001